SAPIENZA
UNIVERSITÀ DI ROMA

Dottorato di Ricerca in Fisica
Scuola di Dottorato "Vito Volterra"

Acoustic Detection of Ultra-High-Energy Cosmic Neutrinos

Thesis submitted to obtain the degree of
"Dottore di Ricerca" – Philosophiæ Doctor
PhD in Physics – XXI cycle – October 2008

by

Giulia De Bonis

Program Coordinator
Prof. Enzo Marinari

Thesis Advisors
Prof. Antonio Capone

to my Rose Of Shining Splendour,
Ever-Lastingly Loved Aunt,
remembering her eternal sunshine.

... like the moon, whose orb
Through optic glass the Tuscan artist views
At ev'ning from the top of Fesole,
Or in Valdarno, to descry new Lands,
Rivers or Mountains in her spotty Globe.

John Milton, *Paradise Lost*

...With so many light years to go
And things to be found...

Europe, *The Final Countdown*

Contents

Abstract

The main topic of this work is related to the opportunity of exploiting the thermo-acoustic effect of pressure pulse generation to detect high energy neutrinos in underwater environment, in the framework of neutrino astronomy, a promising field of investigation in the multi-messenger approach. Possible impacts of neutrino astronomy involve astrophysics (nature and behaviour of cosmic engines and explosive events in the Universe), particle physics (accelerator mechanisms, interaction cross section of particles above the threshold that can be explored in the laboratory, hints of new physics beyond the standard model) and cosmology (top-down models of ultra-high-energy particle generation, dark matter and cosmic neutrino background). Neutrino flux predictions compute a very low number of neutrino events at high energy, therefore a natural target is required when devising a cosmic neutrino detector. A straightforward choice is considering submarine apparatuses (or, alternatively, in-ice apparatuses), so that the oceanic mass can work, at the same time, as the target for neutrino interaction, the medium for signal transmission and the screen for atmospheric muon flux reduction. If charged leptons are produced in neutrino interactions, the Cherenkov radiation, emitted as a consequence of the passage of ultra-relativistic particles in water, can be detected through photo-multiplier tubes. A Cherenkov telescope is thus a regular arrangement of photo-multiplier tubes in the abyss. The acoustic technique aims to complement the Cherenkov technique in underwater neutrino telescopes, in order to extend the effective volume of detection up to several tens of kilometers cube. This because sound attenuation length is bigger than light attenuation length, allowing a coverage of a larger sensitive volume with a smaller number of sensors. The acoustic technique for particle detection is based on the thermo-acoustic mechanism, according to which interacting particle deposit their energy, inducing a perturbation of the thermodynamic equilibrium of the medium that propagates as a pressure wave, detectable by means of hydrophones. In order to develop a project for a neutrino acoustic telescope, detailed studies of the thermo-acoustic effect are required. The first stage is the validation of the technique, gained through test measurements with proton beams and supported by detailed analysis and simulation. The next step consists in moving to the neutrino case, taking advantage of the expertise achieved with protons. Monte Carlo simulations allow to predict properties and behaviour of neutrino-induced acoustic pulses. The work discussed in this thesis documents the efforts in the understanding of neutrino-induced acoustic signal; the outcome of the simulation can provide hints and clues to elaborate detection algorithms and reconstruction strategies, in order to evaluate the feasibility of the application of the acoustic technique in submarine neutrino telescopes.

Introduction

When talking to someone who is not a physicist, it is very difficult to explain that one can be an astronomer without putting eyes on telescopes. And things get even harder since astronomy, that is the branch of science that deals with stars and distant objects above us, can be investigated detecting sub-atomic particles underwater.

The traditional picture of the astronomer is Galileo Galilei (Figure 1), who did astronomy looking through his own telescope, a self-made optical instrument containing an arrangement of lenses and mirrors, to focus and magnify distant objects far away in the sky. And far away in the sky meant the Moon, or Jupiter with its satellites, or maybe a quick look outside the Solar System, to some luminous tracks in the Milky Way.

Since then, a great amount of progresses have been made in the field. Distances have become larger: beyond planetary distances in the Solar System at the astronomical unit scale (1 AU = $149.60 \cdot 10^9$ m), investigations include the parsec scale (1 pc = $30.857 \cdot 10^{15}$ m) - distances to nearby stars - up to distances to nearby galaxies at the mega-parsec scale.

To investigate in depth the close-by celestial sites, as well as remote and hidden regions in the very far Universe, the modern astronomer can count on very sophisticated apparatuses, in which not only traditional optics with lenses and mirrors is involved. Nowadays, to get a most complete description of a celestial object, astronomers put together data and results from very different experiments, combining different experimental techniques.

Modern observations are made in all parts of the spectrum, including X-rays and radio-frequencies, using both terrestrial and orbital instruments and space probes. Modern astronomy is, in one word, multi-wavelength: optical astronomy (light in the visible band) is complemented by radio astronomy and X-ray astronomy, as impressively shown in Figure 2. Investigations performed collecting electro-magnetic radiation constitute astronomy with photons.

But this is not enough, yet. Astronomy can be performed even *without photons*. Not only the photons, in fact, can carry out information from the far Universe: cosmic rays and neutrinos can be added in the list of messengers able to give indirect observations of the sky. And moving apart from particle physics, one can consider also the role of gravitational waves in the astronomical research.What presented is the ***multi-messenger*** approach, that connects astronomy with astrophysics and particle physics, and opens new windows in Cosmology and in the theory of gravity, giving some hints of new physics beyond the Standard Model.

The multi-messenger approach is mainly a complementary source of information for photon-astronomy, but the case of neutrinos is slightly different. Because of their

Figure 1: *Galileo e Milton*, by Cesare Aureli (1844-1923), marble. Physics Department, "Sapienza" Università di Roma (photograph courtesy of A. Biagioni). John Milton was so impressed by his meeting with Galileo Galilei that he recalled the Italian scientist and the miracle of his telescope in his masterpiece, *Paradise Lost*.

peculiar interaction properties, in fact, neutrinos not only can provide additional information to complete the picture produced by all-wavelength photon astronomy, but they can offer unique opportunities to look further away and deeper inside astrophysical objects.

As sketched in Figure 3, and as it will be presented in more details in Chapter 1, photons interact both with matter and with radiation, and therefore they are absorbed during their propagation through the interstellar medium. The same can be stated concerning particles such as protons, neutrons and nuclei. Charged particles, in addition, are deflected by magnetic field.

On the contrary, neutrinos only interact weakly, having no electric charge, neither nuclear charge. Total cross section is small, and probability of interaction goes with target density. Therefore, moving inside the low-density interstellar matter and propagating through the intergalactic space, they have really a little chance to meet a target particle and interact. This means that their journey, from the astrophysical sources, where they have been generated to the Earth, where they will be possibly collected by our detectors, has carried on unperturbed. In other words, neutrinos possess pointing properties and preserve directional information, enlarging the horizon of investigations.

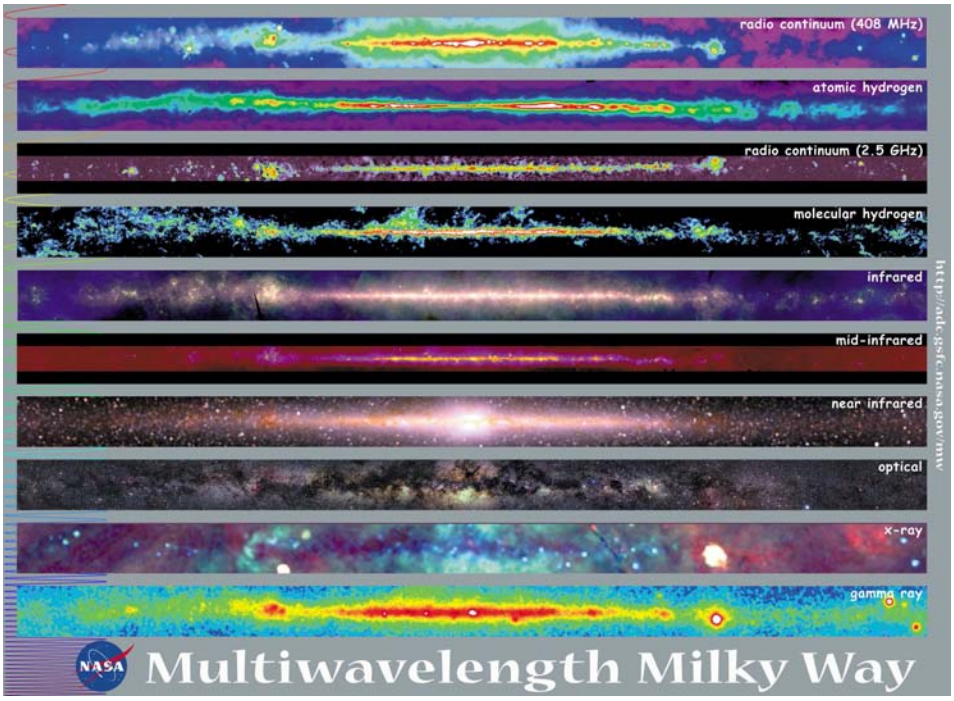

Figure 2: Multi-Wavelength Milky Way. The picture is built up collecting results from several observations, obtained with different experimental techniques. Picture taken from `http://mwmw.gsfc.nasa.gov/`, additional information and detailed references are available therein.

The other side of the coin concerns neutrino detection. Since a particle can be detected only if it interacts with the detector, producing a signature of its passage, the identification of the weakly-interacting neutrino becomes a tough task to accomplish. In particular, considering the case of cosmic neutrinos, a twofold problem has to be faced. A very massive detector is required to offer a significant target for neutrino interaction and, at the same time, detector effective surface has to be large, in order to collect the largest number of events, since the predicted flux of cosmic neutrinos is very low, and decreasing with increasing neutrino energy. The most straightforward choice to fulfill both requirements is thus ruling out a traditional laboratory and exploiting natural targets, as oceanic mass or Antarctic ice.

Going into details of detection techniques, and considering, for instance, the submarine environment, the concrete solution is a huge underwater infrastructure made up of a regular disposal of photomultiplier tubes (PMTs), able to collect the Cherenkov light emitted as a consequence of the passage in water of the charged leptons produced in neutrino interaction with nucleon target in water. This solution, labeled as "Cherenkov" or "optical" technique, constitutes the present development in the field of cosmic neutrino detection and it is practical up to instrumented volumes of about 1 km^3, corresponding to an energy threshold for neutrino events of about $10^{16-17} eV$.

Future developments include the **acoustic technique**, that is a valid and promising strategy to complement and extend Cherenkov apparatuses, in order to get an effective volume of detection of several kilometers cube and to open the possibility of

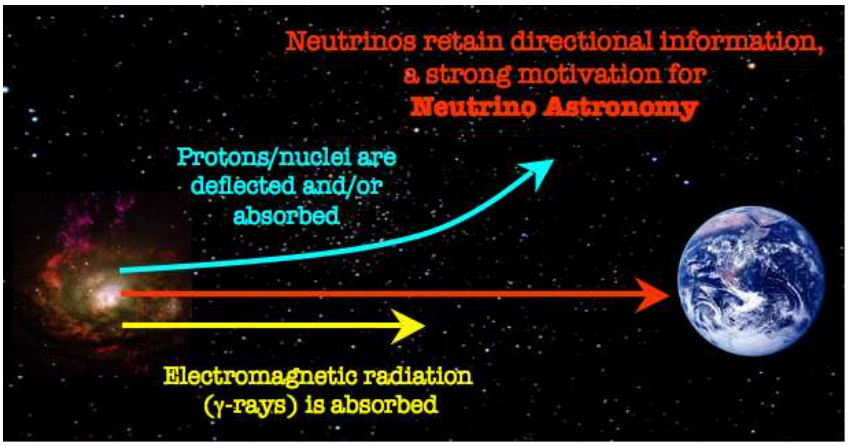

Figure 3: Neutrino-Astronomy. The sketch points out the main motivation for looking at neutrinos in the frame of multi-messenger astronomy. On the left side, a far away cosmic accelerator is depicted, assumed as source of cosmic messengers, as charged particles, gamma-rays and neutrinos. Gamma-rays (photons) are affected by electro-magnetic interaction and may be absorbed during their propagation. Effects of electro-magnetic interaction on charged particles (protons and nuclei) produce particles absorption and deflection by magnetic fields, causing the loss of pointing proprieties. On the contrary, neutrinos are weakly interacting, and therefore they can travel unperturbed through the low-density interstellar medium, able to reach the Earth, where they eventually may be detected, preserving directional information on the cosmic source and opening a new window of observation for astronomy.

investigating neutrino events with energy above $10^{18} eV$. Since the acoustic technique is still in a pioneering stage, detailed studies on the opportunity and the feasibility of the acoustic solution for neutrino detection are needed, and such investigations constitute the main topic presented and discussed in this thesis.

In a literary sense, a *telescope* is something "to see at a distance", and therefore every instrument designed to make distant objects appear nearer is a telescope. This is why we call "telescopes" the deep-sea infrastructures, made up of PMTs or hydrophones, able to identify the passage of particles produced in neutrino interactions: a neutrino signature in the very depths of the ocean could provide indications of something happening very far away in the Universe.

The material presented in this thesis is organized in five chapters.

Chapter 1 is on the scientific motivations for neutrino astronomy, in the frame of multi-messenger astronomy and in connection with astrophysics and cosmology. Some attention will be payed to the possible high-energy neutrino sources; a section will be dedicated in particular to the so-called "GZK" neutrinos. The last part of the chapter concentrates on the challenge of neutrino detection, giving a short essay on the experimental techniques involved. As a conclusion, a report on the experiments presently operating and on future projects is given, paying attention in particular to underwater telescopes.

Chapter 2 goes deeper into details of the acoustic techniques for particle detection, starting from the Askaryan formulation of the thermo-acoustic mechanism. The chapter develops the quantitative aspects of the topic, and gives some indications

on technological resources connected to sound propagation in the sea, including a list of activities operating in the field of acoustic detection of high energy neutrinos.

Right after the description of the thermo-acoustic mechanism, the next step consists in investigating the performances of the acoustic detection. This is the main goal of the activity described in **Chapter 3**, which is dedicated to test measurements performed with proton beams at the ITEP accelerator facilities. The chapter includes a description of the experimental set-up, an account on data analysis and a discussion on the full simulation chain (from the Monte Carlo of the acoustic source up to the acoustic pulse computation). The last part is a report on the results: investigations on the performances of the simulation, a comparison between acquired and simulated pulse, a comparison with results from past experiments at proton beams. In addition, combining results from data analysis and Monte Carlo simulation, it is possible to get some indication on parameters that stayed undetermined during the data taking. The material presented in Chapter 3 is a conclusive report on the ITEP test beam experiment and it represents a good starting point for future developments, both in calibrations (acquired experience and software achievements can be used to plan experiments at test beams) and in the study of the neutrino case.

Some preliminary results concerning neutrinos are presented in **Chapter 4**, that includes expected signals from neutrino-induced hadronic showers. Predictions are compared with results proposed by others groups operating in the field of acoustic detection of high energy neutrinos.

Chapter 5 is for conclusions and perspectives, with strong recalls to what stated in the previous chapters.

In addition, three appendices are included, where specific discussions on source codes and results are accounted. **Appendix A** presents a detailed report of the simulation code reproducing the ITEP test beam, including a general description of the Geant4 toolkit. **Appendix B** goes deep into details on the Geant4 Monte Carlo simulation results. In **Appendix C**, the full AcPulse code used to compute acoustic pulses is included.

Chapter 1

Neutrino Astronomy and Neutrino Detection

1.1 Astro-Particle Physics, the Multi-Messenger Approach and Neutrino Astronomy

As already underlined in the Introduction, one of the most promising perspective in the astrophysical research is the opportunity of a multi-messenger approach [1] [2]. Astrophysics, particle physics and cosmology can profit from such investigations.

Concerning **High Energy Astrophysics**, astro-particle physics is a well established field of research [3] [4], offering the opportunity to investigate the nature and behaviour of the so-called "cosmic accelerators", where ultra-high-energy particles are produced. Supernovae remnants (SNRs), galactic microquasars, pulsars, gamma ray bursts (GRBs), active galactic nuclei (AGNs) are some examples of astrophysical objects and phenomena from which a flux of high energy particles is expected. The detection of astro-particles constitutes a probe of the acceleration mechanisms taking place in the core of cosmic engines. The topic is connected with physics of stars and stellar evolution, quantum and classical electrodynamics, plasma physics and magnetohydrodynamics, physics of galaxies, special and general relativity. Gravitational theory also plays a role since black holes, binary systems and explosive events in the Universe are connected with gravitational waves emission (Section 1.1). Additional details on cosmic ray sources will be listed in Section 1.2, paying attention in particular to neutrinos.

Particle Physics comes into play since cosmic engines, as the ones listed above, can accelerate particles up 10^{20} eV and beyond (Figure 1.1), and such energies will never be available in human-made accelerators[1]. In this sense, astro-particle physics comes back to its origin, when particles coming from the sky were the only source for investigations in the sub-atomic zoo. The history dates back to 1912, with the first evidence of cosmic radiation experienced by Victor Hess, and extends up to

[1] At present, the highest-energy particle accelerator is LHC - Large Hadron Collider (`http://lhc.web.cern.ch/lhc/`) at CERN, that is designed for proton-proton collisions, foreseen at an energy of 7 TeV per beam. LHC represents the frontier in the field of particle accelerators, and considering the current technological skills and knowledge, LHC limits seem to be very hard to overcome.

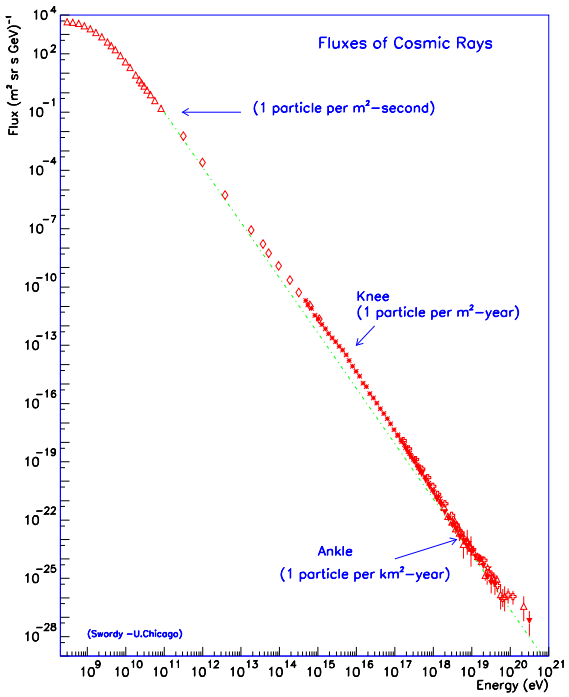

Figure 1.1: Cosmic ray spectrum. Picture by S. Swordy [5].

the '50s, when the first accelerators entered in operation. In the meantime, several discoveries occurred, as in evidence in Table 1.1, taken from [6]. An historical review on cosmic rays is in [7].

Particle	Year	Discoverer	Method
e^-	1897	Thomson	Discharges in gases
p	1919	Rutherford	Natural radioactivity
n	1932	Chadwik	Natural radioactivity
e^+	1933	Anderson	Cosmic Rays
$\mu^\pm$	1937	Neddermeyer, Anderson	Cosmic Rays
$\pi^\pm$	1947	Powell, Occhialini	Cosmic Rays
$K^\pm$	1949	Powell	Cosmic Rays
π^0	1949	Bjorklund	Accelerators
K^0	1951	Armenteros	Cosmic Rays
Λ^0	1951	Armenteros	Cosmic Rays
Δ	1932	Anderson	Cosmic Rays
Ξ^-	1932	Armenteros	Cosmic Rays
$\Sigma^\pm$	1953	Bonetti	Cosmic Rays
p^-	1955	Chamberlain, Segrè	Accelerators
anything else	1955→today	various groups	Accelerators
$m_\nu \neq 0$	2000	KAMIOKANDE	Cosmic Rays

Table 1.1: Discovery of elementary particles. The leading role of cosmic radiation is in evidence. Table from [6].

It is of interest that the last line in Table 1.1 turns back to cosmic rays. Indeed, it must be noticed that neutrino physics has lots to do with cosmic rays, and most of the present understanding comes from astrophysics and cosmic radiation experiments [8] [9] [10], providing in return further upshots for the astrophysical research.

Additional information on astrophysics probes of particle physics can be found in [11].

The open questions concerning the origin of cosmic rays and acceleration mechanisms give also the opportunity to set up a link with **Cosmology**, in particular when taking into account ultra-high-energy particles (energies above 10^{18} eV). The existence of such particles coming from the Universe is a fact, and the research activity looks for Standard Model interactions and for hints of new physics (strong interacting neutrinos, violation of the Lorentz invariance) [12] [13] [14]. In particular, top-down models, as annihilation of WIMPs (Weakly Interacting Massive Particles), Z-burst mechanisms and decay of topological defects and of any other components of super-symmetric matter or massive non baryonic dark matter, are in the list of phenomena than connects ultra-high-energy cosmic ray detection with the early stage of evolution of the Universe [15] [16]. In this field, also, cosmic neutrinos play a crucial role in supporting cosmological theories and providing extensions of the Standard Model, as widely accounted in [17].

The quick glance given in this section is enough to identify astro-particle physics as a rich and multi-disciplinary field of study, with several interlinked and correlated activities, and with a dominant position filled up by neutrinos. The importance of neutrinos, beside the already mentioned facts concerning astrophysics of cosmic engines, neutrino physics and cosmology, becomes decisive if **Astronomy** is accounted. Astro-particle physics, and neutrinos in particular, in fact, can make available a new point of view in astronomy.

The astronomer is the cartographer of the sky, in a sense that for both the purpose is to draw up a map where the main features are located. Therefore, astronomy is strongly connected with the opportunity of investigating the origin of cosmic messengers. In this frame, the role of neutrinos in the multi-messenger approach of the astrophysical research can get crucial, because of neutrino peculiar interaction properties: as weakly interacting neutral particles, in fact, they are not absorbed in their propagation, nor deflected by magnetic field (Figure 3 in the Introduction). If a cosmic neutrino is detected, and if the neutrino direction is reconstructed, the neutrino origin can be extrapolated tracking back the way from the detector to the source.

Nevertheless, it must be underlined that when the pointing information cannot be available, the so-called *diffuse flux* of events (considering charged cosmic rays, photons, neutrinos and gravitational waves) is still of major importance, as the listed above topics in Astrophysics, Particle Physics and Cosmology widely document.

In the following, I will discuss some features of the physics of cosmic radiation, in particular considering some experimental aspects in the framework of the multi-messenger approach. Information are reported with no claim to be exhaustive, but with the only purpose to give a glimpse on the most relevant topics related to neutrino astronomy and astrophysics.

Protons/charged nuclei As known from elementary physics, charged particles do not travel along a straight line, if they move in a region of space where a magnetic field is present, and this is the case of the galactic environment. Therefore, as a consequence of galactic magnetic fields, our Galaxy is filled up with a so-called *diffuse flux* of cosmic rays, for which the pointing properties are lost. As a consequence, the opportunity to extract astronomical details is ruled out, but the diffuse flux of cosmic rays still provides a fruitful source of information for physical research, as widely discussed in [18].

For a back-of-the-envelope computation, we can follow the formulation used in astro-particle physics of the gyroradius, or Larmor radius r_L, in the relativistic case:

$$r_L[cm] = \frac{1}{300} \cdot \frac{E[eV]}{Z \cdot B[G]} \tag{1.1}$$

Here E is the particle energy in eV, B is magnetic field in Gauss, Z is the atomic number. Taking for instance a proton ($Z = 1$), selecting $B = 3\mu$G (average value in the Milky Way[2]), and assuming that the thickness of the galactic disc is approximately 150 pc, it can be computed that an order of magnitude of 10^{18-19} eV in energy is required to escape the magnetic confinement [21]. It must be added that, as far as we know, there is no evidence of any galactic source able to accelerate particles up to energies above the computed threshold [22]. Therefore, considering the Larmor radius, we can state that the energy of galactic cosmic rays is not enough to let particles escape from the "magnetic trap" due to the galactic magnetic field.

With analogous reasoning, we can move away from the Milky Way and consider the case of a charged particle produced in some outer galaxy. The accelerated particle can escape the magnetic confinement of the source galaxy and reach our detectors only if its energy is high enough that the corresponding gyroradius exceeds the radius defining the size of the source galaxy. Assuming for the magnetic field and size of the outer galaxy the same values considered for the Milky Way, we thus expect to detect extra-galactic particles if energy is of the order of 10^{18}eV or above (the so-called "ankle" in the cosmic-ray spectrum) [23] [24]. Cosmic ray propagation in the magnetic field of a spiral galaxy is illustrated in Figure 1.2.

Since a large gyroradius means an - almost - straight line trajectory, ultra-high energy particles preserve directional information on the astrophysical source, and therefore they can be considered for astronomical observation. In other words, for what concerns cosmic rays, astronomy is possible only with ultra-high-energy particles, that are supposed to have extra-galactic origin.

The possibility of employing ultra-high-energy cosmic rays for astronomy has been recently confirmed by the latest results from the Pierre Auger Observatory [26], that show evidence of some anisotropy in the high energy cosmic ray distribution. Moreover, considering the directional information associated with the detected high energy events, the Auger Collaboration has been able to reconstruct the position of the cosmic ray sources on a sky-map. In some significant cases, these reconstructed positions stay in coincidence with Active Galactic Nuclei (AGNs) [27].

[2]Diffuse studies have been carried on to explore the detailed features of the galactic magnetics field. Theoretical models, numerical simulations and hints from observations provide refined information on particle propagation and on high-energy cosmic ray trajectories [19] [20].

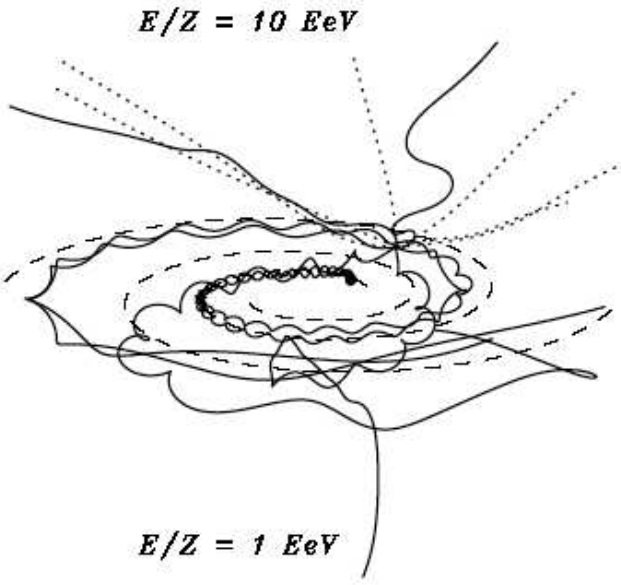

Figure 1.2: Cosmic rays propagation in the galactic magnetic field. Examples of trajectories of nuclei for different ratios of energy over charge: $E/Z = 1$ EeV - solid lines - and $E/Z = 10$ EeV - dotted lines - ($1\,EeV = 10^{18}\,eV$). The dashed lines indicate the spiral arms of the galaxy. At the lower energies particles start to be trapped by the spiral structure of the regular galactic magnetic field. Picture taken from [25].

The first Auger sky-map (Figure 1.3) constitutes a preliminary validation of the hypothesis that states AGNs as the most important candidate sources for high-energy extragalactic cosmic rays. Pierre Auger Observatory results thus open concretely the opportunity of cosmic-rays astronomy.

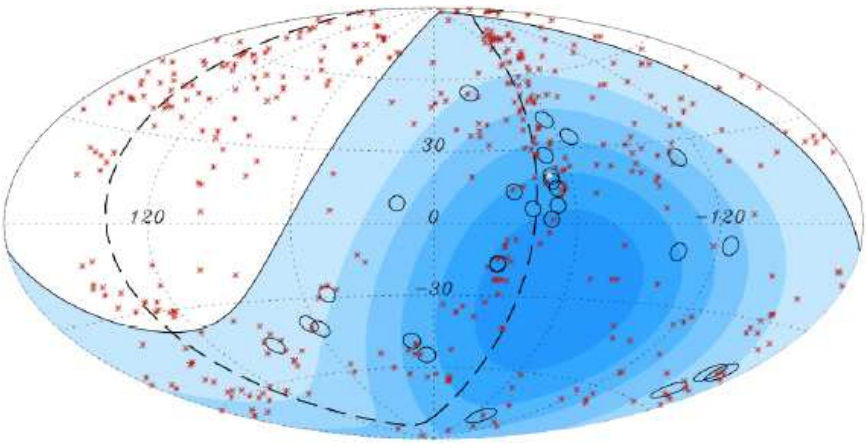

Figure 1.3: Pierre Auger Observatory sky-map (galactic coordinates). Circles are centered around the arrival directions of 27 cosmic ray detected events with energy E>57 EeV. Asterisks identify the positions of the 442 AGN (292 within the field of view of the Observatory). The solid line draws the border of the field of view of the Observatory. The dashed line is the super-galactic plane. Darker colour indicates larger relative exposure. Centaurus A, one of the closest AGN, is marked in white. From [27].

When considering cosmic rays with energy above 10^{19}eV and recent results of the Pierre Auger Observatory, an additional comment should be accounted, concerning the so-called GZK cut-off. Some details and a list of reference will be given in Section 1.2.

Photons Concerning photon-astronomy, the limit is not of course connected with pointing properties of particles: as already discussed in the Introduction, traditional astronomy is basically astronomy with photons. Neutrinos step forward when considering the problem of the opacity of celestial objects to electro-magnetic radiation.

It must be noticed that one of the main motivation for multiwavelength observations in modern astronomy is to overcome the case of cosmic objects not transparent to visible light. Combining information from the full electro-magnetic spectrum, is it possible to approach a comprehensive understanding of celestial sites and phenomena. Check, for instance, [28] [29] [30], and [31] for a general description of the multiwavelength approach.

Still, there are regions in the Universe (very far away or very dense sites in celestial objects) that cannot be "seen", in a sense that no electro-magnetic radiation of any wavelength can escape, since photons are very "fragile" components, absorbed in interactions with matter and radiation. This means that phenomena such as the inner dense core of cosmic sites or the burning of astrophysical engines cannot be explored with photon astronomy. On the contrary, poor interacting neutrinos can travel unperturbed through matter and radiation, and can help in discovering or exploring "hidden" accelerators. A common case of this kind is the Sun: despite the fact it is one of the first investigated objects in the sky, the core is optically thick, that is not observable in photons. Only neutrinos, emitted as a consequence of the burning mechanisms in the stellar core, can escape from the inside and be detected, offering an alternative point of view on the star. A popular example is the picture of the Sun in neutrinos, or neutrino heliograph, provided by the Super-Kamiokande experiment (Figure 1.4).

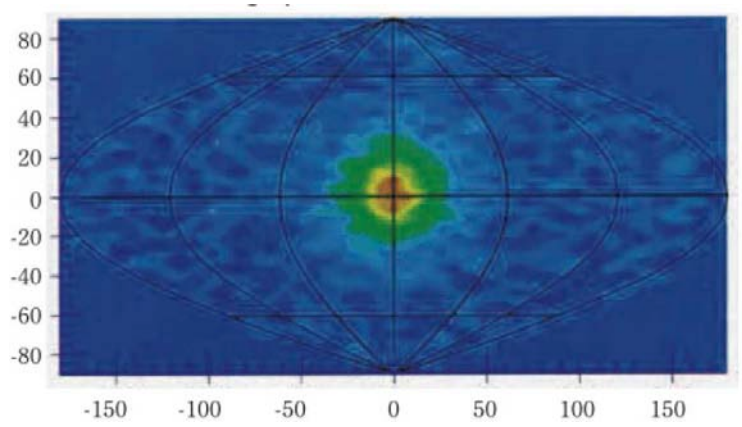

Figure 1.4: Neutrino Heliograph measured by Super-Kamiokande. Picture taken from the Kamioka Observatory Pamphlet 2006, Institute for Cosmic Ray Research, the University of Tokio, Japan (available on line at `http://www-sk.icrr.u-tokyo.ac.jp/lib/` - in Japanese). Additional information on the Super-Kamiokande neutrino heliograph can be checked in [32].

Concerning high-energy gamma astronomy, the most important connection with neutrino-astronomy is related to the opportunity of investigating the nature and behaviour of gamma accelerators. In particular, neutrinos can work as a valid tool to solve the hadronic/leptonic puzzle. The point is that gamma rays can be produced in cosmic accelerators by two mechanisms: a *leptonic mechanism*, with electrons accelerated in cosmic engines and photons produced as a consequence of synchrotron emission, bremsstrahlung, inverse Compton scattering, and a *hadronic mechanism*, following the model according to which primary accelerated particles are protons. Such primary protons interact with ambient matter in the source and produce pions, present in both species (charged and neutral); pion decays give birth to muons and photons, respectively. Muon interactions at the source are then accompanied by the production of neutrinos. Considering the mixing properties of neutrinos, and since a full-mixing is expected, a fixed ratio of neutrinos and gamma is predicted. Such processes of neutrinos and gamma production are usually referred to as *astrophysical beam dumps* [33]. Therefore, high-energy gamma ray astronomy and neutrino astronomy are closely associated, and often go hand in hand when considering expected or observed fluxes of events from astrophysical sources.

In this framework of a special relationship between gammas and neutrinos, it is crucial the role of experiments like H.E.S.S. (High Energy Stereoscopic System) [34] and MAGIC (Major Atmospheric Gamma-ray Imaging Cherenkov Telescope) [35]. Both experiments exploit the Cherenov imaging technique to detect gamma-ray induced particle showers in atmosphere. Tracing back the detected events, several gamma-ray sources are identified in the sky.

Theoretical models predict different spectra of photon emission and energy distribution, depending on which is the assumed the dominant mechanism of gamma-ray production in the astrophysical source, considering the leptonic or the hadronic description. Therefore, observations carried on with gamma-ray telescopes may discriminate between the two pictures. An example is discussed in [36], and illustrated in Figure 1.5. If results of gamma-ray telescope observations are in favour of the hadronic mechanism, a guaranteed and predictable neutrino flux from the identified gamma-source is expected as a consequence. At the same time, a neutrino detection from gamma ray sources would support the hadronic description, offering an important piece of information about the acceleration phenomena inside the cosmic engines.

In addition, one of the most interesting results of gamma-ray telescopes is that they have discovered several *unidentified sources*, that is several sites in the sky emitting gamma-rays and not identifiable with other known objects. Most of these discoveries are located in the galactic plane, in proximity of the Galactic Centre. See, for instance, references [37] [38] for discussion on discoveries carried on by the MAGIC experiment; [39] for an account on the up-to-date list of H.E.S.S. sources with no-other counterpart and [40], that is a collection of the H.E.S.S. Collaboration contributions at the 30^{th} International Cosmic Ray COnference - ICRC2007. Discovering a neutrino counterpart coming from such unidentified gamma-ray source would help a lot in the identification and would provide fundamental hints to understand the physics behind the observations.

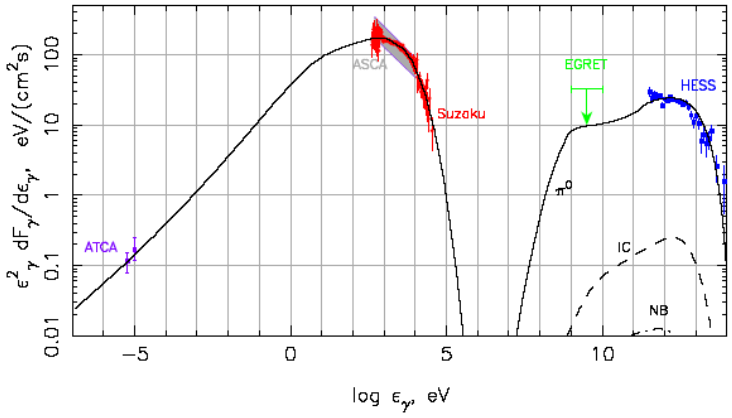

(a) Hadronic-dominated scenario.

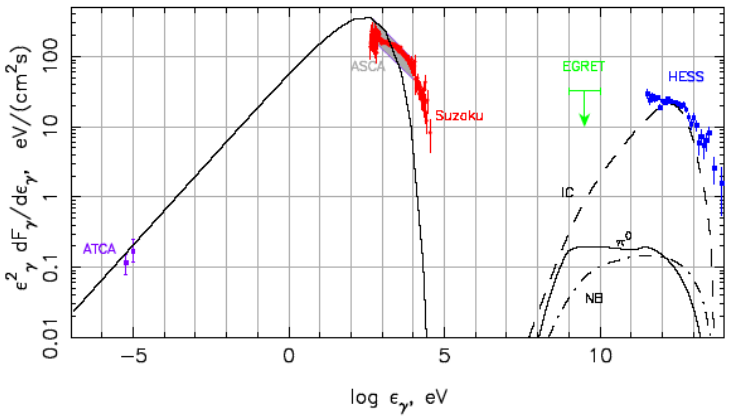

(b) Leptonic-dominated scenario.

Figure 1.5: Hadronic versus leptonic origin of the gamma-ray emission from Supernova Remnant RX J1713.6-3946. Gamma-ray spectral energy distribution. The upper plot shows the computation for a hadronic-dominated scenario (gamma-ray emission from π^0 decay); the lower plot computes the expectations for a leptonic-dominated case. In both plots, models are compared with observations from experiments at different wavelengths. The outcome of the presented study appears to support hadronic mechanisms. Details in [36].

Gravitational Waves As discussed in [41], the list of gravitational waves sources has lots in common with the list of neutrino sources (Section 1.2), and, in analogy with the neutrino case (Section 1.2.1), the signal expected in gravitational wave detectors is very faint. Therefore, it is straightforward to plan collaborations between neutrino telescopes and gravitational waves observatories, in order to join efforts and resources, and employ a cross-calibration procedure to increase the signal-to-noise ratio and the event selection. See, for instance, [42] for a report on coincident events from LIGO[3] and IceCube and [43] for a feasibility study concerning the set up of a collaboration between VIRGO[4] and ANTARES. For details on neutrino telescope experiments, see Section 1.3.2.

1.2 High Energy Neutrino Sources

Entering the details of neutrinos, the starting point can be considered the fundamental works of Gaisser, Halzen and Stanev (1994) [44], Halzen (2000) [45] and Learned and Mannheim (2000) [46]. These reviews offer a large account on physical motivations for neutrino astronomy and astrophysics, and a detailed report on expected neutrino sources and on processes and phenomena whose predicted consequence is a flux of neutrino events. Keeping in mind the wide amount of material discussed in the above cited references, a summary table approach has been chosen to present here the topic of cosmic neutrino sources. Information is listed in Table 1.2. Some details and a list of additional references are given in the next.

<table>
<tr><th>Bottom-Up Models
(Acceleration)</th><th>Top-Down Models
(Annihilation/Decay)</th></tr>
<tr><td>Galactic
SNRs
Pulsars/PWNe
Microquasars</td><td rowspan="2">WIMPs
TDs
Z-bursts</td></tr>
<tr><td>Extra-Galactic
AGN
GRB</td></tr>
<tr><td colspan="2">GZK</td></tr>
</table>

Table 1.2: Cosmic Neutrino Sources. Listed items are grouped in three sets: bottom-up models, that identify the cosmic accelerators, with the two sub-sets of galactic and extra-galactic sources; top-down models, that include tips from cosmology and processes of new physics; cosmogenic neutrino flux, due to the GZK cut-off of the cosmic-ray spectrum.

About the grouping given in the table, the term "bottom-up" recalls to acceleration processes, since it refers to the fact that, through several repeated interactions with matter and radiation, particle energy raises from a lower value up to the final higher value. On the contrary, the term "top-down" underlines that the emitted particle comes from a single process of decay (or annihilation). In general, acceleration

[3]LIGO is Laser Interferometer Gravitational-wave Observer, located in U.S.A. `http://www.ligo.caltech.edu/`

[4]VIRGO is the interferometric gravitational wave observatory in Italy `http://www.virgo.infn.it/`

models mainly reflect predictions of standard model physics, while top-down models require hints of new physics.

GZK neutrinos fill a separate cell in the table, since they constitute the so-called cosmogenic diffuse flux of events, and cannot be associated to a specific source or location in the Universe.

Concerning acceleration models, the reference process that allows particles to gain energy through collisions with plasma nebula is the so-called Fermi mechanism, that was originally proposed by Fermi in 1949 [47] [48]. The Fermi hypothesis has been revised and extended in the years, including the contribution of *shock waves* in plasma [49] [50], but substantially it is still regarded as the fundamental explanation of the cosmic rays acceleration in astrophysical environments.

The subdivision in galactic and extra-galactic sources helps to make up a catalog of candidate emitting neutrinos sites in the Universe, and it is important mainly to look for correlations with results and discoveries from other experiments (Pierre Auger Observatory, MAGIC, H.E.S.S.). A report on galactic sources, and galactic source candidates in correlation with gamma-astronomy, is discussed in [51]. A summary on extra-galactic sources of high-energy neutrinos is in [52].

SuperNova Renmants (SNRs) Supernova remnants are what is left behind after a supernova, that is the gigantic explosion constituting the very last step of stellar evolution. Shock waves in supernova remnant environments fulfill the conditions for the occurring of the Fermi mechanism. Supernova remnants are, at present, the best candidate galactic sources for cosmic ray acceleration up to energies of about $10^{15}eV$ [53]. Neutrino fluxes are predicted according to astrophysical beam dump model.

Pulsars/Pulsar Wind Nebulae (PWNe) A separate case of supernova remnant is represented by pulsar wind nebulae, or plerions. The pulsar is a rapidly rotating neutron star, resulting from the gravitational collapse of the stellar matter during a supernova event, and surrounded by a nebula of relativistic particles and magnetic flux. According to theoretical predictions, particles accelerated in pulsar-driven SNRs can reach higher energies (up to about $10^{18}eV$ [54]). More on acceleration in PWNe and neutrino flux predictions in [55] and [56].

Microquasars X-ray binaries are systems made up of a compact object (black hole, neutron star) and a companion non-compact star, with mass transfer phenomena, through accretion disc, from the non-compact to the compact object. Microquasars are X-Ray binaries whit jet emission.

Theoretical models predict shock waves in the microquasar environment, with a subsequent particle acceleration, and neutrino production as the effect of astrophysical beam dumps. An estimate of the flux of neutrino events from galactic microquasars is computed in [57]. The results of this study indicate microquasars as very promising sources of neutrinos with energy of the order or 100 TeV.

Microquasars take their name from the fact that, because of the presence of the accretion disc and of relativistic jets, they can be considered small scale reproductions of quasars. Since physics processes in microquasar environments resemble phenomena occurring in active galactic nuclei (AGNs), exploring microquasars with

neutrino probes can give the opportunity to achieve a better understanding of such phenomena, providing some hints in the comprehension of the physics of quasars and AGNs.

Active Galactic Nuclei (AGNs) The AGN unified model assumes a supermassive black hole ($M \sim 10^8 M_\odot$), placed in the center of the active galaxy, and characterized by the presence of accretion disc and jet emission. AGNs constitute the most efficient continuous source for cosmic ray acceleration and ultra-high-energy particle emission. Both leptonic (electro-magnetic interactions) and hadronic (strong interactions) acceleration processes are predicted with, in the latter case, an expected (and correlated) flux of gammas and neutrinos. Neutrino-astronomy, thus, could provide the chance to investigate the inner core of the AGN engine, that is supposed to be the most powerful energy source in the Universe [58]. Nevertheless, still large uncertainties in the number of neutrino events are present, because, as in evidence in Figure 1.8, predictions from different models of AGNs produce variations in results [59] [60].

Gamma-Ray Bursts (GRBs) The term gamma-ray burst is referred to an impulsive phenomenon of violent gamma-ray emission, representing the most energetic transient source emitting radiation in the Universe. GRBs constitute a fascinating topic in astrophysics, since the origin of such phenomena is still not completely resolved. For a review of gamma-ray bursts, check [61].

Neutrino emission is predicted in coincidence with gamma emission[62]; GRBs observations in neutrinos would help in the understanding of the processes involved. It is of importance, thus, to check for coincidences of neutrino events with gamma-ray burst alerts. Concerning, for instance, the ANTARES neutrino telescope, a Gamma-Ray Burst trigger has been implemented, to get satellite triggered data taking. The activity is ongoing, and it is documented in [63]. Again, the purpose is in the line with the plans of cross-calibrate the detector, in order to place neutrino telescope data side by side with outcomes from different experiments.

Top-down models have been proposed in the framework of the so-called GZK "puzzle", that is to offer an explanation for super-GZK particles, going beyond the Standard Model of particle physics. The topic is strongly connected with several aspects of neutrino physics and cosmology. A general discussion on top-down models is presented in [64].

WIMPs (Weakly Interacting Massive Particles) The name WIMP identifies a generic class of particles introduced to solve the Dark Matter puzzle in the Universe. A WIMP is a massive, long-lived and weakly interacting particle, trapped in the core of the Sun, or of the Earth, or in the Galactic center. WIMP particle-antiparticle annihilation would produce a flux of neutrinos, whose energy would be a significant fraction of the WIMP mass [65]. Detecting such a neutrino signature would place neutrino telescopes in the field of indirect search of dark matter.

Predictions on neutrinos from WIMPs suffer the multiplicity of hypothesis proposed in the frame of supersymmetry, producing, as a consequence, a huge amount

of unknown parameters in the models. In the rich cauldron of supersymmetric theories, the neutralino appears to be the best candidate to play the role of WIMP in cosmology; but still large uncertainties exist concerning the neutralino mass.

Results concerning WIMPs annihilation investigated with the AMANDA neutrino detector are presented in [66]. Prospects on indirect dark matter search with the ANTARES neutrino telescope are discussed in [67].

Topological Defects (TDs), Relic Particles and other Top-Down Models Magnetic monopoles, massive relic particles and topological defects are in the list of phenomena assimilable to WIMPs, in a sense that decay or annihilation processes could produce a flux of ultra-high-energy particles and neutrinos [68] [69]. Concerning uncertainties in the predictions, the same warnings advanced about the WIMP case are valid, because of the large number of unknown parameters in the several accounted models.

Z-bursts Roughly speaking, the Z-burst process consists in the annihilation of ultra-high-energy neutrinos on relic neutrinos of the cosmic neutrino background CνB[5], with the resonant production of the Z-boson [72] [73] [74]. Ultra-high-energy cosmic rays ($E > 10^{20} eV$) are predicted as a consequence of the Z boson decay, offering an explanation for ultra-GZK detected events, and providing a source for neutrinos in the PeV region (see Figure 1.9).

An important limit of this model consists in the fact that, since the energy of the CνB is very low, neutrinos with energy of the order of $10^{21} eV$ are required to drive the resonant production of Z bosons. Therefore, in some sense, the problem moves upstream: the Z-burst mechanism has been devised to explain the occurrance of high-energy cosmic rays but, in order to have neutrinos energetic enough for the Z resonance, it asks for the existance of ultra-high-energy neutrino sources.

GZK-Neutrinos At last, after so many mentions in the above paragraphs, I am going to deal about the GZK cut-off, that plays a crucial role in the physics of ultra-high-energy cosmic rays, and assume a decisive importance when considering neutrinos. Indeed, as already pointed out, a class of theories (the top-down models) has been devised to face the consequences of the GZK cut-off on the flux of cosmic ray events at Earth.

The first formulation of the GZK effect dates back to 1966 with the work of Greisen [75], Zatsepin e Kuzmin [76], from which the process takes its name. After the discovery of the CMBR (note 5), in fact, the question was to investigate if the presence of a diffuse low-energy background radiation, filling isotropically the entire Universe, could be a limit for cosmic ray propagation.

[5] Analogous to the Cosmic Microwave Background Radiation (CMBR), the cosmic neutrino background (CνB) is a Big-Bang relic isotropic diffuse background of very low energy neutrinos. The CνB temperature is estimated at about 1.95 K, to be compared with the value of about 2.7 K characterizing the CMBR. The reason because the neutrino background is cooler (and therefore, less energetic) than the photon background is due to the fact that CνB is "older" than CMBR, since neutrino decopuling occurred about $2s$ right after the Big Bang, while photons decoupled about 380000 years later. More on the early Universe in [70] [71].

Going into details, the point is that, according to particle physics, high-energy protons can interact with low energy photons, with resonant production of Δ^+ baryon, whose decay gives birth to pions (photopion production), turning into muons, and therefore into neutrinos in the final state. A schematic representation of the processes involved is given in Figure 1.6.

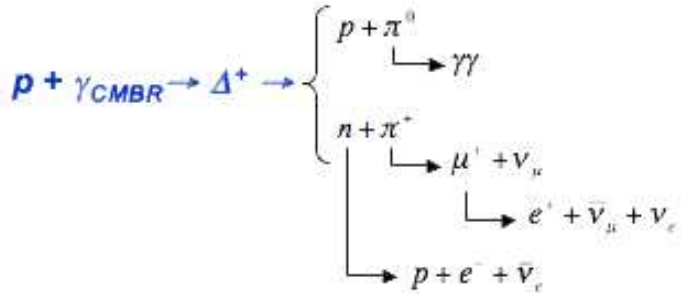

Figure 1.6: GZK effect: high-energy proton interaction with CMBR, with resonant production of Δ^+ baryon. A schematic representation of the decay chain that gives birth to neutrino production. Neutrino mixing assures the presence of all the three flavour states in GZK neutrino events.

Considering relativistic kinematics,a back-of-the-envelope computation[6] results in the value $E_{p,th} \sim 5 \cdot 10^{19}$ eV for the order of magnitude of the energy threshold of the process. In addition, one can estimate the mean free path of protons with the formula: $\lambda = (\sigma \cdot n)^{-1}$ (σ is the average cross-section of the process; n is the CMBR photon density), getting an order of magnitude of some tens of mega parsecs. The conclusion concerning cosmic ray detection is that the cosmic ray spectrum should manifest an abrupt steepening (cut-off) at energies around $E_{p,th}$. Indeed, if ultra-high-energy protons are produced somewhere in the Universe further away than the distance defined by λ, they cannot travel up to the Earth, because they will experience, on average, resonant interaction with background photons.

It must be noticed that gamma-rays also suffer of interaction with CMBR. In this case, the process is a pair production mechanism (creation of an electron-positron pair), whose threshold is at about $E_{\gamma,th} \sim 10^{14}$.

In recent years, a lot of debate has arisen about the GZK-effect, because of the so-called GZK "puzzle", that is the paradox of registering ultra-GZK events, in contrast with the predictions of the theory. In particular, results from the AGASA experiment[7], showing events beyond the GZK threshold [77], have opened way to speculations to overcome the constraints of the GZK. An account on activities and discussions about "GZK and surroundings" is documented in [78].

Nowadays, as already anticipated, latest results of the Pierre Auger Observatory confirmed the GZK cut-off [79], attesting a decrease of the cosmic ray flux at energies above about $4 \cdot 10^{19}$ eV, in agreement with the last released outcome presented by the HiRes[8] experiment [80]. Results are shown in Figure 1.7.

[6] More accurate computations should take into account the details of the CMBR energy spectrum and the tails of the energy distribution of background photons

[7] AGASA is Akeno Giant Air Shower Array, a surface detector in Japan, in operation in the '90s. AGASA reported a cosmic ray spectrum with evidence of violation of the GZK predictions.

[8] The HiRes experiment is a fluorescence experiment studying UHE cosmic rays.

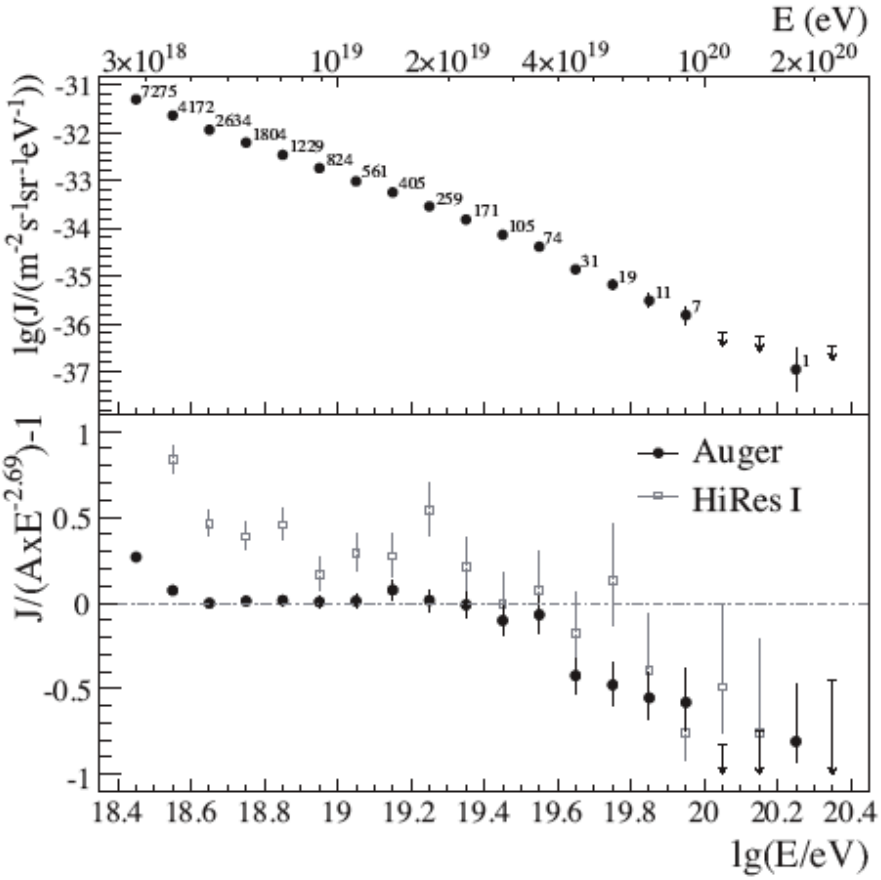

Figure 1.7: Evidence of the GZK cut-off from results of the Pierre Auger Observatory [79]. Upper panel: differential flux as a function of energy. Lower panel: comparison with results of the HiRes experiment, and with a spectrum with an index of 2.69.

It is important to underline that the confirmation of the GZK effect is associated with a guaranteed ultra-high-energy neutrino flux (GZK-neutrinos). As illustrated in Figure 1.6, neutrinos are predicted as a consequence of protons interaction with cosmic microwave background radiation (CMBR). Therefore, ultra-high-energy cosmic-rays physics is strongly connected with neutrinos, and the limits of proton propagation translate into a great opportunity in neutrino physics. Detecting GZK-neutrinos would substantiate Auger results and contribute in solving the GZK puzzle.

1.2.1 Neutrino Flux Predictions

Figure 1.8 (energy range: $10^{11} - 10^{20}$ eV) and Figure 1.9 (energy range: $10^{9} - 10^{25}$ eV) report the expected flux of neutrino events according to different predictions and models. I decided to include both pictures, because the first one gives details on the acceleration scenario, while the second one present specific information on top-down models at extreme energies. Results are represented in logarithmic scale, the horizontal axis is energy, the vertical axis is energy flux, given as differential neutrino flux multiplied by E_ν^2.

It is in evidence that neutrinos expected from AGN models become dominant over atmospheric neutrinos[9] for energies above 10^{14} eV, therefore in the range accessible to Cherenkov telescopes (Section 1.3.2). Neutrinos from Gamma Ray Bursts (GRBs) are predicted in the same energy range; they can be distinguished from AGN events considering the directionality and the characteristic time evolution of GRB neutrino signature, and implementing a satellite alert, in coincidence with satellites records, as discussed above.

As it will be accounted in Section 1.3.2, the Cherenkov technique works at its best up to about 10^{17} eV, that is when the acoustic technique can start operating. This energy range corresponds to the value at which GZK and top-down models become dominant over AGN models. The top-down scenario becomes the only one available at energies above 10^{21} eV.

1.3 The Challenge of Neutrino Detection

The fact that neutrinos are weakly interacting is, at the same time, a great opportunity for discoveries in astrophysics and astronomy, and a gigantic obstacle for detection. In addition, to make things more difficult, neutrino flux predictions compute a decreasing number of events as neutrino energy increases (Section 1.2.1). In one sentence, neutrinos are very hard to detect, but high-energy cosmic neutrinos are even harder.

The strategy to catch neutrinos consists in collecting a signature of the passage of the particles. This imply that neutrinos should interact in the proximity of the detector, or inside the detector volume. Therefore, the first requirement a cosmic neutrino detector should fulfill is to be huge, in order to intercept the faint flux of neutrino events at high energies. Moreover, it has to be massive, since a large amount of target nucleons are necessary to provoke a neutrino interaction, because of the small neutrino-nucleon cross section. This two considerations drive to the conclusion that a natural target as to be employed, as oceanic water (or antarctic ice), since no human-made laboratory could ever be large enough to host such an apparatus.

Secondly, if a neutrino interaction has occurred, the telescope should be able to identify the products of the interaction. As it will be accounted section 1.3.1, a neutrino-nucleon interaction can result in hadrons and leptons. Detection techniques differ since they concentrate in discovering signatures of different secondary products of neutrino interactions. In all cases, however, the signal revealing the presence of secondary particles has to be transmitted through the detector volume, in order to be collected and recorded: light, in case of optical Cherenkov telescopes, or sound in case of the acoustic technique (or radio signals, when considering the radio detection in ice). The water volume thus operates as the medium for signal transmission. As it will be discussed in Section 1.3.3, how different light and sound propagate in water is one of the aspects that defines the energy range of application of the two techniques.

[9] Atmospheric neutrinos are neutrinos produced as secondary particles as a consequence of primary cosmic ray interactions in atmosphere. They constitute the background events for neutrino telescopes. Secondary neutrinos are also those one coming from interactions of cosmic rays with matter in the galaxy.

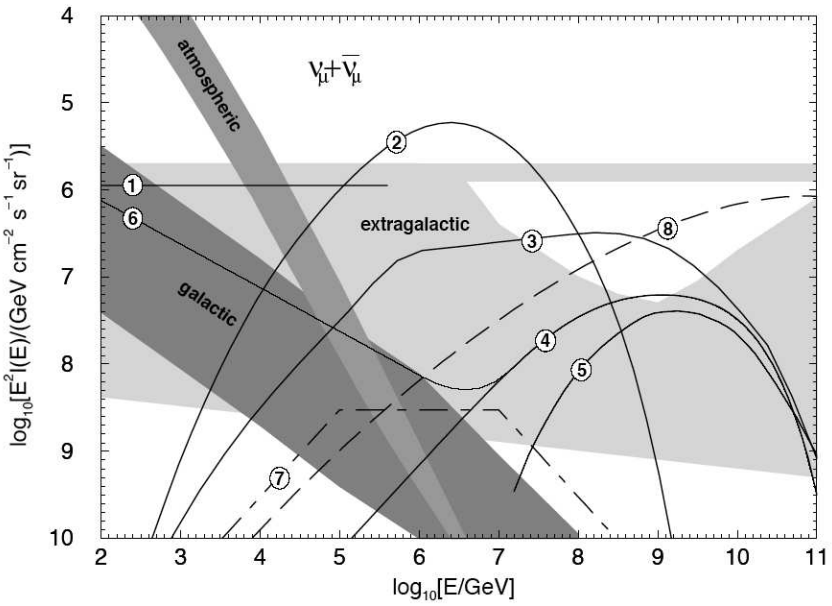

Figure 1.8: Neutrino Flux Predictions (I). (1-4 and 6) AGN models; (5) GZK; (7) GRB; (8) topological defects. The shaded regions labeled as "atmospheric" and "galactic" identify the theoretical bounds on background events from Earth atmosphere and Galactic disc; "extragalactic" indicates a diffuse flux from non-resolved extra-galactic sources. Plot is taken from [46], details therein.

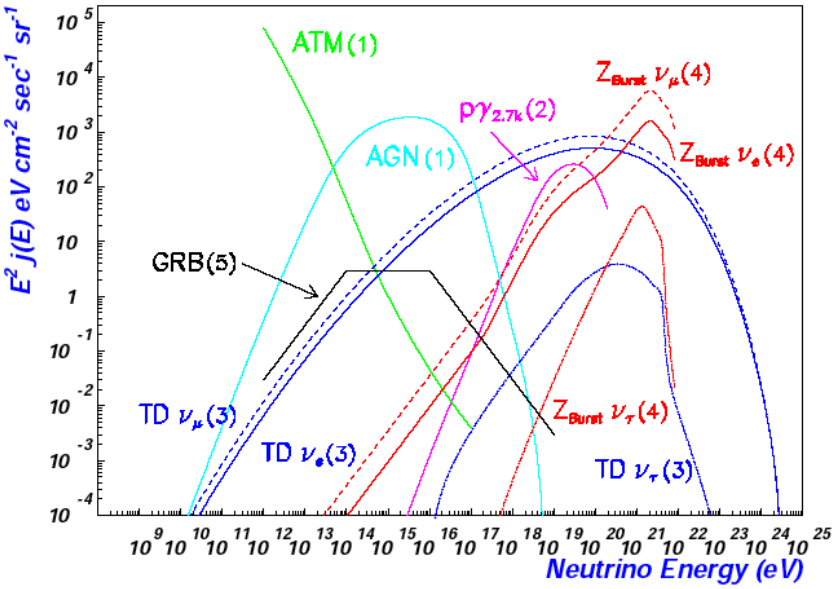

Figure 1.9: Neutrino Flux Predictions (II). The plot is taken from [81]; numbers identify the references for each computation presented. Extragalactic sources and processes listed in Table 1.2 are present. $p\gamma_{2.7\,K}$ indicates the GZK neutrinos."ATM" refers to atmospheric neutrinos.

In addition, placing a neutrino telescope in the abyss (or deep in ice) provides a screen against background events. Considering, in fact, the case of the optical technique, the goal is to detect the muon track resulting from neutrino-induced muon passage in water. The background is given by atmospheric muons, produced as secondary particles in cosmic ray interactions in Earth atmosphere, and mimicking a neutrino-induced event. The water mass above the detector stops a large amount of atmospheric muons, preventing them to reach the sensitive volume.

Therefore, in the sense discussed in this section, a natural target as the oceanic mass plays a triple action: it is, at the same time, the target for neutrino interaction, the medium for signal transmission and the screen for background events reduction.

1.3.1 Neutrino Physics and Neutrino Interactions

In the framework of the Standard Model, neutrinos weakly interact with nucleons by deep inelastic scattering, through charged current (CC) and neutral current (NC) processes:

$$\nu_\ell(\bar{\nu}_\ell) + N \rightarrow \ell^-(\ell^+) + X \tag{1.2}$$

$$\nu_\ell(\bar{\nu}_\ell) + N \rightarrow \nu_\ell(\bar{\nu}_\ell) + X \tag{1.3}$$

with ℓ indicating the leptonic flavour ($\ell = e, \mu, \tau$), N the target nucleon, X the hadronic cascade originating in the interaction. The bar refers to anti-neutrinos. Almost 80% of the initial neutrino energy stays in the leptonic channel [82]. Figure 1.10 displays cross-sections for νN interactions at high energies.

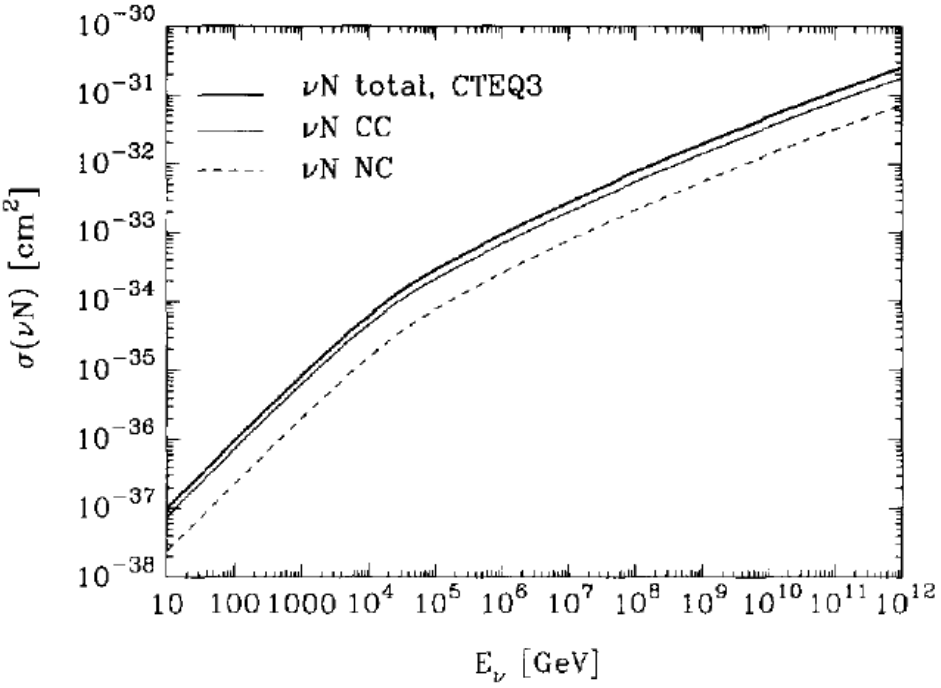

Figure 1.10: Neutrino-nucleon cross section at high energies. Cross section increases with energy [82].

For what concerns charged current interactions (Equation 1.2), both the charged lepton and the hadronic shower leave a signature in the detector. If there is a muon in the final state, the expected signature is a long track. Showers, both hadronic and elecro-magnetic, are expected as a signature of electrons and tau leptons[10]. Cherenkov neutrino telescopes are mainly tuned to detect muon tracks in the apparatus, as it will be presented in Section 1.3.2. The hadronic component (and the cascading component in general) may be accessible through acoustic detection.

Considering neutral current interactions (Equation 1.3), the neutrino in the final state escapes unperturbed from the instrumented volume, and cannot be detected. The only detectable product is the hadronic shower, that is what the acoustic technique aims to identify.

1.3.2 Optical Cherenkov Telescopes - toward the km3

The optical Cherenkov telescopes constitute the present-generation detectors for high-energy neutrinos in ice and water. Cherenkov neutrino telescopes look for muons produced in charged current neutrino interactions (Equation 1.2).

Entering the details, the secondary muon is an ultra-relativistic particle travelling in a medium (water or ice) in which the refractive index n is larger than 1, so that the light speed in the medium $c = c_0/n$ (c_0 is light speed in vacuum) is smaller than particle speed. The consequence is coherent emission of Cherenkov[11] light, due to polarization and de-excitation of atoms in the medium. The geometry of the emission is fixed by the refractive index. The wavefront is a cone surface, whose axis is coincident with the particle track, and whose aperture is definite. Figure 1.11 sketches the phenomenon of Cherenkov radiation emission, focusing on the Cherenkov angle $cos\phi = \frac{1}{n\beta}$, with $\beta = v_\mu/c$ defining the speed of the ultra-relativistic particle. In case of high energy cosmic neutrinos inducing ultra-relativistic muons in water, $n \simeq 1.35$, $\beta \sim 1$ and thus $\phi \sim 41°$.

The consequence of the predictable geometry of the Cherenkov emission is that a particle track with a definite direction of propagation manifests with a unique signature on a detector made up as a regular grid of light collectors, or photo-multipliers tube (PMTs). The particle track direction can be reconstructed comparing time of arrivals of photons to the PMTs. Data analysis consist in selecting hits on photo-tubes, in order to identify the Cherenkov cone, and thus the corresponding muon track that has induced it. Once that the muon track direction has be identified, pointing properties of the telescope are assured by the fact that in relativistic neutrino interactions, the muon direction is almost collinear to the primary neutrino ($\theta_{\nu-\mu} \sim 1.5°/\sqrt{E_\nu[TeV]}$ [85]), and therefore to the astrophysical source.

The first proposal to employ the Cherenkov technique for neutrino detection in submarine environment dates back to the '60s, by Markov and Zheleznykh [86]. An artist view of a sub-marine Cherenkov array is in Figure 1.12.

[10] Tau leptons can be distinguished from electrons because of tau typical signatures, as a consequence of tau decay. More on this (the so-called "double-bang" events) can be checked in [83]. Additional details on different lepton signatures in optical neutrino telescopes are accounted in the IceCube Preliminary Design Document (PDD) [84].

[11] The process takes its name after the Russian scientist P.A. Cherenkov, who first described it. He was awarded the Nobel Prize in Physics in 1958, "for the discovery and the interpretation of the Cherenkov effect" (`http://nobelprize.org`).

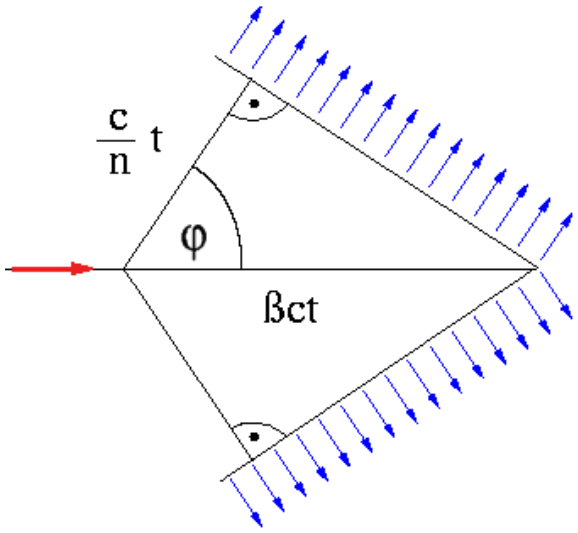

Figure 1.11: Geometry of the Cherenkov radiation emission. The Cherenkov angle is in evidence. Image from Wikimedia Commons.

In the following, I will give a quick review on existing Cherenkov neutrino telescopes, with a list of references.

The precursor of underwater neutrino experiments is the **DUMAND** project - Deep Underwater Muon and Neutrino Detector [88] - operating from 1976 to 1995. The goal of the project was to install a neutrino detector in the Pacific Ocean. The efforts were mainly focused on the optical Cherenkov technique, carrying on both theoretical and experimental studies, but the DUMAND project has been also where the first investigations on the feasibility of the acoustic detection were developed, in order to test the efficiency of the technique for neutrinos in submarine environment. The DUMAND experiment never saw the light of the day, because of lack of funding, but still the activities carried on inside DUMAND constitute a rich repository of information for people in the field, and have been used as a reference by the next experiments.

The first concrete realization of a Cherenkov telescope is **Baikal** [89], a Russian experiment located in the Lake Baikal, in Siberia. The project started in the '80s, but the first full prototype was completed in the '90s and, with several stages of improvements, it has turned up to the current status (NT200+) since 2005. Together with the development of the optical Cherenkov technique, feasibility studies on acoustic neutrino detection are ongoing. For additional details are available in the latest status report of the Baikal experiment [90].

In the mean time, two other location started to catch the scientists attention for the deployment of a neutrino telescope: the Mediterranean Sea and the Antarctica.

Concerning the South Pole, **AMANDA** - Antarctic Muon And Neutrino Detector Array [91] - is the first neutrino telescope to exploit antarctic ice for Cherenkov detection of cosmic neutrinos. In AMANDA, holes have been drilled in ice, and PMTs are deployed inside. See [92] for details on the AMANDA experiment and a summary on AMANDA results.

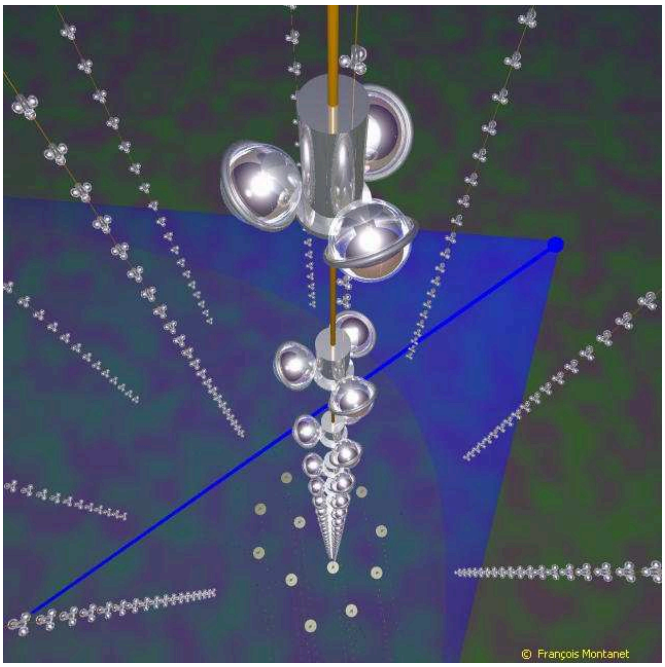

Figure 1.12: An artist view of a submarine neutrino Cherenkov telescope (ANTARES). Optical modules are photo-multipliers tubes, hosted in glass spheres. A cluster of three spheres constitutes a "floor", hanging to a "string", the linear structure anchored to the sea bottom. The ANTARES telescope is made up of 12 strings, each one with 25 floors. To complete the picture, a muon track passing through the apparatus is added, with its Cherenkov cone. Image from the ANTARES experiment web site [87].

AMANDA extension, **IceCube**, is presently under-construction, with the goal to have one cubic kilometer instrumented volume in the South Pole. A detailed report on the IceCube activities can be checked at the full-documented web-page [93] and the latest facts concerning the experiment are in 2008 IceCube update [94].

IceCube will complement its predecessor AMANDA not only increasing the instrumented volume for neutrino Cherenkov detector, but also developing auxiliary detectors, like the IceTop air shower array experiment [95], and exploiting the acoustic and radio techniques. For this purpose, several R&D activities are ongoing in the IceCube site, some details on radio and acoustic projects in ice will be given in the next section and in Section 2.4. The plan, as it will be discussed in Section 1.3.3, is to work for a hybrid detector, where several different detection techniques are put together, in order to join efforts and win the challenge of neutrino astronomy.

In the Mediterranean Sea, three European projects are working at the development of a submarine neutrino observatory. The first one to appear is **NESTOR** [96], in Greece. Recent updates on the NESTOR activities are reported in [97], mainly devoted to developments of technologies and infrastructures for the marine environment.

ANTARES - Astronomy with a Neutrino Telescope and Abyss environmental RESearch [87] - is the first full prototype neutrino Cherenkov telescope operating in the Mediterranean Sea. The detector, located offshore Toulon, France, has been completed in June 2008, data taking and analysis is currently on-going and results are

forthcoming. The ANTARES achievements constitute a fundamental step toward a cubic kilometer detector in the Mediterranean Sea, for what concerns both technical solutions and data analysis. Acoustic activities in ANTARES are also present, some references will be given in Section 2.4.

The activity of the **NEMO** Collaboration - NEutrino Mediterranean Observatory [98] - started with multi-disciplinary investigations of the submarine environment. In several sea-campaign, in collaboration with oceanographers, geophysicists, oceanographers, extensive studies have been carried on concerning geological (orography of the sea bottom), oceanographic (sea currents), biological (fishes, bacteria, bio-fouling), physical (temperature and salinity profile; natural radioactivity of sea water) and optical (light attenuation length [99]) properties of the abyss, in order to complete site selection activity, that is performing accurate measurement to identify the optimal submarine location for the deployment of a Cherenkov neutrino detector.

In parallel with the study of the deep-sea environment, the NEMO Collaboration has developed technological solution (mechanics and electronics) for the project of an underwater neutrino telescope. NEMO "phase-I" is the test of instrumentation devices, mechanical structures and electronics of data transmission in the test-site, offshore Catania, Sicily (Italy). The activity was carried on with the deployment of the "mini-tower", a scaled prototype of the NEMO project design solution.

The Catania test-site hosted also the OνDe station - Ocean Noise Detection Experiment, for the real-time monitoring of the acoustic background. More on this in Section 2.4.

The NEMO experiment is now entering its "phase-II", consisting in the deployment of a full scale structure (the NEMO "tower") offshore Capo Passero, Sicily, in the submarine site that has been selected by the Collaboration (3500 m depth). NEMO phase-II will include hydrophones, for a first operative approach to acoustic neutrino detection (see Section 2.4).

The next step for what concerns the European projects is to converge, and upgrade toward a "km^3" - cubic kilometer detector. The progress up to the "km^3" is the mandatory solution for getting significant results in neutrino astronomy and astrophysics. The three European collaboration, NESTOR, ANTARES and NEMO enter as "pilot projects" the European **km3Net Consortium** [100], joining advancements in research and development. The goal is to connect people working in the field of high-energy neutrino telescopes, so that they could share experiences and cooperate, in order to carry on a unique project for a cubic kilometer detector in the Mediterranean Sea [101]. Indeed, a northern hemisphere neutrino observatory is a desideratum, to complement IceCube observations and get a full-view of the sky-map, as it is shown in Figure 1.13[12].

[12]Because of the tiny neutrino-nucleon cross section (Figure 1.10), the probability that a high-energy neutrino in the energy range $1 - 10TeV - 1 - 10PeV$, accessible to Cherenkov telescopes, would interact in the detector volume is not negligible only if it enters the detector from below (up-going event), after having crossed the full Earth mass. To make things simpler, we can say that down-going muon tracks are background (atmospheric muons), while up-going muon tracks are signal candidates (to be distinguished from background atmospheric up-going neutrino events, that mimic astrophysical signature). Therefore, Cherenkov telescopes mainly look downward, having approximately a 2π sensitivity: PMTs are downward oriented and selection and reconstruction strategies in data analysis are implemented to keep up-going track and to reject down-going tracks.

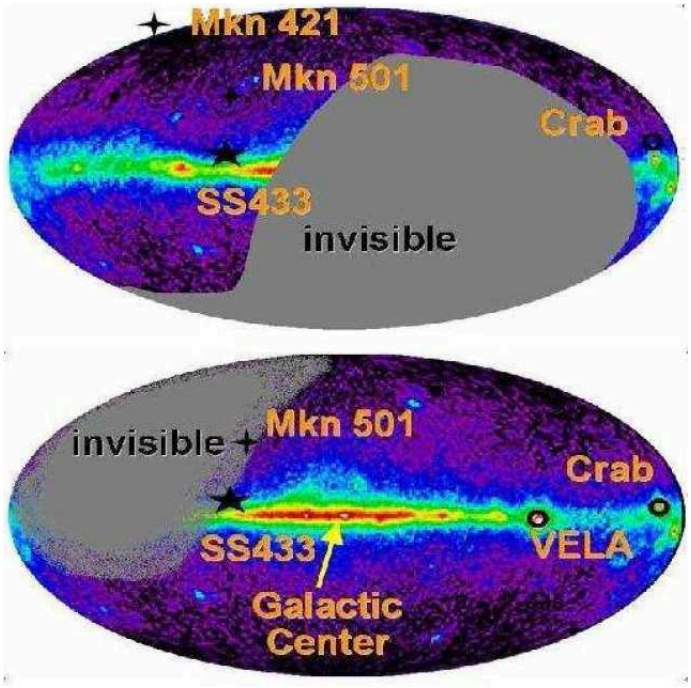

Figure 1.13: Field of view of a neutrino telescope at the South Pole (top panel) and in the Mediterranean Sea (bottom panel), in galactic coordinates. A 2π downward sensitivity is assumed, having as a consequence invisible regions in the sky. Some candidate neutrino sources are indicated in the map. It is clear that, on the contrary of the South Pole telescope, a Mediterranean observatory would have access to the Galactic center, that is a very promising object of investigation [101].

The multi-disciplinary activities of the km3Net Consortium are organized in working packages, covering all the main features in the design study of a neutrino submarine telescope: physics analysis and simulation, to investigate the performance of different detector options; shore, sea-surface and deep-sea infrastructure, to carry one site-selection activity, and to develop deployment and recovery procedures; design of the optical modules; design of the readout and data acquisition system; interactions with associated sciences, as biology, geology, oceanography. The enumerated activities are in the list of items presented and discussed at the VLVnT Conferences - Very Large Volume Neutrino Telescope. Conference proceedings provide additional information on the topic and document the joint efforts carried on towards a km^3 detector [102] [103] [104].

1.3.3 Radio and Acoustic Detection - beyond the km3

An additional step further, beyond the km^3, is provided by the so-called alternative techniques (radio and acoustic detection), in order to complement and extend neutrino telescopes, and increase detector capabilities up to energies of the order of the GZK events ($\sim 10^{17-18}$ eV) and above [105] [106]. Indeed, the neutrino flux in this energy range is predicted so low, that a kilometer cube detector would be not enough to intercept the occurrence of an event, and therefore a larger instrumented volume should be designed.

The Cherenkov technique is not adequate for such an extension, because the deployment of mechanical structures with optical modules (PMTs), over a volume larger than a cubic kilometer, would imply not affordable costs and not likely to overcome technical constraints, since the km3 already represents the boundary, for what concerns economical and technological resources. Distances between photo-tubes, in fact, are determined by the value of the effective attenuation length of light (between 20 and 50 m, considering ice and ocean water [46]): a larger spacing would cause a loss of time coincidences between hits on PMTs, and would degrade or preclude the reconstruction of the Cherenkov cone.

Therefore, the key point to progress beyond the km^3 is considering the propagation of signals in water and ice, and sound and radio signals share the appealing property to have a large attenuation length: under certain conditions, the range is of the order of the kilometer, for both radio and acoustic pulses. Different from the case of optical modules in a Cherenkov grid, the consequence is that acoustic and radio modules can be positioned with much more spacing between adjacent elements, offering thus the opportunity to have a very large instrumented volume with a reduced number of sensors, with sensible saving of costs and resources.

Therefore, the implementation of radio and acoustic solutions for neutrino detection represents the future of high-energy neutrino telescopes, and this is why experiments and collaborations in the field are carrying on investigations on the topic, as listed in the previous section.

The **ARENA Workshops** (Acoustic and Radio EeV Neutrino Activities) are expressly dedicated to the development of radio and acoustic techniques, and to their application for neutrino detection. The proceedings of the conferences are a valid tool to get an update on the progresses of the techniques and on the status of the several projects ongoing in the field [107] [108] [109].

The conclusive goal of all these studies is the prospect for a **hybrid detector** (optical-acoustic in water, or optical-radio-acoustic in Antarctic ice, simulation is ongoing, Figure 1.14). The techniques should overlap in the energy range below 10^{18} eV, as illustrated in Figure 1.15, meeting the requirements for a cross-calibration of the telescope[13].

In addiction, these future composite infrastructures may be complemented with auxiliary apparatuses (for instance, IceTop) and external collaborations (coincidences with gravitational wave observatory events, gamma-ray burst alerts and satellite triggered acquisition), to cross-calibrate the detector and increase the opportunity of event detection.

1.3.3.1 Radio Detection

The pioneer of the radio technique proposal was Askaryan, in the '60s, with the discovery of what is now known as "Askaryan effect" [114] [115]. It consists in coherent emission of Cherenkov radiation in the radio band from electro-magnetic showers propagating in dielectric media, as a consequence of the occurrence of a net negative charge excess [116].

[13] A remark: the opportunity of overlap and cross-calibration in hybrid detectors is already exploited in the Pierre Auger Observatory (surface detector and fluoresce technique) [110].

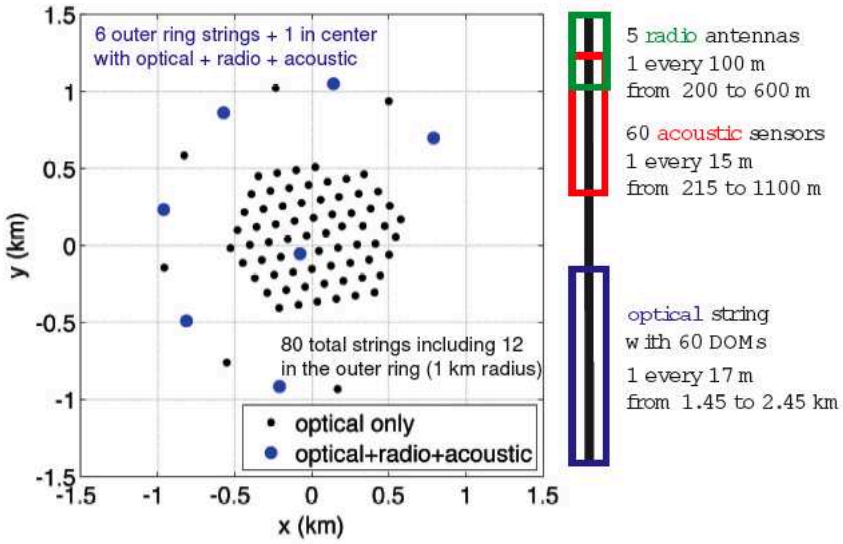

Figure 1.14: A project for an hybrid detector (optical-radio-acoustic) in the South Pole. The simulated performances of a so-equipped apparatus are explored in [111]. See also [112].

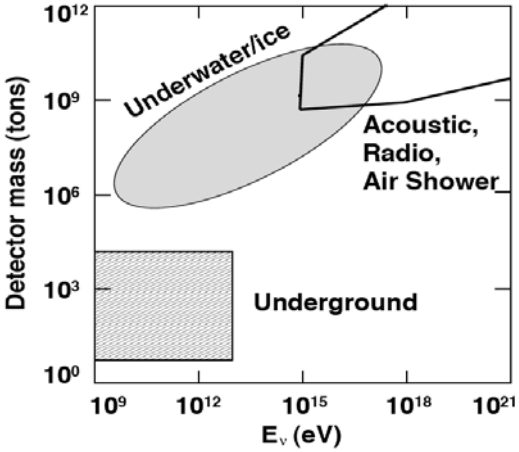

Figure 1.15: Detector masses for different energy range and neutrino detection techniques. 10^9 tons is about the mass contained in a cubic kilometer detector in water; 10^{12} tons is the mass of water in a cube of approximately 10 km per side. Underwater/ice area identifies the energy range accessible with optical Cherenkov telescopes. The overlap between optical and radio/acoustic technique is in evidence. The label "air shower" refers to the opportunity, available in Auger Observatory, to look for neutrino-induced horizontal air showers at ultra-high energies [113].

Radio technique can be applied to ultra-high-energy neutrinos, since the emitted radiation can reveal electro-magnetic showers produced in charged current neutrino interactions (Equation 1.2)[14]. The Askaryan effect is expected to have measurable signatures in ice, salt and sand; it has been verified with laboratory tests [118] [119].

[14]In addition, several projects are operating to measure Cherenkov coherent radio emission from extensive cosmic ray showers in atmosphere, complementing observations of surface array detectors (KASCADE [117], Pierre Auger). More on this in the proceedings of ARENA Workshops.

In the following, I will report on the status of some of the projects involved in radio detection of ultra-high-energy neutrinos. Additional information is available in the Conference Proceedings of the ARENA Workshops.

The main field of action is Antarctic ice, where a lot of work is ongoing concerning signal simulation, expected detector performances, development of technological solutions. An important role is played by *in situ* measurements of ice properties, to better understand the effect of environmental parameters on signal production and propagation. Most of the activity carried on at the South Pole consists in IceCube related projects and experiments.

The **RICE** experiment (Radio Ice Cherenkov Experiment) is an array of antennas deployed in ice. Five years of data taking allowed the RICE experiment to set upper bound on the diffuse ultra-high energy neutrino flux [120]. The successor of RICE is **AURA** - Askaryan Under-ice Radio Array, currently under construction and operates inside the IceCube Collaboration [121].

A different concept is considered in the **ANITA** experiment - ANtarctic Impulsive Transient Antenna, a balloon born apparatus, flying over the Antarctica at about 35 km height, and able, in this way, to inspect up to $1.5 \cdot 10^6\, km^2$ of ice surface. A prototype instrument, ANITA-lite, has already been launched, in 2004, and has been operative for about 18 days. ANITA-lite experiment was successful, for what concerns both technological solutions and data taking. Data collected with ANITA-lite test flight allowed the collaboration to put limits on cosmic neutrino flux detectable with the radio technique (Figure 1.16) [122]. A second flight with a larger apparatus has been completed in 2006-2007. Data analysis is in progress, preliminary results suggest an agreement with the projected sensitivity in Figure 1.16. Improvements to the detector are ongoing, additional data taking is foreseen.

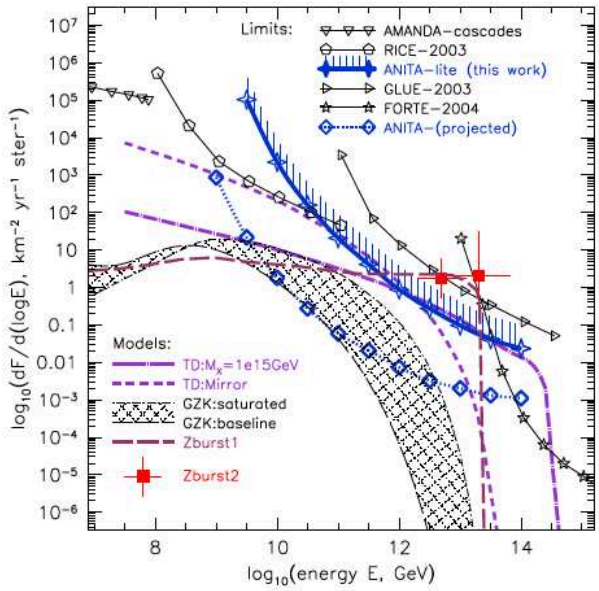

Figure 1.16: Limits on ultra-high-energy neutrino flux. Results from ANITA-lite data analysis are compared with constraints computed by other experiments, and with some theoretical models. In addition, the plot reports the projected sensitivity for the full ANITA experiment. Details in [122].

The **FORTE** satellite - Fast On-orbit Recording of Transient Events - observed the Greenland ice for about 2 years (about 3 days of net exposure), searching for coherent Cherenkov emission from electromagnetic showers, as signature of neutrino interactions [123]. FORTE results enabled to put a limit on ultra-high-energy neutrino fluxes, reproduced in Figure 1.16.

A separate group of projects concerns the opportunity to search for signatures of neutrino interactions in the lunar regolith, that is the layer of sand and dust covering the Moon surface. Results of the **GLUE** experiment - Goldstone Lunar Ultra-high energy neutrino Experiment - have been obtained with 120 hours of livetime with two radio antennas at the Goldstone radio observatory [124]. The GLUE limit is shown in Figure 1.16. More on lunar Cherenkov neutrino detection, including an historical overview on past experience and a report on future projects, is in [125].

A review on the principles of acoustic technique, and on the status of neutrino acoustic detection is accounted in Chapter 2.

Chapter 2

Acoustic Detection

2.1 The Thermo-Acoustic Model and Acoustic Neutrino Detection

A proposal on acoustic detection of particles and on the opportunity to apply the technique to the neutrino case was advanced by Askaryan [126] [127]. The idea is based on the thermo-acoustic (or hydrodynamic) mechanism of energy dissipation, according to which particle energy losses in matter induce a local heating, that perturbs the thermal equilibrium of the medium and propagates as a pressure wave.

The concept can be applied to high energy neutrino detection, considering particle cascades resulting from neutrino interactions with nucleons (Section 1.3.1). As a consequence of neutrino interaction, neutrino energy is transferred to particles in the shower and, as the shower develops in matter (at about the speed of light), energy is almost instantaneously deposited along the shower axis, producing a fast local heating of the medium and a density variation. The perturbation manifests as a bipolar pressure pulse (compression - thermal expansion - followed by rarefaction), propagating in the medium at the speed of sound.

The volume interested by the propagation of the particle cascade is where energy deposition occurs (perturbed region) and constitute the acoustic source generating the pressure wave. Considering neutrino interaction in water, and assuming energy deposition occurring over a cylinder with longitudinal extension $L \sim 10\,m$ and radial extension $r \sim 10\,cm$ (order of magnitudes of the shower development in water), the characteristic time of the hydrodynamic mechanism can be estimated as $\tau_{hydro} \sim r/v \sim 10^{-4}\,s$ ($v \sim 1500\,m/s$ is the sound speed)[1]. Since particles in the shower propagate at about the speed of light $c \simeq 3 \cdot 10^8\,m/s$ (ultra-relativistic particles), the characteristic time of energy deposition is about $\tau_{dep} \sim L/c \sim 10^{-7}\,s$, that is much smaller than τ_{dep}, having as a consequence that energy deposition in the shower volume can be approximated as instantaneous. This hypothesis introduces a simplification in the analytical formulation of the pressure wave propagation (Section 2.2).

[1]For what concerns characteristic time, the thermo-acoustic mechanism is the most efficient process of energy (heat) dissipation.For comparison, considering processes due to kinematic viscosity $\eta \sim 10^{-6}\,m^2/s$, characteristic time is of the order of $\tau_\eta \sim r^2/\eta \sim 10^4\,s$.

In principle, both hadronic and electromagnetic cascades are detectable by the acoustic technique, since in both cases neutrino interaction result in a local energy deposition fulfilling the conditions of the thermo-acoustic model. Nevertheless, in practice, the so-called **LPM effect** has to be take into account. The LPM effect was originally discussed by Landau, Pomeranchuk and Migdal [128] [129] [130]. It is a suppression process reducing the *bremsstrahlung* and pair production cross section, for high-energy electrons and photons, respectively. As a consequence, considering a cascade of high-energy particles, modifications are introduced in the shower development: the electro-magnetic part of the shower elongates, and the energy density along the particle tracks decreases. The consequences of the LPM effect on acoustic detection are straightforward, since pressure pulse amplitude depends on energy density (and not on energy itself). In addition, the LPM effect introduces large fluctuations for what concerns the longitudinal profile of the particle cascade [131]. This causes uncertainties in the modeling of the shower development, that is in the description of the acoustic source.

LPM threshold is the energy at which the LPM effect starts to be significant; it depends on the medium density, order of magnitude for water is $E_{LPM} \sim 10^2\, TeV$ [132]. In short, the LPM effect alters the shower propagation, and it is much more significant as the energy of the primary neutrino increases.

To keep apart complications due to the LPM effect, only the hadronic component of cascades will be investigated when considering expected signals from neutrino-nucleon interactions in water. The study will be limited to the case of acoustic pulses from neutrino-induced hadronic showers, as it will be discussed in Chapter 4.

Acoustic pulses in water are registered by means of hydrophones (by analogy, devices employed in-ice are named "glaciophones"). Typically, the sensitive element is made up of piezo-electric ceramics, materials responding with electric polarization to mechanical solicitations. The design of acoustic modules, and the calibration of sensors, constitute an important part of the activity carried on by groups working in the field of acoustic neutrino detection. Indeed, acoustic sensor technology is on the shelf (commercial hydrophones), but several different prototype are under study, especially for what concerns the the power consumption and the sensitivity at large pressure (large depth in water and ice), in the frequency band where neutrino-induced signals are expected.

2.2 The Wave Equation

Following the account given by Askaryan in [133], a quantitative approach to the thermo-acoustic mechanism in water leads to the non-homogeneous **Wave Equation** (second-order linear partial differential equation in the unknown pressure):

$$\nabla^2 p(\vec{r},t) - \frac{1}{v^2}\frac{\partial^2 p(\vec{r},t)}{\partial\, t^2} = -\frac{\beta}{C_p}\frac{\partial^2 q(\vec{r},t)}{\partial\, t^2} \tag{2.1}$$

where v is sound speed, β is thermal expansion coefficient, C_p is specific heat coefficient, $p(\vec{r},t)$ is the pressure signal, $q(\vec{r},t)$ is the energy deposition density (source term), defining the boundary condition of the problem.

The general solution of the Wave Equation is the **Kirchoff integral**:

$$p(\vec{r},t) = \frac{\beta}{4\pi C_p} \int \frac{1}{|\vec{r}-\vec{r}'|} \frac{\partial^2}{\partial\, t^2}\, q\left(\vec{r}', t - \frac{|\vec{r}-\vec{r}'|}{v}\right) dV' \tag{2.2}$$

handling the propagation according to the Green formula (retarded potential).

Under the hypothesis of instantaneous energy deposition, the source term $q(\vec{r},t)$ can be expressed so that $\dot{q}(\vec{r},t) = q(\vec{r})\delta(t)$, assuming $t = 0$ as the time of occurrence of neutrino interaction, that is coincident with the time when the acoustic source pops up. In other words, the acoustic source does not evolve in time, and time evolution (time derivative) is simply propagation at the speed of sound, taking into account the relation between time and distance $R = v \cdot t$. The Kirchoff three-dimensional integral thus reduces to a surface integral (**Poisson formula**):

$$p(\vec{r},t) = \frac{1}{4\pi} \frac{\beta \cdot v^2}{C_p} \frac{\partial}{\partial\, R} \int_{S_{\vec{r},R}} \frac{q(\vec{r}')}{R}\, d\sigma' \tag{2.3}$$

Integral is computed over spherical surfaces (S), with radius R and center at the hydrophone position $\vec{r}$.

$\Gamma = \frac{\beta \cdot v^2}{C_p}$ is the **Gruneisen coefficient**; it expresses a measurement of the efficiency of the thermo-acoustic mechanism, in a sense that it evaluates how much of the deposited energy is transferred via the propagation of a pressure wave. The Gruneisen coefficient is related to environmental parameters, and to thermal expansion coefficient in particular, because the generation of the acoustic perturbation strongly depends on heat conversion into thermal expansion.

As in evidence in the Poisson formula, the Gruneisen coefficient determines the amplitude of the resulting acoustic pulse, and therefore it specifies an indication about measurable pressure signals in a definite environment. In other words, the Gruneisen coefficient can be considered as a parameter to quantify the performances of the acoustic technique in a specific site. Considering acoustic waves in water, the Gruneisen coefficient increase with water temperature (Section 3.4.3), and therefore warm waters are to be preferred. This corresponds to an opportunity in favor of the Mediterranean Sea, whose temperature is higher than values registered in the oceans.

Considering a neutrino-induced shower as an emitting line (cylindrical acoustic source), each portion of the perturbed volume, that is each segment along the shower track, can be considered as a point-like source, emitting sound. The several source element do not combine constructively everywhere, and the so-called **acoustic pancake** represents the interference figure characterizing the acoustic pulse propagation from an emitting line [134]. The acoustic "pancake" generation is illustrated in Figure 2.1. As a consequence of the acoustic pancake, amplitude and shape of the resulting pulse strongly depend on the hydrophone position, that is where the receiver is located with respect to the acoustic source. This is a key-point for what concern signal identification in the sub-marine environment, in particular when modeling a matched filter to select the signal from the background. Investigations on this topic are carried on in Section 4.3.

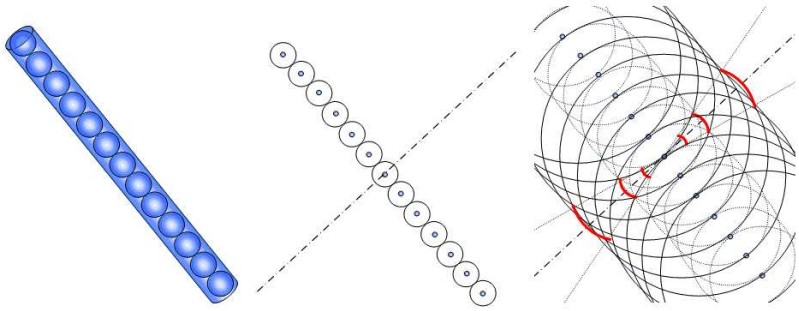

Figure 2.1: Acoustic "Pancake". Each element along the shower track behaves as a point-like source. Constructive interference (between the Huygen's wavelets) defines a "pancake" perpendicular to the original neutrino direction. The typical opening angle is about 5 degrees. This schematic description is more appropriate under the assumption of instantaneous energy deposition. Picture by the ACoRNe Collaboration [135].

2.3 Sound in Water: Acoustic Pulse Propagation

Moving apart from the analytical assumptions of the Askaryan model to the concrete case of experimental techniques to detect acoustic signals from particles in the sub-marine environment, things become difficult, since sound propagation is "spoiled" by the fact that sea water is not an ideal fluid, but characterized by absorption and scattering phenomena.

Absorption is connected with losses due to shear viscosity mechanisms. *Scattering* is caused by sea water inhomogeneities, such as bubbles, plankton, particulate matter. The combined effect of scattering and absorption defines *sound attenuation*. A quantitative measurement of attenuation comes from the *attenuation coefficient* α, that is a function of frequency f and of environmental parameters. α is typically expressed in [dB/km], representing how much the sound signal reduces, with respect to the initial value, for increasing distances from the generation point.

Several parametrization have been proposed to account the effect of environmental parameters on attenuation coefficient [136] [137]. See also the *Encyclopedia of Acoustics* [138], for an introduction on underwater sound, essential oceanography and an account on sound propagation.

A very approximated description can be given considering Figure 2.2, that reproduces attenuation coefficient α in [dB/km] versus frequency. Considering the reported values, we can describe the dependence of attenuation with frequency according to the very simplified model:

$$\alpha[dB/km] \propto f^2 \tag{2.4}$$

with a coefficient of proportionality of the order of 10^{-9} (the coefficient of proportionality can be assumed approximately constant in the frequency range of interest ($f = 10 - 100kHz$), taking into account the stability of water properties at large depths).

The formula above assures that, for frequencies in the range of some tens of kHz, acoustic pulses attenuate of a few dB after a propagation of the order of the kilometer (attenuation length, that is $1/\alpha$ is about 1 km at frequency f=20 kHz, as anticipated in Section 1.3.3).

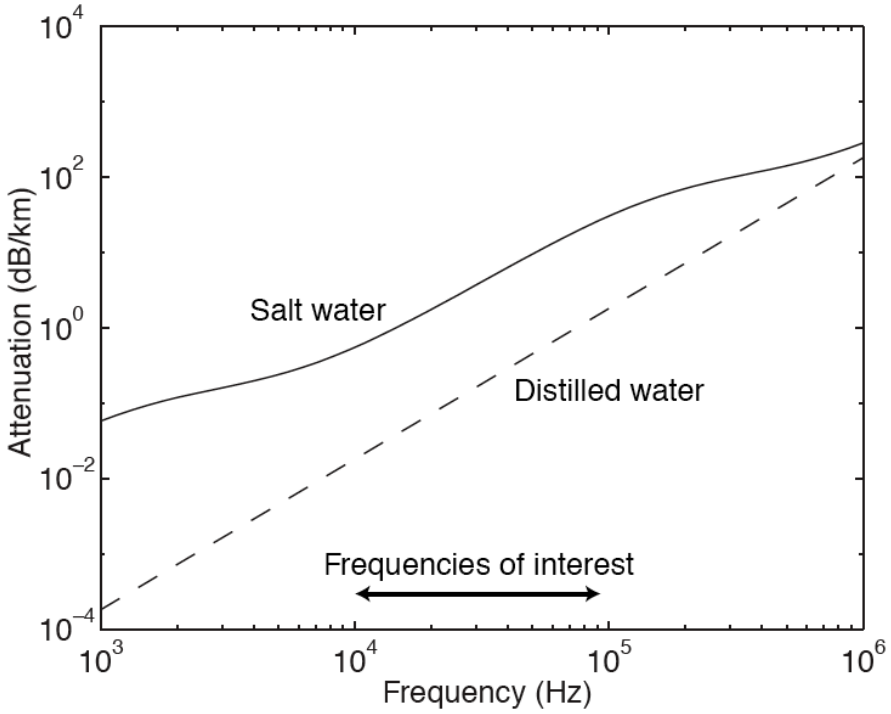

Figure 2.2: Attenuation coefficient, from [134]). The label "frequencies of interest" identifies the range in the frequency band where neutrino-induced acoustic pulses are expected.

The effect of attenuation can be introduced in the computation at different levels of accuracy. Learned's solution [139] consists in introducing the viscosity in the model through the Stokes formulation of the fluid equation of state. With such assumptions, d'Alembert wave equation 2.1 thus becomes:

$$\nabla^2 \left(p(\vec{r},t) - \frac{1}{\omega_0}\frac{\partial p}{\partial t} \right) - \frac{1}{v^2}\frac{\partial^2 p(\vec{r},t)}{\partial\, t^2} = -\frac{\beta}{C_p}\frac{\partial^2 q(\vec{r},t)}{\partial\, t^2} \tag{2.5}$$

with $\omega_0 \approx 10^{12} s^{-1}$ the characteristic attenuation frequency.

The solution of the wave equation is computed in the frequency domain through Fourier transform. The result can be expressed as a convolution with a *smearing function*, that accounts for attenuation effects, and results in a "gentle" power-law cut-off at large distances.

Askaryan's approach in [133] is pretty similar, with the important difference that the "smearing function" does not come from the solution in the frequency domain of the wave equation with losses, but it is selected assuming an exponential cut-off model. Askaryan results obtained including or neglecting the attenuation term in the computation show an agreement within 20-30%.

An exponential cut-off in the frequency domain is the solution adopted also by the ACoRNe Collaboration [140]:

$$A(\omega) = e^{-\alpha(\omega)\cdot R} \tag{2.6}$$

with R distance from the shower axis, $\alpha(\omega)$ the attenuation coefficient as a function of frequency. Computation with the ACoRNe strategy provides the same outcome of the Learned's approach, but it is much more faster.

It is important to underline that the solution of the wave equation given by the Poisson formula (Equation 2.3) does not consider the frequency dependence explicitly, therefore it does not take into account sound attenuation. Since the AcPulse code (Section 3.4.2) used to compute pressure pulses in the simulation is based on the Poisson formula, attenuation is not included in the simulations discussed in this work.

An additional remark should be added concerning the hydrophone transfer function. The spectral content of collected signals, in fact, is altered non only by sound propagation (transfer function of the medium), but also by the frequency response of the transducer. In this framework one can place the importance of hydrophone calibration procedures, in order to get an accurate model of acoustic sensors used for data taking.

2.4 Listening to Neutrinos - a Review on Acoustic Detection Activities

In the following, I will give a short report on some of the activities ongoing in the field of acoustic detection, including references. Additional information and details can be found in the Conference Proceedings of ARENA Workshops. As anticipated in Section 1.3.2, most of the projects are related to Cherenkov neutrino telescopes, and are developed to explore the feasibility of the acoustic detection, and the opportunity of integration of acoustic devices into optical detectors.

Starting from in-ice experiments, the IceCube activity in the field of acoustic detection is **SPATS** - South Pole Acoustic Test Setup [141]. SPATS has carried on several studies on the design of acoustic devices suitable for the South Pole environment. Piezo-electric acoustic sensors have been deployed in ice, and the development of technological solution is ongoing. In addition, SPATS data taking allows investigations on environment parameters and ambient acoustic noise.

The **SAUND** experiment - Study of Acoustic Ultra-high energy Neutrino Detection - employs an existing large hydrophone array infrastructure in the US Navy Atlantic Undersea Test and Evaluation Center (AUTEC), located nearby Bahama islands, in the Atlantic Ocean. SAUND-I (first phase of operation and data taking) has been an important test-bench for neutrino acoustic detection, in particular considering data acquisition and data analysis. Data collected using a sub-set of 7 hydrophones allowed to set the first experimental upper limit for the flux of ultra-high-energy neutrinos with acoustic technique (Figure 2.3) [142]. Since 2005 SAUND has upgraded to phase II, consisting in the opportunity to employ a larger number of hydrophone in the AUTEC array. First results of SAUND-II concerns ambient noise monitoring [143].

A similar experience is that one of the **ACoRNe** Collaboration - Acoustic COsmic Ray Neutrino Experiment [135]. The group, operating in the United Kingdom, has the opportunity to employ the existing military array in Rona, north of Scotland, as a test-bench for hydrophone calibrations and data analysis. At the same time, the group is carrying on extensive simulations of neutrino interactions and neutrino-induced acoustic pulses in sea water. Their work constitutes the starting point for my studies on the simulation of acoustic pulses in the neutrino-case (Chapter 4).

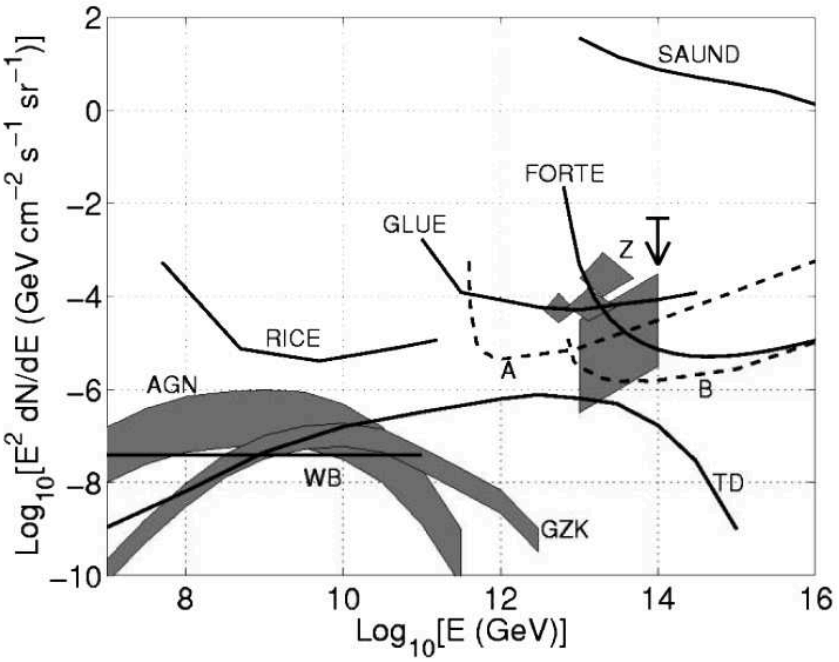

Figure 2.3: Diffuse neutrino flux limit from SAUND. The plot includes, also, results from other experiments (RICE, GLUE, FORTE, see Section 1.3.3.1) and predictions of theoretical model (AGN, GZK, topological defects, Z-bursts, WB - Waxman and Bahcall limit). Dashed lines, labeled "A" and "B", correspond to the calculated sensitivity of two Monte Carlo simulated acoustic arrays, with two different optimized geometry [142].

The ACoRNe group is also employed in some studies of sensitivity predictions from simulations of large scale hydrophone arrays [144], setting some upper limits on high-energy neutrino flux. Results have been presented at ARENA 2008 Workshop, and will be included in the conference proceedings. The activity is going on in the framework of km3Net.

Acoustic investigations inside the ANTARES Collaboration are carried on by the **AMADEUS** project. The pilot AMADEUS activities consisted in the operation of an Autonomous Module for Acoustic DEtection Under the Sea. Experience gained with the first tests allowed the group to design a more complex experiment to be integrated into the ANTARES optical telescope, for what concerns both the mechanics and the continuous data acquisition. The project has been realized implementing six acoustic storeys (three on ANTARES IL07 - Instrumentation Line, and three on ANTARES Line12); data taking is currently ongoing. The hydrophone configuration and the hydrophone type is not the same in every storey. Different possibilities concerning the device type (commercial sensors or self-made hydrophones), the device orientation and the mechanical structure hosting the acoustic modules are being explored. The goal of these ANTARES Modules for Acoustic Detection Under the Sea is to perform long-term studies of acoustic background noise and to develop algorithms of data analysis. The status of the AMADEUS project has been presented at the ARENA 2008 Workshop; conference proceedings are forthcoming.

In addition, the work discussed in [145] has been developed in the framework of the ANTARES Collaboration.

Concerning the NEMO Collaboration, several activities, related to the opportunity of acoustic detection of ultra-high-energy neutrinos, have been approached. Acoustic studies in the framework of NEMO phase-I include **OνDE** - Ocean Noise Detection Experiment [146]. The main goals of the OνDE test station, operating off-shore Catania, Sicily, in the NEMO test-site, from January 2005 to December 2006, consisted in *in situ* investigations on hydrophones and hydrophone data acquisition, and in on-line monitoring of underwater acoustic noise. The station was made up with four hydrophones, arranged in a tetragonal geometry, operating in the frequency band [30 Hz - 40 kHz]. Data analysis allowed to produce a detailed description of the acoustic noise background in the Catania site, evidencing some seasonal variations of the PSD (Power Spectral Density), that may be correlated to environmental parameters and human activities. Some initial tests on the capability acoustic source tracking have been performed. Considering the classification introduced by Urick [147], acoustic data collected with OνDE show that the average sea-noise level, in the monitored site, in the frequency band [20-43 kHz], is between Sea State 0 (SS0 - absence of sea surface agitation) and Sea State 2 (SS2 - low surface agitation and absence of identifiable acoustic source), Figure 2.4. The average acoustic sea noise measured in the same frequency band is $5.4 \pm 2.2_{(stat)} \pm 0.3_{(syst)}$ mPa RMS. This result can provide an indication on detectable neutrino-induced signals, as discussed in Section 4.3.

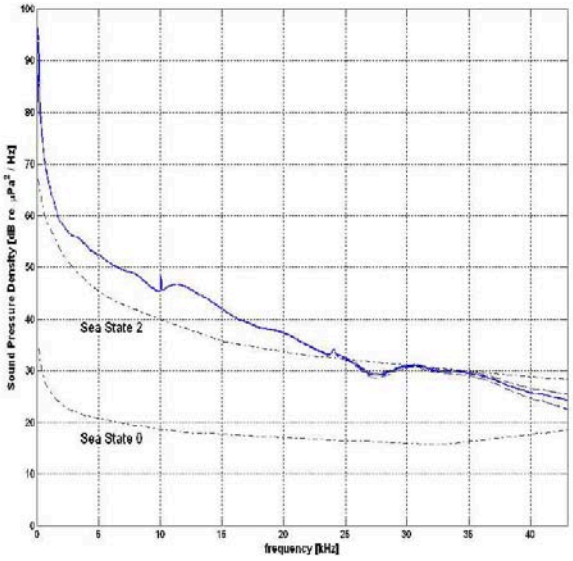

Figure 2.4: OνDE - Sound Pressure Density (SPD) of sea noise. The plot reports the average sea-noise recorded with the OνDE experiment. The black curves indicates respectively the expected SPD of the sea in conditions of Sea State 0 and Sea State 2 ([146].

The research follows a multi-disciplinary approach, with significant links with bio-acoustics. A collaboration with CIBRA[2] has produced important results concerning marine mammal population in the Ionian Sea [148], having notable echo in national and international press [149].

[2]CIBRA is Centro Interdisciplinare di Bioacustica e Ricerche Ambientali - Multidisciplinary Center for Bio-acoustics and Environmental Research - University of Pavia, Italy `http://www-1.unipv.it/cibra/`.

As anticipated in Section 1.3.2, NEMO phase-II consists in the deployment of a full-scale NEMO-tower prototype in the Capo Passero site, Sicily. The tower will be made of 16 floors, each one equipped with four PMTs and two hydrophones (plus two additional hydrophones at the tower base). This configuration of acoustic sensors responds to the need of acoustic positioning, but it is at the same time a precious opportunity to implement acoustic acquisition and investigate acoustic neutrino detection performances. **Acoustic positioning** is the current technology to measure and monitor the position of mechanical structures in underwater neutrino telescopes. Considering a submarine grid of Cherenkov light sensors (PMTs), sea currents and other mechanical solicitations may cause a displacement of mechanical structures with respect to their nominal position. Be informed of the actual position of optical modules in the grid is mandatory, in order to correctly compute time of arrivals of PMT hits and to reconstruct particle tracks. Hydrophones in the NEMO phase-II tower will thus perform a double function: they will be the devices used to carry on the acoustic position system, and they will allow a first approach to acoustic neutrino detection, constituting a test-bench for testing reconstruction strategies and data analysis algorithms.

Additional activities carried on in the framework of the NEMO Collaboration are hydrophone calibrations, simulations of neutrino-induced pulses (this work) and implementation of reconstruction algorithms and noise rejection strategies [150].

2.5 Sound in the Sea beside Neutrinos

The exploit of acoustic signals in water to detect high energy particles is, of course, the latest frontier in underwater marine research. The science of sound in water is connected to well-established **applications and technological developments** in multi-disciplinary fields of activity, as navigation, fishing, communication, oil industry, defense. Concerning more academic topics, underwater sound is an important tool of investigation for geology (seismology and volcanology), climatology and biology (marine mammals). The case of the OνDE project, presented in Section 2.4, is a significant example of this kind of multi-disciplinary research.

An interesting account on sound in water, with popular discussion on physics and applications and a lot of introductory material, is available on the web at Discovery of Sound in the Sea, http://www.dosits.org/ (September 2008). The web site, mainly developed by University of Rhode Island's (URI) Office of Marine Programs (OMP), includes a list of additional resources.

Chapter 3

Investigating the Performances of the Acoustic Technique

The ITEP Test Beam

As soon as the idea of acoustic detection of particles was proposed - by G. A. Askaryan (1957) [126] - and the possibility of applying the acoustic technique to ultra-high-energy neutrinos was advanced [127][1], the next step was to investigate the effectiveness of the thermo-acoustic mechanism and the validation of the methods, testing the model with experimental measurements. The activities carried out with proton beams by L. Sulak, J. Learned *et al.* in 1979 [152] place in this framework; their results still constitute a reference for people in the field. More recent contributions at proton accelerator facilities can be found in [153] [154] [155]. When starting to approach the topic of acoustic neutrino detection in underwater neutrino telescopes, we thus moved in the same direction, planning and performing **experimental measurements at proton beams**.

Our first intent was to enter the topic and get familiar with tools and techniques concerning acoustic detection of particles. Of course, some preliminary activity was needed. Beside the delve into the subject, and the building of the theoretical foundation through articles and reviews, the first step performed was toward the understanding of the procedures connected with acoustic pulses acquisition. Saying in other words, the first part of the work was dedicated to *hydrophones*, in order to get confident with instruments and methods and gain practice in data acquisition procedures. At this purpose, we went for calibration measurements at the Underwater Acoustics Laboratory of CNR IDAC - Institute of Acoustics "O. M. Corbino" [156]. Using their technical facilities and their precious collaboration, we have been able to measure the hydrophone sensitivity response in the frequency domain.

With the experience gained at IDAC, we got ready for *protons*: our calibrated hydrophone was used to collect pressure pulses generated as a consequence of proton beam dumping in water. The success in registering acoustic signals from protons represents a good confirmation of the thermo-acoustic model and of the feasibility of the acoustic technique for particles detection. First outcomes from data analysis produce results in agreement with expectations on energy calibration. The study of the beam profile is a first attempt in investigating some unknown or uncertain variables in the experimental setup using results from data analysis.

[1] References [126] and [127] are both cited in [151].

The activity in the field of acoustic detection has started in 2003; a report has been included in my master thesis [157] (in Italian) and has been presented at the ARENA 2005 Workshop [158]. The main topics faced in this first work are, as already introduced, hydrophone calibration in the frequency domain (IDAC data) and first results on hydrophone energy calibration, using intense low-energy proton beams as acoustic source. Data acquisition took place at the protosynchrotron medical facility in ITEP - Institute of Theoretical and Experimental Physics, Moscow, Russia [159]. Details on the experimental setup and on data acquisition are given in Section 3.2.

Despite the large amount of information already collected, the work was still in a preliminary phase, since detailed analysis and deep understanding of the phenomena were missing and further developments were needed. Most of the research carried on during my PhD was thus dedicated to the topic, with the purpose to complete the study of the ITEP test beam, improving the data analysis and profiting from the support of simulation tools. The activity is widely documented in this chapter. The material has been presented also at the ARENA 2008 Workshop [160][2].

3.1 Why protons - The Bragg peak

Before describing data analysis and simulation algorithms and entering the core of the topic, the first question to answer is *why protons*, or in other words, what are the motivations for performing hydrophone energy calibration at proton beams. These motivations come from proton therapy studies for cancer treatment and the dose-depth profile of protons in water.

Ideally, as explained in [161], the objective of any cancer treatment method is to remove or destroy the tumor while preserving at the same time the healthy tissue as much as possible. As clearly seen from Figure 3.1, different from other kind of radiation exploited in tumor therapy, protons deposit most of their energy at the end of the path, in the so-called *Bragg peak*. Therefore, proton energy deposition profile satisfies the required condition to concentrate the dose where needed, avoiding irradiation of critical organs in the vicinity of the tumor.

3.1.1 The Bragg Peak: a Simplified Physical Model

Typical energies of protons in medical beams are in the range 50-300 MeV. Detailed studies of proton interacting properties, both with data and with Monte Carlo simulations, have been widely carried out in the field of medical physics and proton-therapy.

Following the account given in [163], a quantitative approach to understand the Bragg peak behaviour comes from the simplified physical model, valid for proton energy in the medical range. Equation 3.1 estimates the average rate of loss of energy, or *Linear Energy Transfer (LET)* for a single proton passing through water:

$$\left|\frac{dK}{d\lambda}\right| \left[\frac{MeV}{g/cm^2}\right] \approx \frac{1}{0.098 \cdot k + 0.0277} \tag{3.1}$$

[2]The Conference took place in Roma University "Sapienza", Italy, in June 2008. The proceedings of the conference will be published by Elsevier Science on Nuclear Instruments and Methods in Physics Research, Section A (NIMA) [109].

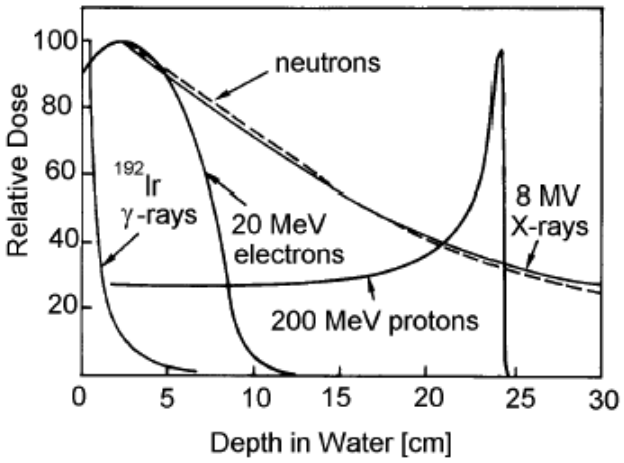

Figure 3.1: Dose-depth profiles for different types of radiation. Protons deposit most of their energy at the end of the path, in the so-called "Bragg Peak". Picture taken from [162].

Here, $k \equiv E[MeV]/100$ and E is proton instantaneous kinetic energy. Protons lose most of their energy just before they stop, as shown in plot [a] of Figure 3.2.

The exact depth at which protons stop, that is where the Bragg peak is expected and most of the energy is released, is dependent on the initial energy of the particles in the beam. Therefore, by modulating proton energy at the injector, it is possible to control the position of the Bragg peak. Equation 3.2 is a good parametrization to calculate the average *range* of protons in water, i.e. the stopping depht corresponding to the position of the Bragg peak:

$$< R > [g/cm^2] \approx 4.90 \cdot k^2 + 2.77 \cdot k \tag{3.2}$$

Here, $k \equiv E[MeV]/100$ and E is initial energy of incident protons. Taking the value $\rho = 1 g/cm^3$ for water density, and considering the cases $E = 100 MeV$ and $E = 200 MeV$, Equation 3.2 gives an expected range of about $< R > \approx 7.67\, cm$ and $< R > \approx 25.14\, cm$, respectively. Results for the computation at different initial energies are shown in Figure 3.2, plot [b].

It must be underlined that the processes here described, involving a large number of particles, are stochastic, and therefore a "straggling" has to be considered, both in kinetic energy and in range, both depending on proton injection energy. Order of magnitude of the root mean square (RMS) spread is $1\, MeV$ and several millimetres, respectively.

In addition, *Multiple Coulomb Scattering (MCS)* processes have to be taken into account, since they cause an increase angular spread and transverse size for protons propagating in water, as shown in Figure 3.3, where the range for protons (the Bragg peak placement) is put in evidence at different injection energies.

The last feature to consider is the average *transmission*, i.e. the fraction of proton beam transmitted as a function of injection energy K_0 and depth in water λ, $T = T(K_0, \lambda)$. Here again we see from Figure 3.4 that most of the particles stop at the Bragg peak.

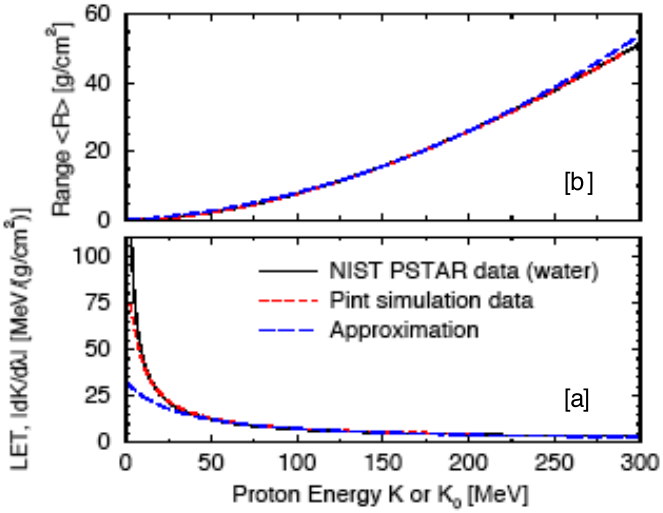

Figure 3.2: [a] LET for protons in water versus instantaneous kinetic energy. [b] Range for protons in water, versus incident kinetic energy. Data are compared with results from simulation; approximation is computed with Equations 3.1 and 3.2, respectively [163].

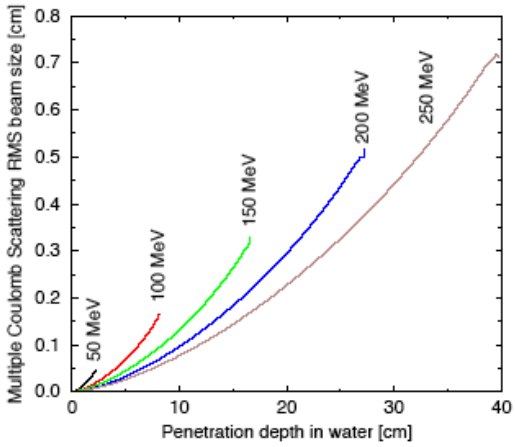

Figure 3.3: Effect of Multiple Coulomb Scattering on transverse proton beam size versus depth in water, for different initial energy values. Results from Monte Carlo simulations [163].

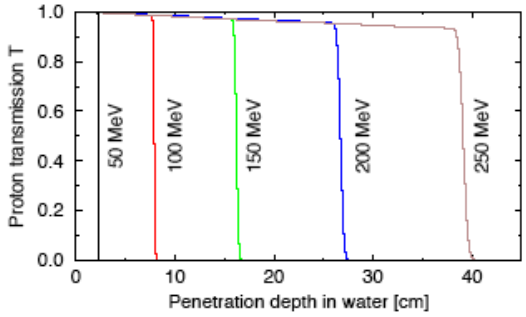

Figure 3.4: Fraction of transmitted protons versus depth in water, for different values of kinetic energy at the injection [163].

3.1.2 The Bragg Peak as Acoustic Source

The connection between protons and acoustic pulses is related to the opportunity for the Bragg peak to work as acoustic source.

Considering an intense proton beam, the Bragg peak is in fact a tiny region in the water volume where a large amount of energy is deposited in a very short time. In other words, in the position identified by the Bragg peak, there is a highly-localized and almost instantaneous energy deposition, thus fulfilling the conditions of the thermo-acoustic mechanism for pressure pulse generation. The approximation of instantaneous energy release holds on because particles in the beam propagate at about the speed of light $c \approx 3 \cdot 10^8\, m/s$, and thus several orders of magnitudes larger than the speed of sound in water, $v \approx 1.5 \cdot 10^3\, m/s$. Reasoning in terms of time, the interval during which the energy deposition occurs can be estimated as $\tau_{dep} = R/c$ with R longitudinal extension of the acoustic source (the range of protons), while the time scale of the thermo-acoustic mechanism depends on hydrodynamical transport: $\tau_{hydro} = r/v$, with r lateral extension of the source. Since for protons in medical beams $R \approx 10^{-1}\, cm$ and $r \approx 10^{-2}\, cm$ (see Figure 3.3) we get $\tau_{dep} \approx 10^{-9}\, s$ and $\tau_{hydro} \approx 10^{-5}$. As a conclusion, then, the Bragg peak can be considered as a case of acoustic source from which we expect detectable pressure pulses according to the thermo-acoustic mechanism, and for which the Poisson formula can be applied. This last point is very important, since it allows to define the computation algorithm for simulation.

The last comment concerns the shape of the Bragg peak as acoustic source, since it is expected to be axially symmetric along the direction of particles propagation, the same as it is the case of neutrino-induced cascades.

3.2 Data-Taking at the ITEP accelerator facility

The second question that needs an answer is: where do our data come from? Or, what was the experimental setup we met and used in ITEP during our data acquisition?

Here I will report in short some information on the data taking, paying attention in particular to important facts to understand the basic operations performed to get the comparison between data and simulations. Additional details can be found in [157] and in [158].

An important comment must be added. As it will be clear in the following, the most important source of uncertainty in results is due to indeterminacy in the knowledge of some features that define the experimental setup.
Going on with data analysis and with the building of the simulation frame, it has become evident that a more deep understanding and control of some parameters would have been necessary to provide a better description, and therefore a better reproduction, of the experiment in the simulation. As it will be underlined in the conclusions, this reasoning provide the first recommendation and guidance for future experiments with calibration beams. The study carried on with the ITEP beam has thus allowed to establish the directives to follow for a better modelling of the phenomena.

3.2.1 Geometry

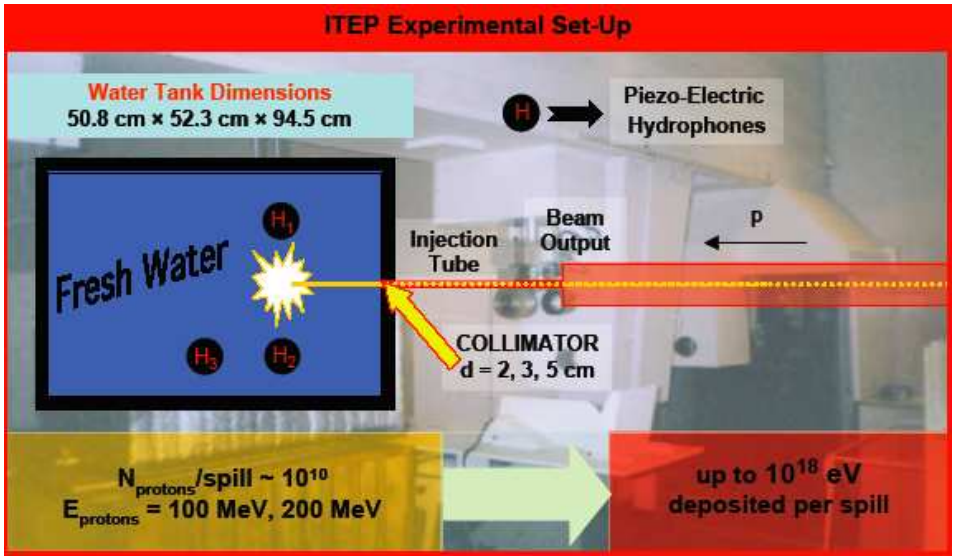

Figure 3.5: Sketch of the experimental setup at the ITEP protosynchrotron facility. The relevant elements of the data taking are in evidence. Details in the text.

Figure 3.5 is a sketch of the experimental setup in ITEP. The beam line ends into a plastic tank whose shape is a parallelepiped and whose dimensions are $L_x = 94.5\,cm, L_y = 50.2\,cm, L_z = 52.3\,cm$ (assuming x as the beam axis direction and z along the vertical). Dimensions listed above refer to the outer sides of the tank, while the inner walls are covered with phono-absorber material. The tank is $\approx 90\%$ filled with fresh water. Taking into account the lack of information concerning the inner volume of the tank and the actual amount of water inside the tank, one can estimate uncertainties in the geometry of the order of some percents. Nevertheless, these uncertainties do not affect the modelling: as it will be shown in the next (Section A.2), the Monte Carlo simulation picks out the essentials of the setup, and does not involve tank boundaries, making these uncertainties unimportant.

As shown in Figure 3.5, three piezo-electric hydrophones are placed inside the tank, but only hydrophone H_1 will be considered in the further analysis. A mechanical support, designed to reduce reflections, holds up the hydrophones in the middle of the tank, at about the same vertical measurement of the beam line. Hydrophone H_1 is placed where the Bragg peak is expected: measuring distances from the protons entrance point in the tank, the value is fixed at $7.5\,cm$ for injection energy $E = 100\,MeV$, and $25.5\,cm$ for injection energy $E = 200\,MeV$. The hydrophone is maintained at $10.5\,cm$ from the shower axis.

The most important fact to notice is that in the simulation the hydrophone is treated as a point-like receiver, neglecting its spatial extension, that is of some centimeters in diameter, therefore the same order of magnitude of uncertainties in the hydrophone position itself. These uncertainties can therefore affect the results of the simulation. The "tuning" of the hydrophone position in the computation will play a relevant part in the comparison between experimental pulses and simulated ones (Section 3.6.3).

3.2.2 Environmental Parameters

Since water in the tank is the target medium of our experiment, a detailed monitoring of environmental parameters, such as water temperature, water salinity, atmospheric pressure, should be imperative. Regrettably, this control was lacking during the data taking The only information available is on water temperature at the very beginning of the acquisition session ($T = 18.1\,C^{\circ}$), but data taking lasted all night long, and ambient temperature sensibly decreased.

As it will be discussed in Section 3.4.3, information on environmental parameters, and on temperature in particular, is crucial to calculate the *Gruneisen coefficient*, that determines the acoustic pulse amplitude. This lacking of information produces additional uncertainties in the predictions.

3.2.3 Acquisition

Data have been acquired with hydrophones connected to an oscilloscope. Sampling frequency is $f_{EXP} = 10\,MHz$, corresponding to a sampling period of $t_{EXP} =$ 100 ns.

An **event** is a single occurrence of the phenomenon of protons injection and energy deposition in water, and subsequent pressure pulse generation and recording with hydrophone. Each event corresponds to a single acquisition file and it is made of 10^4 samples. Each acquisition file registers time in seconds and amplitude in Volt.

In Figure 3.5 there is an indication of energy and collimators. As already mentioned above in the text, the two values selected for the injection energy of protons in the beam are $E = 100\,MeV$ and $E = 200\,MeV$.

Concerning collimators, they have been placed just before the entrance point of protons into the water tank. The reason for this is to collimate the proton beam, reducing irregularities in the beam profile. Available values for the collimator diameter are $d = 2\,cm$, $d = 3\,cm$, $d = 5\,cm$.

The beam intensity is measured via a Beam Current Transformer (BCT); the number of protons is proportional to the amplitude value A_{BCT} registered by the BCT:

$$N_{protons} = 2 \cdot 10^8 \cdot K \cdot A_{BCT}[\text{Volt}] \tag{3.3}$$

where K is a parameter regulated by machine settings. As sketched in Figure 3.5, the number of particles injected for each event is of the order of 10^{10} protons per spill.

A **run** is a collection of events, each one with the same characteristics for what concerns intensity scaling factor K, injection energy and collimator applied. For each configuration (K, E, d), several events have been collected, producing a large amount of raw data.

Equation 3.3 gives the number of particles extracted from the protosynchrotron and *not* the number of particles entering the tank, since protons measured via the BCT have to pass through the collimator, that reduces the intensity. This means that we do not have a direct measurement of the actual number of protons interacting in water, and thus responsible for the acoustic source. This lack of information, together with the indetermination associated with the beam profile, provide the most important source of uncertainty in the analysis.

3.2.4 Beam Profile

The beam profile in time was attested as a $\cos^2(t)$ function, with full-width-half-maximum (FWHM) of $68\,ns$. These data have not been considered in the further analysis, since energy deposition is taken as instantaneous in the simulation.

Information available on the beam profile in space is particles having an axially symmetric Gaussian distribution along the beam axis. Unfortunately, no further details were provided, in particular on the "size" of the beam (the "sigma" of the Gaussian distribution). The Gaussian hypothesis itself represents only an ideal case, because fluctuations and irregularities in the proton extraction can occur. The collimator plays a role, also, since it may not be centered at the beam axis. These uncertainties prevent to determine the distribution and the number of protons depositing energy in water, and therefore limit our potential to make predictions about the acoustic source and thus the acoustic pulse itself.

As it will be clear in the next, modelling the beam profile is therefore a crucial point: most of the investigations in the Monte Carlo simulation will be dedicated to the acoustic pulse dependence on the proton beam distribution in space (Section 3.6.2).

3.2.5 Hydrophone

The hydrophone considered in data analysis is manufactured by BENTHOS[3]. Since it is a dedicated prototype, no official data sheet is accessible, and the only available information is that obtained during the IDAC calibration measurements. A short description of the calibration procedure at IDAC includes a mention of the IDAC calibrating source producing a sine wave pulse, whose frequency was in the range $(5.00-25.0)kHz$, sweeping with a step of $0.5kHz$, for a total of 41 data points in the sensitivity/frequency plane.

In principle, the knowledge of the hydrophone transfer function is mandatory to get the response in Pascal from the registration in Volt, but unfortunately, beside the IDAC test measurements, no further study on the transducer calibration has been carried out. Therefore, since a detailed model of the hydrophone and of the hydrophone response in the frequency domain is not available, some assumptions are needed to proceed.

Typical information from specification sheets for high-depth hydrophones assures a flat frequency response up to about $50\,kHz$, where mechanical resonances start to occur (see, for instance, Figure 3.6). These sensitivity plots give grounds for my assumption of a simplified model with a constant value for the hydrophone transfer function. The assumed constant value is the average value from the IDAC calibration set, that is about $-173\,dB\,re\,1\,V/1\,\mu Pa$. Since at first stage what is important is to convert Volt to Pascal, the simplified hydrophone model seems enough to assure a good comparison of experimental data with simulations.

[3] `http://www.benthos.com/`

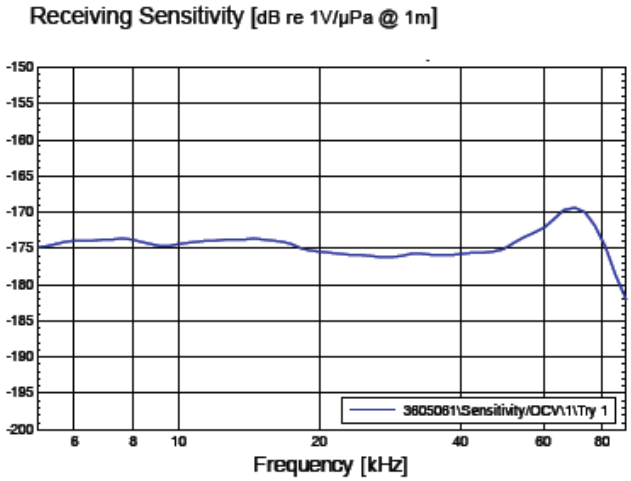

Figure 3.6: Receiving sensitivity for hydrophone RESON TC4042. Hydrophone considered in data analysis is fairly similar. A product of the same series has been employed both in the IDAC test and in the ITEP test. Picture taken from [164].

3.3 Signal Processing on Hydrophone Data

To take into account the losing in sensitivity at higher frequency, I apply a second order Butterworth filter on voltage acquired data. Signal processing has been performed testing the cut-off frequency at three different values (50,100 and 150 kHz) and comparing the results (Figure 3.7 and 3.8). Motivations for filtering the data are as follows: the frequency content above the cut-off threshold should be rejected since, as it is beyond the hydrophone sensitivity, should not have a physical meaning connected with acoustic phenomena, but should have an intrinsic mechanical (resonances) or electrical origin.

In modelling the protons interaction in water and the pressure pulse generation, it is more interesting to examine some sample cases, rather than the whole set of raw data. A selection on raw data has thus been conducted, taking into account only those runs with the largest K, in order to have a large number of protons interacting in water, a subsequent great amount of deposited energy, and therefore a pressure signal well separated from noise. As a consequence of this selection, I keep on considering 6 runs only, one for each couple of values (E,d = energy, diameter of the applied collimator)[4].

Since each run represents a sample configuration, the next step consists on computing the average signal for each run, that is the average event for a specified acquisition condition. Of course, this processing, performed with a dedicated script (run.csh script, that runs executable files compiled from read.cc, sum.cc and average.cc) has the consequence of smoothing the signal, cancelling some of the random noise of the single acquisition. Additional smoothing is achieved with the filtering procedure on the average signal, as discussed above.

Figure 3.7 shows the results of the described procedure of signal processing on hydrophone data. Figure 3.8 display the same signal in the frequency domain. Figure

[4]Selected runs are schematically referred to as: E1d2, E1d3, E1d5, E2d2, E2d3, E2d5.

3.9 (time domain) and Figure 3.10 (frequency domain) compare acoustic pulses on the same plot, to point out differences due to configuration settings (E, d). Details in captions; filtering, Fourier transform and visualization are performed with Octave[5].

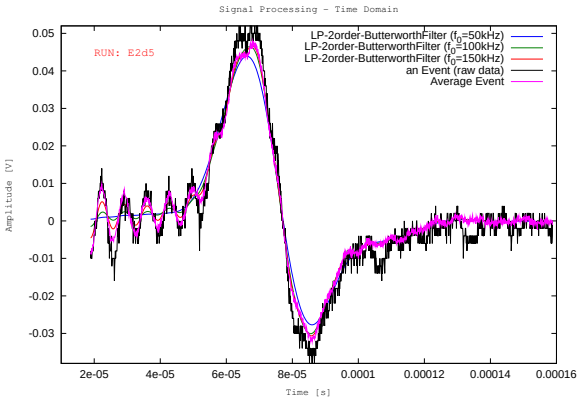

Figure 3.7: Signal Processing on Experimental Data - Time Domain. The plot illustrates the effects of signal processing performed on hydrophone data, taking the case of run E2d5 (injection energy E = 200 MeV, collimator diameter d = 5 cm). The horizontal axis is time, time origin is at the proton injection into the tank. The black line is raw data. Line in magenta is the result after averaging all events in the run. Blue, green and red lines represent the average signal after the apply of a second order low-pass Butterworth filter with a cut-off frequency of 50, 100, 150 kHz, respectively. Data filtering and visualization are performed with Octave.

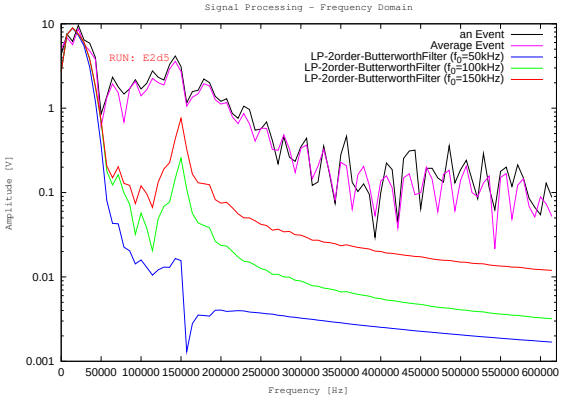

Figure 3.8: Signal Processing on Experimental Data - Frequency Domain. Signals displayed in Figure 3.7 are shown in the frequency domain. The frequency scale extends up to the Nyquist frequency ($f_N = 5\ MHz = \frac{1}{2}f_s$, where f_s is sampling frequency), but the display is up to 625 kHz $\left(\frac{f_s}{16}\right)$, to better evidence the lower part of the spectrum. The vertical axis is the absolute value of Fast the Fourier Transform (FFT) in logarithmic scale (computation carried out with Octave). The effect of filtering is in evidence. The peak at about 150 kHz is interpreted as mechanical resonance of the hydrophone.

[5]GNU Octave is a high-level language, primarily intended for numerical computations, mostly compatible with Matlab (MATLAB is a registered trademark of The MathWorks, Inc., `http://www.mathworks.com/`). More about Octave on [165].

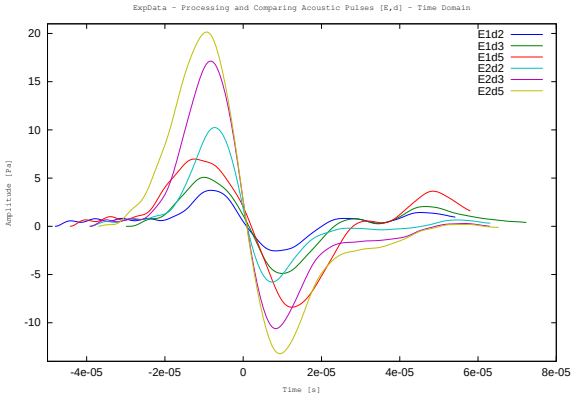

Figure 3.9: Hydrophone Data - Comparison of Acoustic Pulses (time domain). For each run (Note 4), the average event is processed according to procedure described in Section 3.3. Selected cut-off frequency in the filter is $50\,kHz$. Volt-to-Pascal conversion, as discussed in Section 3.2.5, is included. To better compare results, time axis is translated for each signal, in order to place the origin at the pulse centre $t_0 = [t(A_{min}) + t(A_{max})/2]$(see parametrization introduced in Section 3.6.3).

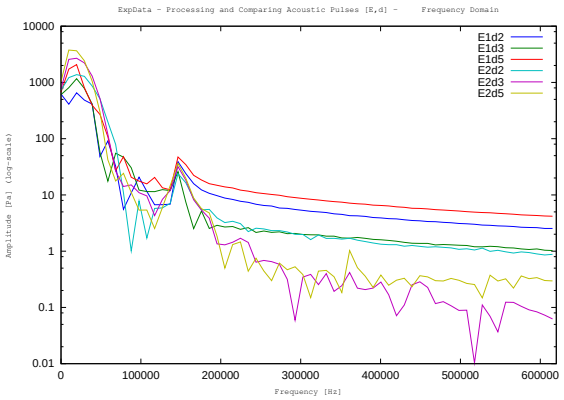

Figure 3.10: Hydrophone Data - Comparison of Acoustic Pulses (frequency domain). The frequency content of signals in Figure 3.9 is plotted. See caption of Figure 3.8 for comments on horizontal and vertical axes.

3.4 Monte Carlo Simulation

The employment of the Monte Carlo simulation gives the opportunity to complete the data analysis, going in depth into the understanding of the phenomenon of thermo-acoustic mechanism of acoustic signal generation.

Introducing a schematic view, the simulation chain can be split up in two main sections, one dedicated to the Monte Carlo simulation of the acoustic source (**AcSource**), the other one aimed at the computation of the acoustic pulse from a known energy deposition scheme (**AcPulse**).

Additional minor elements can be considered in the simulation chain, depending on the level of details one wants to include. For instance, the environment description can be taken into accounts, at several levels of approximation. The first stage is the case considered in my code, that is the parametrization of the Gruneisen coefficient

as a function of water temperature, salinity and depth. Details will be presented in Section 3.4.3. Figure 3.13 reports the block diagram of the **simulation chain**, as sketched above.

Advanced environment description implies a detailed point-to-point simulation of the medium in which propagation takes place, considering a field of temperature and salinity, and thus a field of sound velocity.
A parallel development evaluates the effect of attenuation, that becomes important at larger distance from the source. Therefore, considerations on attenuation are postponed in Chapter 4, when the neutrino case is examined.

Further components in the simulation, that get important when starting to define acoustic detector prototypes, require advanced hydrophone modelling, beyond the simple solution described in Section 3.2.5, to predict the receiver response.

3.4.1 AcSource: The GEANT 4 Monte Carlo Simulation Code

Keeping concentrate on the two major simulation steps, let's start with describing the AcSource code.

The goal is to reproduce the acoustic source, that is the pattern of energy deposition in the volume interested by particles interaction. Considering the case of protons involved in the ITEP test beam, energy deposition is computed with Monte Carlo techniques to take into account protons propagation and interaction in water.

3.4.1.1 Geant4

The tool employed to get the energy deposition map that works as acoustic source is Geant4 (GEometry ANd Tracking) [166] [167][6]. This simulation framework, developed at CERN, represents the evolution towards C++ object-orienting programming of the GEANT project, originally advanced at CERN in the '90s and written in Fortran, to simulate the passage of particles through matter. As the name itself explains, the code is best suited for reproducing a complex experimental setup where particle propagate and interact. Applications include high-energy physics (accelerator physics and simulation of detector response), space and radiation, medical physics (including proton therapy and hadron therapy for cancer treatment). A large international collaboration of people works to build and improve the code. The web-page [168] widely documents the concepts, the structure, the usage and the applications, with examples and tutorials. User Manuals are available, as well.

3.4.1.2 Geant4 Simulation of the ITEP Test Beam

A detailed discussion on the Geant4 simulation of the ITEP test beam is accounted in Appendix A. Attention is given to the structure of the *main* program, and to the so-called *Mandatory User Classes*, that are required to define the geometry (sensitive volumes and materials), the physics processes and the primary generator properties. This last point, in particular, assumes a key-role since, as it is investigated in Section 3.6.2, differences in the primary generator settings determine differences in the energy deposition, and therefore in the acoustic source.

[6] The Geant4 version used to build the ITEP application is geant4-09-00-patch-01 (28-August-2007).

Results of the AcSource simulation are shown in Figure 3.11 (geometry only) and 3.12 (geometry and particle tracks), details in caption.

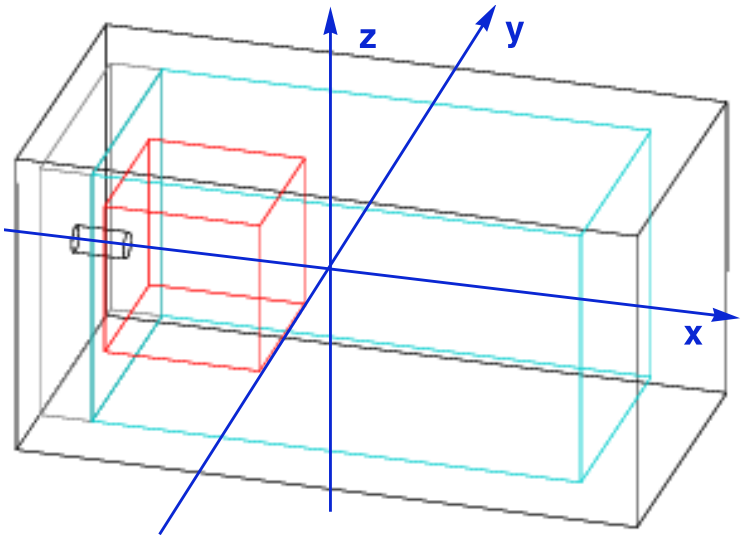

Figure 3.11: Geant4 Simulation - Geometry only. The outermost black contour is the mother volume, which is set visible. The blue contour identifies the water basin, centered at the mother volume. The grey contour next to the water basin indicates the lead screen; the cylindrical hole that plays the role of the collimator is in evidence. The cubic red contour inside the basin delimits the sensitive detector. As explained in Appendix A, subdivision in cubic cells is set invisible to speed up visualization. The picture is produced with the Geant4 graphics tool DAWN Event Display (`http://geant4.kek.jp/~tanaka/`). The axes of reference are added.

Optional User Action Classes are implemented to manipulate the outcome of the simulation and produce the output file, in the form of a "map" of energy density *rhoEmap*, that "feeds up" the AcPulse code.

3.4.2 AcPulse

The AcPulse code is the next step in the simulation chain. Output from AcSource becomes input for AcPulse.

The algorithm of computation is based on the **Poisson formula** (see Chapter 2). The idea is to reproduce a discrete computation of the integral solution as expressed in Equation 2.3. I tried several versions, implemented in different programing languages; the current version I use is written in C.

In the following I will analyze the AcPulse code in details. The main topics are listed in the sketch reproduced in Figure 3.13, that is the block diagram illustrating the algorithm of computation implemented in AcPulse and integrated in the full simulation chain. The source code used to produce the results shown in this Chapter is included in Appendix C.

The input file, that is the acoustic source *rhoEmap*, is passed as the argument of the AcPulse program.

The main system of reference S comes from the frame of reference in which the acoustic source is specified. In the case of the ITEP test beam Monte Carlo, the

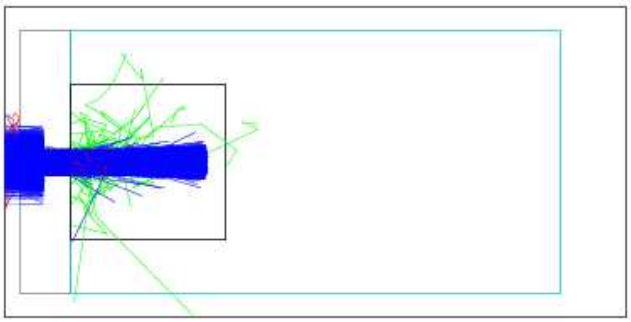

(a) Geant4 Simulation: side-view

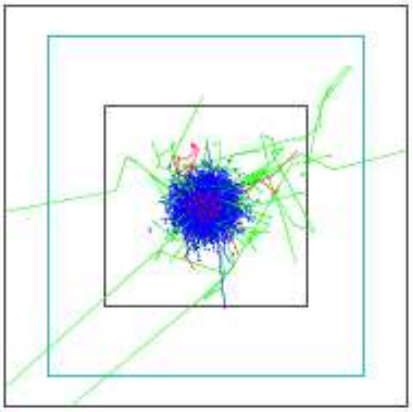

(b) Geant4 Simulation: front-view

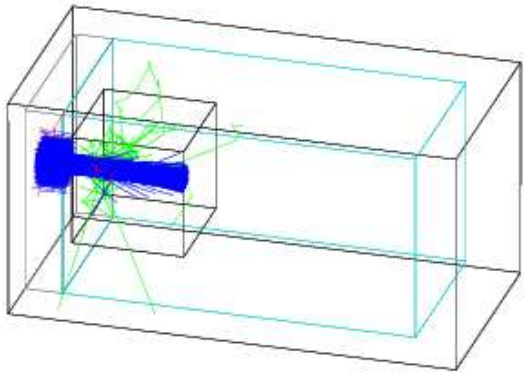

(c) Geant4 Simulation: view in perspective

Figure 3.12: Geant4 Simulation - Geometry and Particles: visualization of the full simulation of the ITEP application. Results refer to Run $E2d5n3N4$, with proton injection energy $E = 200MeV$ and collimator diameter $d = 5cm$; 10^4 primary protons are simulated, distributed according profile $n = 3$ (see details in Section A.4 and Table 3.1). Geometry presented in Figure 3.11 is completed with the add of particle tracks, both primary protons and secondary particles produced in protons interactions with water. According to Geant4 color legend, blue lines are proton tracks (positive particles), red lines are electron tracks (negative particles), green lines are photon tracks (neutral particles). Results are presented from three different points of views, obtained changing the camera angle settings, in order to offer a full description of the simulation. The most important fact to notice is that, as already underlined in Section A.2, the sensitive detector is large enough to contain most of the particle trajectories, that is most of deposited energy. Only some low-energy photons can escape from the shower core, carrying away a small amount of energy, whose contribute can be neglected. In Subfigure [a] and [c] the effect of the collimator is in evidence. Protons are generated following the selected beam profile; the lead screen stops the ones that are produced outside the diaphragm window. Proton tracks development in the water tank is in agreement with the Bragg peak behaviour: range and fluctuations are as expected for a $200MeV$ injection energy value, according to the Simplified Physical Model presented in Section 3.1.1 . Subfigure [b] shows that shower development is axially symmetric. Pictures are produced with the DAWN Event Display.

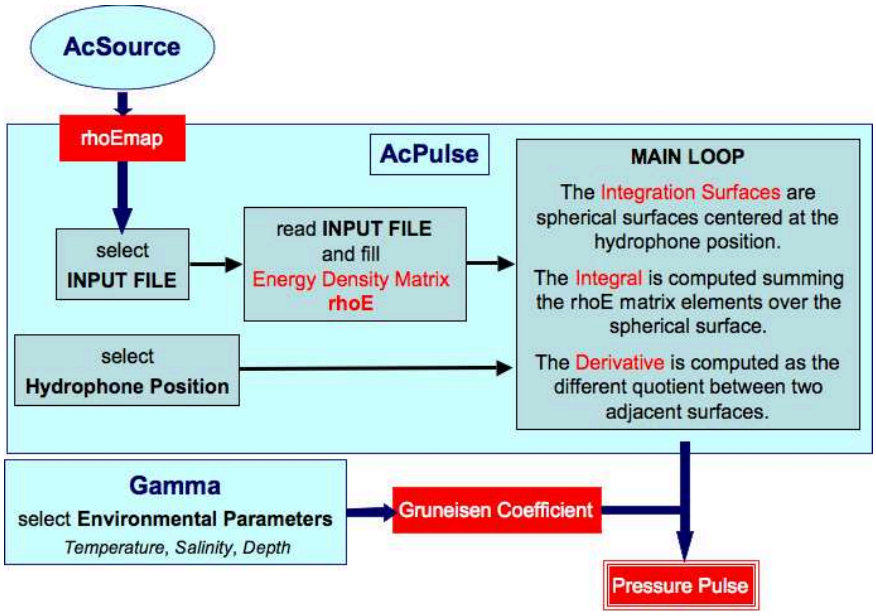

Figure 3.13: Computing the Acoustic Pulse: the Simulation Chain. The sketch represents the block diagram for the computation of simulated acoustic signals. The three main blocks (AcSource, AcPulse and Gamma) are in evidence.

AcSource defines a set of Cartesian coordinates (O, x, y, z) centered in the middle of the water tank (target volume), as illustrated in Figure 3.11.

The reference system $S^{'}$ is a set of **spherical coordinates** (H, R, θ, ϕ) placed at the hydrophone position $H = (xH, yH, zH)$, given in the system S. Range of variables is:

$$\begin{cases} R = (R_{min}, R_{min}) \\ \theta = (0, \pi) \\ \phi = (0, 2\pi) \end{cases} \tag{3.4}$$

Hydrophone position $H = (xH, yH, zH)$ is specified inside the source code. Defaults values are hydrophone nominal position at the ITEP test beam (see 3.2.1, page 50): $zH = 0$, $yH = 10.5\ cm$, xH depending on proton injection energy, since hydrophone is placed where the Bragg peak is expected. In system of reference S, this is $xH = -39.75\ cm$ for E=100 MeV, $xH = -21.75\ cm$ for E=200 MeV. The hydrophone is assumed point-like.
A detailed comparison between simulated pulses and acquired ones requires a deeper inquiry on hydrophone position. As underlined in Section 3.2.1, in fact, the order of magnitude of indetermination on hydrophone position, due to the spatial extension of the hydrophone itself, is not negligible with respect to to the order of magnitude of distance between the acoustic receiver and the acoustic source. In Section 3.6.3, investigations on hydrophone position are carried out, in order to study the effect on signal shape.

The selection of the system of reference $S^{'}$ is motivated with the choice of taking, as a point of reference for the AcPulse algorithm, the formulation in Equation 2.3, where the pressure pulse $p(\vec{r}, t)$ is computed operating a two dimensional integration and a derivative.

Integration surfaces are spherical surfaces centered at the hydrophone position $\vec{r} = H$. R variable identifies the **radius** of the integration spheres. It is connected to the time variable:

$$t = \frac{R}{v} \qquad \text{and} \qquad R = v \cdot t \tag{3.5}$$

with v propagation speed of the perturbation, assumed as constant (propagation in a homogeneous medium). The R variable thus defines the *time evolution* of the acoustic pulse at the fixed hydrophone position.
To better understand the topic, we can consider each portion of the extended acoustic source as a point-like source itself, that generates a perturbation travelling as a pressure wave in the homogeneous medium, at the assumed constant speed of sound. Elementary contributions sum up, constituting the acoustic pulse, and the sum depends on location in space where the total perturbation is measured. Under the assumed hypothesis of instantaneous energy deposition, each portion of the acoustic source pops up simultaneously, and therefore the only cause producing a difference in time of arrival on the receiver is the different distance that each contribution has to travel. In other words, the time evolution of the perturbation is due to the fact that different contributions coming from different portions of the acoustic source can reach the receiver at different times, depending on the distance between the hydrophone and the source point. The R (distance) interval (R_{min}, R_{min}) is thus connected to the t (time) interval (T_{min}, T_{min}) (Equation 3.5). R interval must be large enough to include the whole acoustic source, so that every contribution to the total acoustic signal has the time to reach the receiver.

The variation dR (indicated as *rstep* in the AcPulse code) plays a role when computing the derivative as difference quotient. The smaller it is, the more accurate the computation, since it is connected (through Equation 3.5) with dt (*tstep*), that is the sampling time of the simulated signal, and, of course, a smaller sampling time means a better description of the pulse shape. However, the dR value has a lower constraint, given by AcSource settings in defining the detector geometry. Considering the AcPulse code, the constraint is the *grid* parameter, whose value is the side of the sensitive cell, that is the binning of the computation in the Geant4 Monte Carlo simulation. If *rstep* is set smaller than *grid*, effects of discretization become pronounced, since we go below the maximum allowed resolution.

Concerning the **angular variables**, integrating over spherical surfaces in spherical coordinates means performing a two dimensional integral in θ and ϕ. As listed in Equation 3.4, the interval of definition of angular variables includes the whole solid angle. N and M parameters in the AcPulse code define the angular step (*thetastep* and *phistep*): $d\theta = \frac{\pi}{N}$, $d\phi = \frac{2\pi}{M}$. The larger are N and M, the smaller are $d\theta$ and $d\phi$, and therefore the more accurate is the computation of the integral over spherical surfaces. On the other hand, the increase of angular resolution has, of course, an effect on computation time, that thus grows with N and M[7].

[7] As it will be shown in Chapter 4, if the distance between the acoustic source and the acoustic receiver increases, it is not necessary to integrate over the whole solid angle, since the angular extension of the source is reduced with hydrophone placed far away. In this case, a re-normalization factor has to be included, to take into account the correction. At the same time, if distance between the source and the receiver increases, a larger angular resolution is required to get a better

It is important to underline that passing from the Poisson Formula to the AcPulse algorithm, computation moves from a continuous to a discrete space of parameters. As it will be clear further on, this has an effect in computing the Jacobian of the transformation.

After the setting of all the relevant parameters, we come to the core of the computation algorithm.

The first action consists in opening the input file and scanning it in order to get a measurement of the geometric boundary in x, y and z of the acoustic source. This operation is essential, since it allows to allocate and initialize the three dimensional ***rhoE* array**, hosting the energy deposition map. Each element of the array $rhoE[i][j][k]$ contains the energy density value in the sensitive cell identified by the indexes $[i][j][k]$. This part of the source code is strongly depending on the AcSource details, since features concerning the reading of the input file and the allocation of the *rhoE* array are determined by the input file format[8].

Once that the *rhoE* is correctly defined, it is ready to be filled with information from the AcSource. Therefore, the input file is scanned a second time. The goal is to convert information on the cell position as given in the input file in a set of array indexes $[i][j][k]$, in order to properly set the *rhoE* array elements. This operation determines the energy density map used in calculating the pressure pulse.

The next action in the computation algorithm is the **main loop** where the integration and the derivative are performed.
In short, we can figure this loop as a "pointer" of increasing length (length increases in steps of dR), applied at the hydrophone position, moving all around over spherical surfaces, scanning the space. If the pointer intercepts a cubic cell in which energy deposition density is not equal to zero, the density value is kept and accumulated. Just before the increment in the pointer length, derivative is computed between two adjacent spherical surface, with the difference quotient method, giving rise to the bipolar pulse. Sketch in Figure 3.14 is a schematic representation of this procedure.

In details, looking at the AcPulse code, computation in spherical coordinates is carried out through three nested loops, in which the values R, θ and ϕ, identifying the current position of the pointer, are calculated. Then, the code checks if the current position is intercepting a location in space where some energy may be deposited. If the selected position points outside the acoustic source boundary, the loop moves forward to the next position for the pointer. Otherwise, the content of the corresponding *rhoE* array element is taken and it accumulates in the F variable, that represents the integral $I(R)$ on the spherical surface of radius R. The following lines are extracted from the code in Appendix C.

```
for (iR=0;iR<nbinR;iR++)
  {
    R=Rmin+rstep*iR;
    for (itheta=0;itheta<=N;itheta++)
      {
        theta = PI*itheta/(N-1); // theta assumes (N+1) values from 0 to PI
        iZ = 1+RoundDouble((zH + R*cos(theta)-Zmin)/grid);
```

description of the pressure pulse. This is obtained selecting larger N and M values. The reduced interval of definition for angular variables, together with the increase of N and M represents a good compromise in limiting the computation time, without losing in resolution.

[8] As it will be discussed in Chapter 4, if the acoustic source is assuming axial symmetry in cylindrical coordinates, the *rhoE* array is two-dimensional.

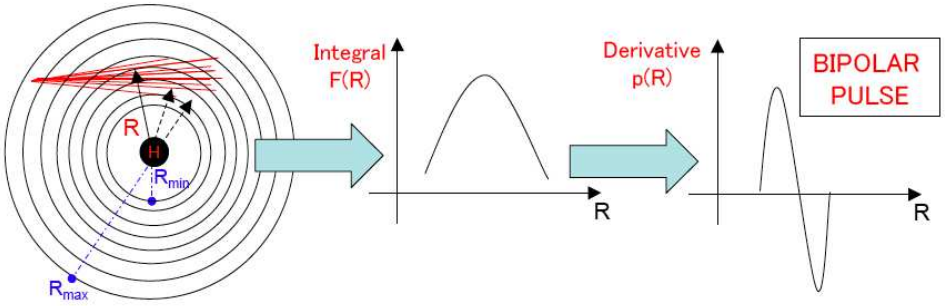

Figure 3.14: Sketch of the AcPulse main loop procedure. Picture on the left is a schematic view in two dimensions. Red tracks represent protons interacting in water and delimit the acoustic source. Circles are plane sections of spherical surfaces of increasing radius R, from R_{min} to R_{max}. The black dot in the centre identifies the hydrophone position, from where the pointer, denoted by the black arrow, goes on scanning the space all around. Next pictures represent qualitatively the integrated energy density and the bipolar pulse, to give an idea of what expected after the integration and the derivative operation, respectively.

```
          if ((iZ>nZ)||(iZ<=0)) continue;
          for (iphi=0;iphi<=M;iphi++)
            {
              phi = 2*PI*iphi/(M-1); // phi assumes (M+1) values from 0 to 2*PI
              iX = 1+RoundDouble((xH + R*sin(theta)*cos(phi)-Xmin)/grid);
              if ((iX>nX)||(iX<=0)) continue;
              iY = 1+RoundDouble((yH + R*sin(theta)*sin(phi)-Ymin)/grid);
              if ((iY>nY)||(iY<=0)) continue;
              // rhoE[iX][iY][iZ]=q(R,itheta,iphi) is energy density
              F = F + (rhoE[iX][iY][iZ])*sin(theta);
            }
        }
// DIFFERENCE QUOTIENT
      pulse = DIMfact*PI/(2.0*N*M)*(F+R*(F-Fprev)/rstep); // [Pa]
      Fprev=F;
    }
```

An additional comment has to be made concerning the derivative. The adopted formulation results from a simplification of the Poisson Formula (Equation 2.3), taking into account a fundamental property of calculus. The integrand is a function of three variables (R, θ, ϕ), but the integral in two dimensions, with the surface element $d\sigma$ in spherical coordinates given by:

$$d\sigma = R^2 sin\theta \, d\theta \, d\phi \tag{3.6}$$

This means that the R dependence has not to be integrated, and thus it can be placed "outside" the integral. Result of the integration will be a function of R only. Derivative can be solved with the product rule. Therefore, Equation 2.3 is manipulated as follows:

$$\begin{aligned} p(\vec{r},t) \propto \frac{\partial}{\partial R} \int_{S_{\vec{r}}}^{R} \frac{q(R,\theta,\phi)}{R} R^2 sin\theta \, d\theta \, d\phi \rightarrow \frac{\partial}{\partial R} R \int_{S_{\vec{r}}}^{R} q(R,\theta,\phi) \, R^2 sin\theta \, d\theta \, d\phi \\ \rightarrow \frac{\partial}{\partial R} \left[R \cdot I(R) \right] \rightarrow \left(R \frac{\partial I(R)}{R} + I(R) \right) \end{aligned} \tag{3.7}$$

from which the formulation used in the AcPulse algorithm arises, replacing the derivative with the difference quotient.

A result from calculus is also the coefficient $\frac{\pi}{2 \cdot N \cdot M}$ used in the computation. It derives from the Jacobian[9] of the coordinate transformation (C: θ, ϕ)→(D: $i\theta$, $i\phi$), where "C" indicates a set of continuous variables, and "D" refers to the discrete set. Since the transformation is given by:

$$\begin{cases} \theta = i\theta \cdot \frac{\pi}{N} \\ \phi = i\phi \cdot \frac{2\pi}{N} \end{cases} \tag{3.8}$$

the Jacobian matrix for this coordinate change is:

$$J = \begin{bmatrix} \frac{\partial \theta}{\partial i\theta} & \frac{\partial \theta}{\partial i\phi} \\ \frac{\partial \phi}{\partial i\theta} & \frac{\partial \phi}{\partial i\phi} \end{bmatrix} = \begin{bmatrix} \frac{\pi}{N} & 0 \\ 0 & \frac{2\pi}{M} \end{bmatrix} \tag{3.9}$$

Therefore, the Jacobian determinant is:

$$|J| = \frac{2\pi^2}{N \cdot M} \tag{3.10}$$

that, considering the $\frac{1}{4\pi}$ factor in Equation 2.3, reduces to the coefficient used in the AcPulse code formula.

Still on coefficients included in the computation, *DIMfatc* is a parameter applied so that the pressure pulse can be expressed in Pascal [Pa].

In addition, the role played by environmental parameters has to be taken into account. Their effect can be expressed through the Gruneisen coefficient. On the topic, a separated account will be given in the next Section.

3.4.3 The Gruneisen Coefficient

As already pointed out in Chapter 2, considering the thermo-acoustic mechanism of pressure pulses generation, the dependence of the signal amplitude on physical properties of the medium can be condensed in the Gruneisen Coefficient Γ:

$$\Gamma = \frac{\beta \cdot v^2}{C_p} \tag{3.11}$$

with β [$^\circ C^{-1}$] thermal expansion coefficient, v [m/s] sound speed, C_p [$J/(kg \cdot ^\circ C)$] specific heat coefficient. These three coefficients are strongly dependent on environmental parameters, and on **temperature** in particular.
The Grunesien coefficient quantifies the efficiency of the thermo acoustic mechanism, that is the efficiency in converting thermal energy into energy propagating as a pressure wave.

[9] The Jacobian (named after the German mathematician K.G.J. Jacobi) is the shorthand for the determinant of the Jacobian matrix, that is a first-order partial derivative matrix defining a transformation of coordinates. The Jacobian determinant is a multiplicative factor included when making a change of variables in multi-dimensional integrals. For this topic, and for calculus in general, refer to Piskunov's textbook [169].

The Gamma factor appears as a multiplicative term in the Poisson Formula (Equation 2.3). To include it in the algorithm for acoustic signals computation, a parametrization is occurring, considering in particular the effects of temperature variations. Starting from Equation 3.11, this means to look for a parametrization describing v, β and C_p[10].

Sound Speed v - In the AcPulse code, the value selected for the sound speed is the nominal value $v = 1500m/s$. This approximation has the purpose of fixing the sampling time in simulation, and therefore the ratio between sampling time in simulated and acquired pulse, simplifying the signal processing on simulated data (Section 3.5). Concerning the signal amplitude, a much more detailed description is required. For this purpose, I consider the empirical parametrization proposed by Wilson [174]. At the level of accuracy here requested, we can take the approximated Wilson formula, as suggested in [175][11]:

$$v = 1449 + 4.6 \cdot T - 0.055 \cdot T^2 + 0.0003 \cdot T^3 + (1.39 - 0.012 \cdot T) \cdot (S - 35) + 0.017 \cdot Z \tag{3.12}$$

Here, T is water temperature, in Celsius degrees; S is water salinity, in psu[12]; Z is depth, in dbars[13].

Thermal Expansion Coefficient β - Concerning the thermal expansion coefficient, a collection of measurements taken at different water temperature is available thanks to Kell [178]. These data have been plotted and an exponential dependence on temperature is found, as in evidence in Figure 3.15. The fit function and the fit parameters are reported in Equation 3.13.

$$y = A_0 + A_1 \cdot (1 - e^{-x/T_1}) + A_2 \cdot (1 - e^{-x/T_2}) \tag{3.13}$$

$$A_0 = -7 \cdot 10^{-5};\ A_1 = 1.5 \cdot 10^{-4};\ A_2 = 1.58 \cdot 10^{-3};\ T_1 = 14.87109;\ T_2 = 182.02178$$

Specif Heat Coefficient C_p - In a similar way, to compute the water specific heat coefficient as a function of water temperature, data taken from a collection provided by Stimson in [179] have been plotted. As illustrated in Figure 3.16, data points are well described by a polynomial curve. Computation has been carried out considering a 2-order, a 4-order and a 6-order polynomial curve and results are compared. The

[10] More information and detailed collections of data are available in [170], in [171], in UNESCO International System of Units in Oceanography [172] and in UNESCO International Oceanographic Tables [173].

[11] Cited in `http://www.cms.udel.edu/mast602/`

[12] psu is Practical Salinity Unit, that is the official scale for salinity since 1978, [176] [177]. It defines the amount of dissolved salts from measures of conductivity. Standard value in sea water is 35; fresh water salinity is approximately 0.

[13] It is common in marine science applications to express pressure in decibars (1 dbar = 0.1 bar). Conventionally, pressure at sea level is taken as the reference value (0 dbars), following the standard formulation introduced in UNESCO technical papers. Increasing pressure corresponds to increasing depth.

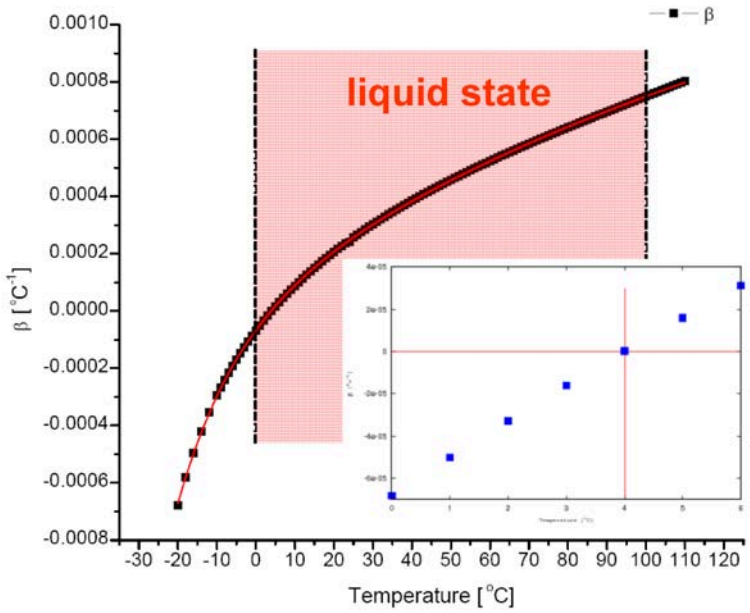

Figure 3.15: Water Thermal Expansion Coefficient of Water as a function of Temperature. Black dots are data point taken from [178]. Red curve is the exponential curve, that well fits experimental measurements. The selected exponential function is: The coloured area evidences the range of temperatures that corresponds to liquid water. It is noticeable that the thermal expansion coefficient is negative if temperature is below 4 °C, as in evidence in the box. Fitting and visualization carried out with Origin (`http://www.originlab.com/`).

6-order polynomial fit has been selected, the fit function and the fit coefficients are given in Equation 3.14.

$$y = \sum_{n=0,\ldots,6} A_n \cdot x^n \tag{3.14}$$

$$A_0 = 4.21721;\ A_1 = -0.00365;\ A_2 = 1.37825 \cdot 10^{-4};\ A_3 = -2.81845 \cdot 10^{-6};$$
$$A_4 = 3.39462 \cdot 10^{-8};\ A_5 = -2.15592 \cdot 10^{-10};\ A_6 = 5.65398 \cdot 10^{-13}$$

To better understand the role of environmental parameters, their contribution has been included on a separate piece of code - Gamma.m - (see Figure 3.13), that is part of the Signal Processing chain (Section 3.5). Parametrizations proposed in this Section for the sound speed, the thermal expansion coefficient and the specif heat value are the ones included in the code to compute the Gruneisen coefficient[14].

Taking into account uncertainties in the measurement of environmental parameters at the ITEP test beam (as pointed out in Section 3.2.2), settings applied in the Gamma.m code are $S = 0$ (fresh water) and $Z = 0$ (sea level). About temperature, several selections have been made in the expected range of values. Investigations on how variations in temperature affect the pressure signal amplitude are discussed in Section 3.6.4.

[14]Concerning the specific heat coefficient, since values from parametrization are in $[J/g \cdot {}^\circ C]$, they have been converted in $[J/kg \cdot {}^\circ C]$.

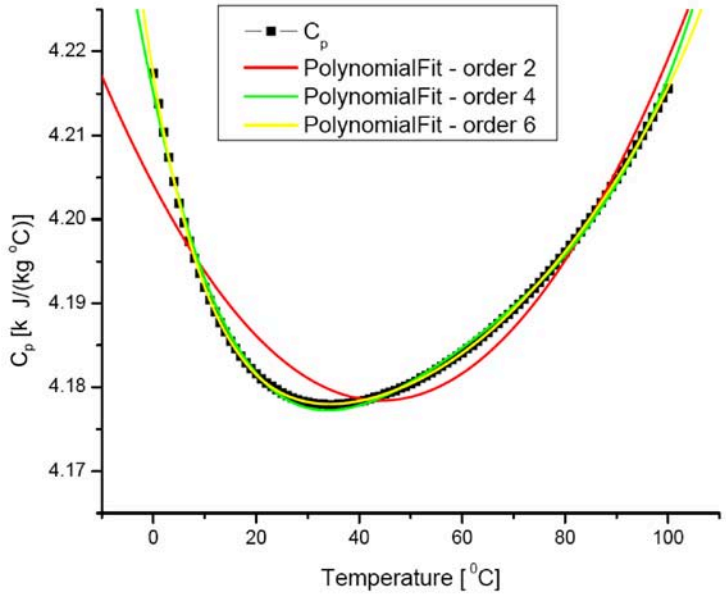

Figure 3.16: Water Specific Heat Coefficient as a function of Temperature. Black dots are data point taken from [179]. In red, green and yellow, the 2-order, 4-order and 6-order polynomial fit, respectively. The last is the solution adopted in the simulation. Fitting and visualization carried out with Origin.

3.5 Signal Processing on Simulated Data

This Section is to give some technical details concerning preliminary data processing applied to pressure signals at the output of the simulation chain.

As already discussed in the previous Section 3.4.3, the code Gamma.m computing the Gruneisen coefficient is included in the signal processing chain, as part of the *scalefactor* computation, that in addition allows to scale the amplitude of the acoustic signal with the number of protons involved in the interaction (see Section 3.7.1).

Beside the *scalefactor*, the most important operation performed on simulated signals is *resampling*. This process increases the number of samples describing the signals and allows a point-to-point comparison with acquired pulses. Coming into details, sampling time for experimental data is $t_{EXP} = 100\,ns$ (Section 3.2.3), while for simulated data it is fixed by the *grid* parameter and the sound speed value, as explained in Section 3.4.2, page 60. Setting in the AcPulse code $grid = 0.3\,cm$ and speed value $v = 1500\,m/s$ (nominal value), one gets $t_{MC} = 2\,\mu s$, that is a ratio $r = \dfrac{t_{EXP}}{t_{MC}} = 20$.

The theory behind the resampling process is *bandlimited interpolation*, ruled by the *Shannon's sampling theorem*. More on this in [180]. It is important to underline that the resampling does not increase the amount of information associated with the simulated pulse, in a sense that the frequency content stays unchanged up to the "true" Nyquist frequency $f_N = 250kHz$, depending on $t_{MC} = 2\,\mu s$.

In addition, in order to get a more accurate comparison between experimental

and simulated data, simulated pulses are filtered, setting the same low-pass filter parameters applied to experimental pulses (Butterworth filter coefficients and cut-off frequency).

Result of data processing on simulated pulse, including the filtering, is shown in Figure 3.17. Scalefactor is not included. Signal processing and visualization is done with Octave.

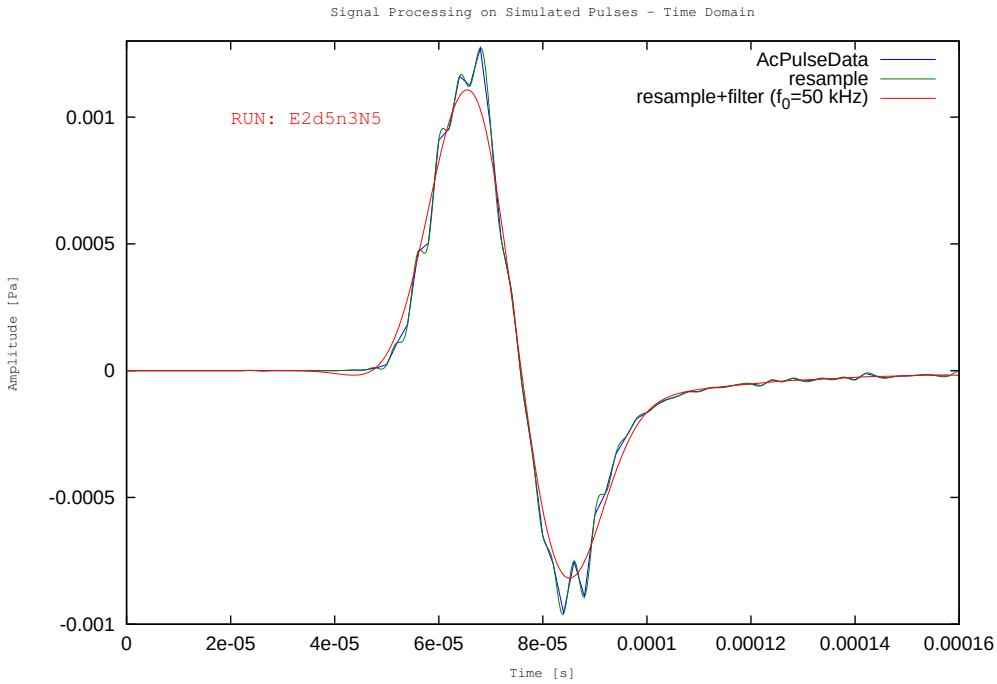

Figure 3.17: Signal Processing on Simulated Data - Time Domain. The plot displays the original AcPulse output, the resampled pulse and the effect of filtering (cut-off frequency = 50 kHz). No scalefactor is considered. Concerning the simulation, the acoustic source is identified by E2d5n3N5: this means that the AcSource code selects injection energy E=200 MeV, collimator diameter d=5 cm, beam profile index n=3 (see Table 3.1), number of primary protons generated N=10^5. Hydrophone is placed at nominal position in AcPulse.

3.6 Investigating the Performances of the Simulation

The last part of this Chapter is dedicated to results of the ITEP test beam simulation. The several aspects pointed out so far (the Bragg peak phenomenon, the beam profile, the geometry of the detection, the temperature dependence) will be examined in details, in order to check if the computation carried out inside the simulation chain is correctly reproducing expectations.

The most important goal of these investigations is in the frame of future developments: a better understanding of the simulation chain and of its parameters implies a deeper comprehension of the physics mechanisms. This improved knowledge can assure a stronger control of the experimental setup in future test-beam experiments. In addition, a robust and verified Monte Carlo can provide a valid starting point to build reliable predictions in the neutrino-case.

3.6.1 The Energy Deposition Profile and the Bragg Peak

This first test on the Monte Carlo can be performed without the coupling with the AcPulse code. The goal is to check that the AcSource simulation reproduces the proton energy deposition profile as expected according to the Bragg peak description (Section 3.1).

Manipulations on *rhoEmap* file, output of the Geant4 ITEP project (Section A.6), can provide several descriptions to visualize how the Geant4 Monte Carlo computes the proton energy deposition in the water tank. For example, Figure 3.18 is the energy deposition longitudinal profile. The plot is produced considering the average per proton of the amount of deposited energy. The Bragg peak is well in evidence, and its position is where expected, according to Equation 3.2.

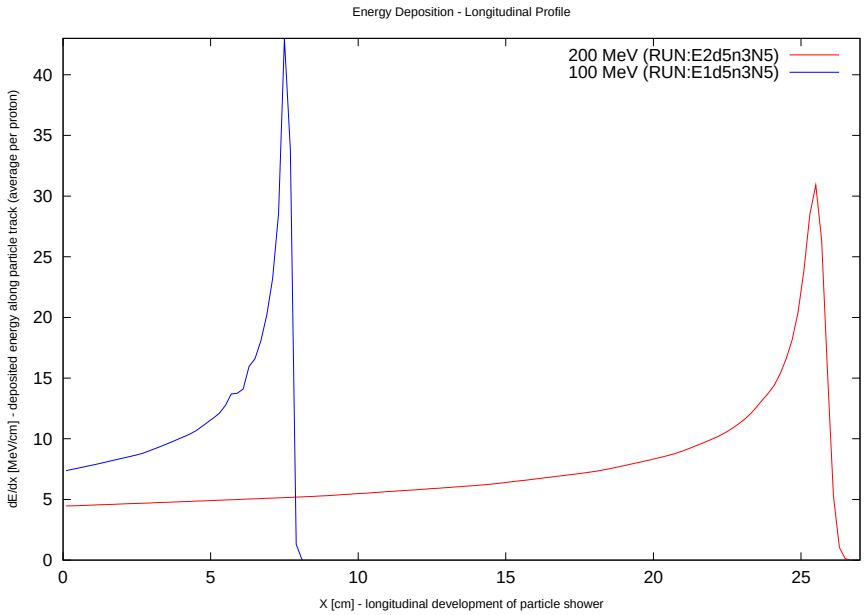

Figure 3.18: Energy Deposition - Longitudinal Profile. The plot displays the shape of energy deposition along the shower longitudinal development. The horizontal axis is the x coordinate of the sensitive cell where energy deposition occurs. The value has been translated so that the origin is at the injection point of particles in the water tank, in order to make it significant in terms of proton range. Vertical axis is the total amount of energy released at range x divided the number of protons involved in the simulation, to get an average per proton. The value is given in [MeV/cm] to underline the energy loss along the track. Considering the selected acoustic source (E1d5n3N5 and E2d5n3N5, details in Figure 3.17, caption), one gets, for E = 100 MeV, maxdose = 6.4457 MeV, range = 7.5 cm; for E=200 MeV, maxdose = 4.6376 MeV, range = 25.500 cm. Results are well in agreement with expectation according to the Bragg peak simplified model, Section 3.1.1.

3.6.2 Beam Profile Dependence

Once that the AcSource code output has been validated, the next step is to understand how different selections in the Monte Carlo of the acoustic source affect the acoustic pulse resulting from the AcPulse code.

The most important set of parameters to consider is connected with the definition of the beam profile at the primary generator, as explained in Section A.4. Beam profile settings are specified in the ITEP.mac macro file (page 121).

A quantitative description showing the connection between the acoustic source size and the pressure pulse shape is pointed out by Askaryan in [133]:

$$f_{eff} = \frac{v}{2 \cdot \ell} \tag{3.15}$$

where f_{eff} is the effective range of the acoustic pulse spectrum[15], v is the sound speed, ℓ is the transverse dimension of the acoustic source. The ℓ parameter is connected with the shape and extension in space of the proton energy deposition, depending on the kinematics of proton injection, and therefore on beam profile settings.

Several investigation have been carried out to study the effect of the beam profile model on the acoustic pulse shape. Examples in the following consider injection energy E = 200 meV, collimator diameter d = 5 cm, number of injected protons N = 10^5 (selection E2d5N5). It is important to underline once again the N is the number of protons generated in the simulation, analogous to the proton intensity measured with the BCT during the ITEP test beam experiment (see Section 3.2.3, page 51). Therefore, it does not equate with the number of protons interacting in water, since there is a certain amount of particles intercepting the lead screen and being stopped before entering the water tank. The number of "escaping" particles is, of course, strongly dependent on the beam profile setting n (σ_1, σ_2, p), together with the collimator diameter selection d.

Results shown in the next are obtained keeping fixed the collimator window diameter and varying σ_1, σ_2, p in the primary generator. Computing the acoustic pulse, the receiver is placed at the nominal hydrophone position.

Figure 3.19 (time domain) and Figure 3.20 (frequency domain) compare signals generated from acoustic sources with different beam profile settings. Table 3.1 gives the complete list of settings implemented for the analysis.

n	σ_1 **[cm]**	σ_2 **[cm]**	p **[%]**
1	0.55	2.0	65
2	1.0	2.0	40
3	1.0	2.0	50
4	0.55	2.0	40
5	0.80	2.0	40
6	0.80	2.0	30

Table 3.1: Beam Profile Settings.

Results are consistent with Askaryan prediction (Equation 3.15). A narrow beam ($n = 1$) implies that particles travel close to each other, and deposit their energy

[15]The term "effective" refers to the fact that the computation has been developed assuming a "monochromatic" pulse, radiating at a single frequency. The actual pressure pulse contains a broad band of frequencies centered at about f_{eff}. Additional details in [152].

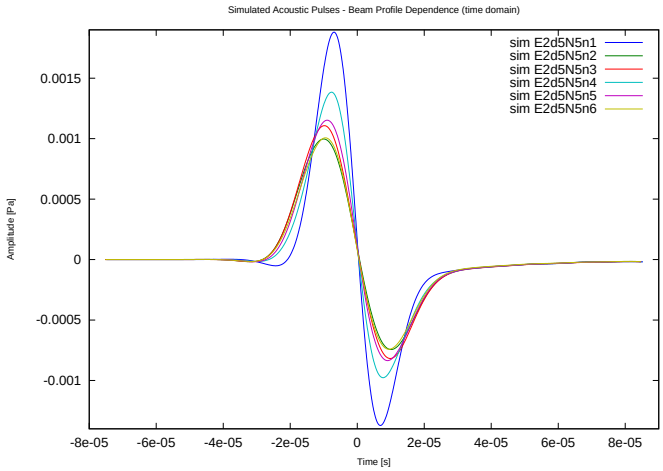

Figure 3.19: Acoustic Pulse dependence on Beam Profile Settings - Time Domain. Results follow the prediction of Equation 3.15 concerning the connection between the acoustic source size and the acoustic pulse spectrum. Time origin is placed at the pulse centre $t_0 = [t(A_{min}) + t(A_{max})/2]$(see parametrization introduced in Section 3.6.3). Signal processing is applied, as described in Section 3.5.

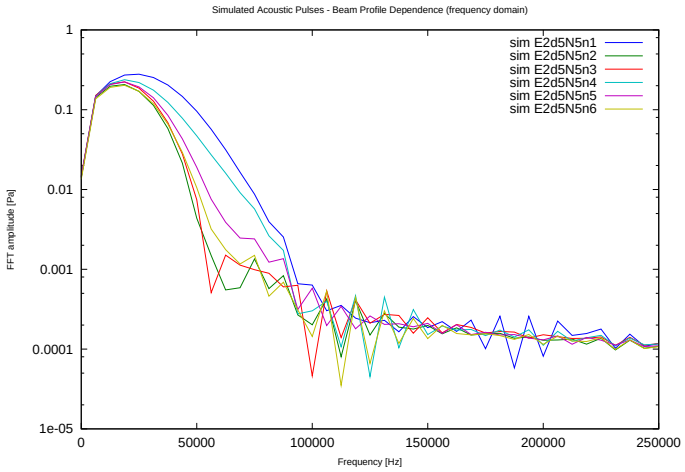

Figure 3.20: Acoustic Pulse dependence on Beam Profile Settings - Frequency Domain. The frequency scale is displayed up to the "true" Nyquist frequency of simulated pulse

over a restricted region in the water volume. Therefore, the transverse size of the acoustic source is small, and the acoustic signal has a broad frequency content (large f_{eff}) and a fast evolution in the time domain (the sound transit time across the source transverse size is short). On the contrary, a wider beam ($n = 3$) is consistent with a more diffuse distribution of tracks in the water tank, with energy deposition spreading over a larger volume (larger transverse size ℓ). The consequence is that the corresponding signal is shorter in the frequency domain and longer in the time domain. A more quantitative approach is discussed in Section 3.29, Figure 3.30.

In addition, in the narrow beam case the energy density is larger: the volume of deposition is smaller, and the total amount of energy released in the water tank

increases because much more particles are allowed to pass through the collimator window. Since according to the thermo-acoustic mechanism the pressure perturbation is related to the energy density (Section 2.1), this explains the behaviour of the signal amplitude, that has a maximum with beam profile settings identified by $n = 1$. For additional details on this topic, see Figure 3.31 in Section 3.7.2.

A better comparison among different beam profile models is achieved considering a normalized amplitude. Results are plotted in Figure 3.21.

Superimposing the experimental acquisition (RUN: E2d5), represented by the black thick line, it is possible to get an indication on the actual beam profile during the ITEP test beam. A clearer guide comes from looking at signals in the frequency domain, Figure 3.21 (b).

The study developed in this Section allows to discriminate among different models of beam profile. A too narrow description can be excluded. On the contrary, a guess can be made in favor of a "wide" beam. Considering "wide" models, results are less sensitive to details in the beam profile settings (σ_1, σ_2, p). The set of parameters identified with $n = 3$ has been selected for further analysis[16].

3.6.3 Hydrophone Position Dependence

Investigations on beam profile allow to have an indication concerning the primary generator setting. Still, considering the plot shown in Figure 3.21 (a), there is some difference in the pulse shape between experimental data and simulation, that cannot be easily eliminated introducing additional correction in beam profile parameters. The difference is in fact mostly a matter of asymmetry, since the rarefaction (negative) peak is smaller that the compression (positive) peak, and the disparity is much more pronounced in acquired data, than in simulated ones.

Asymmetry of the acoustic pulse is connected with the *geometry of the detection*, that is where the hydrophone is placed with respect to the acoustic source. According to the description given in Section 3.4.2, the energy deposition profile, and therefore the acoustic pulse itself, appears different to different receivers placed in different positions. Therefore, the geometry of the detection plays a major role in affecting the result of the simulation.

Looking at Figure 3.21 (a) and keeping in mind these considerations on connection between asymmetry and geometry, since simulated pulses are computed setting hydrophone coordinates to the nominal values ($xH = -21.75cm$, $yH = 10.5cm$, $zH = 0.0cm$ for the case E = 200 MeV in the AcPulse code), the conclusion is that they do not indicate the "true" location of the receiver during the ITEP data acquisition, and some corrections are required.

To have an indication on the corrections to apply to nominal hydrophone position, the next step consists thus in computing the acoustic pulse, changing the hydrophone coordinate values (xH, yH, zH) in the AcPulse code. The AcSource configuration is the same for every computation (E2d5n3N5); the *scalefcator* is not included.

The first approach to the problem is carried on with yH fixed at the nominal value, and "pushing" the receiver forward or backward along the x axis, in order to

[16] Additional investigations have shown that results obtained with $n = 3$ are about equivalent to a single Gaussian model ($p = 100$), with $\sigma_1 = \sigma_2 = \sigma = 1.5\,cm$.

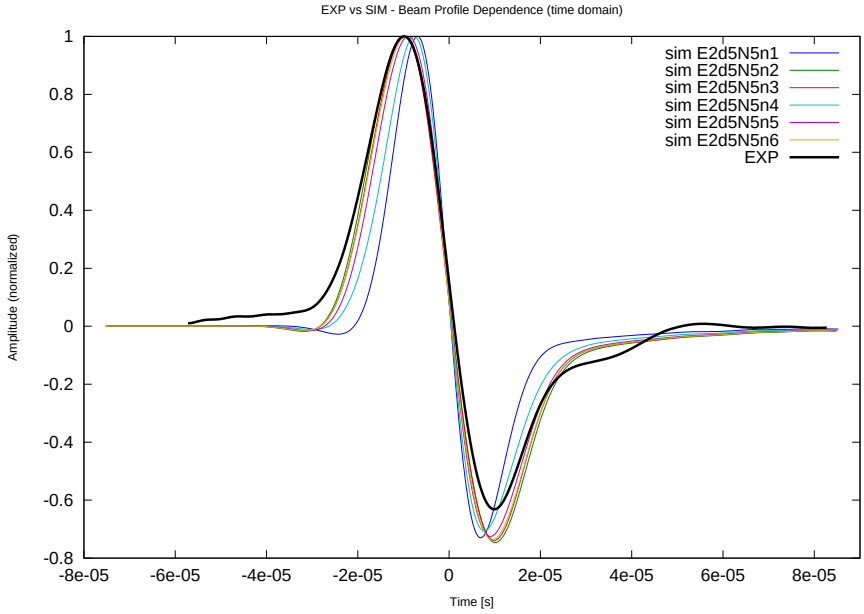

(a) Acoustic Pulse dependence on Beam Profile Settings (time domain) - normalized scale

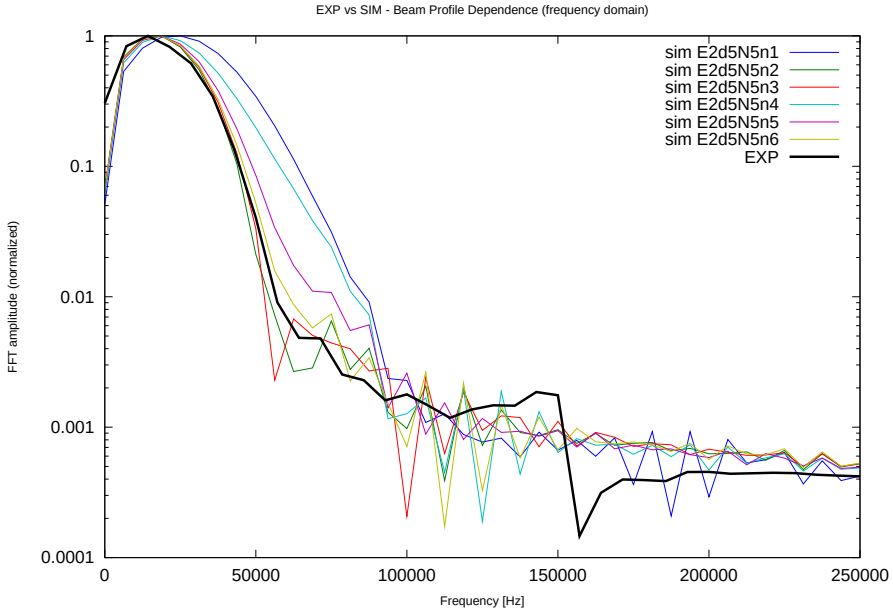

(b) Acoustic Pulse dependence on Beam Profile Settings (frequency domain) - normalized scale

Figure 3.21: Acoustic Pulse dependence on Beam Profile Settings - normalized scale. Signals in Figure 3.19 and Figure 3.20 are displayed on a normalized amplitude scale; the experimental pulse (RUN: E2d5) is added.

explore different "points of listening" to the Bragg peak. Results in the time domain are included in Figure 3.22, details in caption.

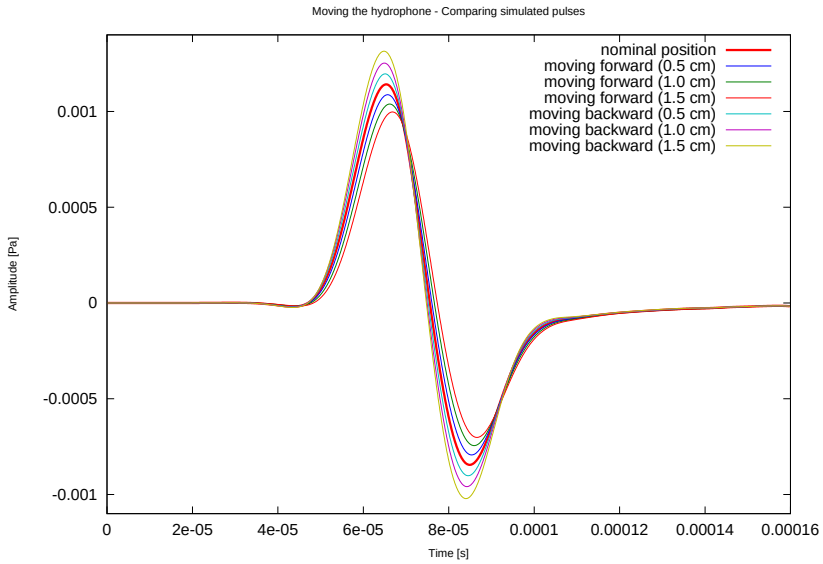

Figure 3.22: Signal dependence on hydrophone position. The acoustic pulse computed with hydrophone in the nominal position is represented by the thick red line in the plot. Starting from this position, the hydrophone is moved back and forth, with step of 0.5 cm along the x direction. Variation in the signal amplitude is due to the fact that the distance between the acoustic source and the receiver changes with hydrophone coordinates. Increasing distance corresponds to decreasing amplitude, and moving forward means getting farther from the energy deposition (remember there is something before the Bragg peak, but almost nothing beyond). Changes in distance affect also the time of arrival of signal to the hydrophone.

A more quantitative approach can be reached considering the Niess-Bertin parameterization, introduced in [131] to give a quantitative description of the shape of the pressure pulse using a small number of values. As in evidence in Figure 3.23, the pulse shape in the time domain can be characterized by 3 parameters: peak to peak duration Δt, half peak to peak amplitude A_p, symmetry factor R/C, that is the ratio of the amplitude of the rarefaction peak to the compression one.

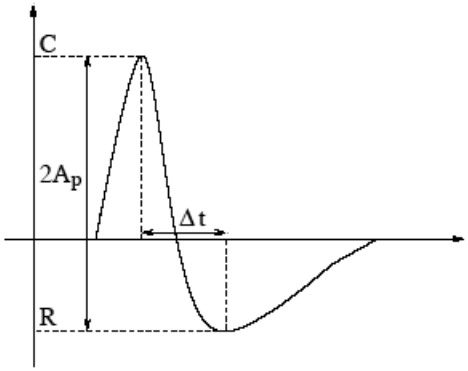

Figure 3.23: Niess-Bertin Parameters [131].

In this Section, Niess-Bertin parameters are used to quantify the differences in the shape of acoustic signals as a function of the hydrophone position. Figure 3.24 report results for the symmetry factor R/C, including different simulations and the experimental case RUN: E2d5. The goal is to get an indication on where to place the hydrophone in the simulation to approach the experimental value. Results show a clear tendency in favor of the "forward movement". Assuming a linear dependence between the symmetry factor and the shift in the x direction, the prediction is that a better agreement with experimental data could be reached "pushing" the hydrophone forward, at about 4.5 cm from the nominal position. Details in Figure 3.25, caption.

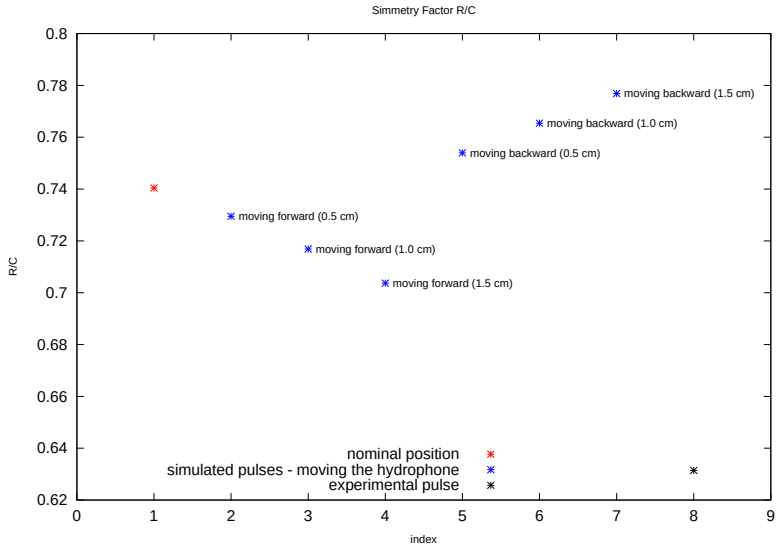

Figure 3.24: Symmetry Factor R/C as a function of Hydrophone Position. The horizontal axis is an index identifying the geometry of the detection: index=1 (red dot) is the result of computation at the nominal hydrophone position; index=8 (black dot) is the symmetry factor for the experimental acquisition; index=2-4 correspond to hydrophone moving forward, index=5-7 represent computation with hydrophone moving backward. The goal is to get an indication on where to move the hydrophone to approach the experimental value of symmetry factor.

Figure 3.26 drives a comparison, on a normalized scale (time domain and frequency domain), between the experimental pulse (RUN: E2d5) and the output of the simulation, the latter computed with hydrophone shifted from nominal position considering the outcome from Figure 3.25. It is in evidence that a better agreement concerning the symmetry factor has been achieved.

3.6.4 Temperature Dependence

Considerations carried on up to now have been developed taking into account normalized amplitude signals. Therefore, before going on with the final comparison between experiment and simulation (Section 3.7.1), the last topic to investigate concerns the signal amplitude.

As already widely discussed, environmental parameters, and temperature in par-

ticular, strongly affect the signal amplitude, since they determine the value of the Gruneisen coefficient (Section 3.4.3). Figure 3.27 shows the effect of water temperature on the acoustic signal amplitude. Results are produced varying temperature values in the range [3.0 - 20.0] °C, with a step of 1.0 °C. It is interesting to notice that, with temperature spanning in the specified interval, the signal amplitude covers almost two order of magnitude.

3.7 ITEP Test Beam - Results

Investigations on the performances of the simulation, developed and discussed in Section 3.6, have two main intentions. The first one is to deeper understand the phenomenon of thermo-acoustic pulse generation. The second is that Monte Carlo studies allow to enrich and complete the data analysis.

As widely underlined in Section 3.2, several uncertainties affect the data taking. Outcomes achieved in Section 3.6 give strong indications to solve undetermined parameters. For instance, Section 3.6.2 produces some hints on the beam profile settings and Section 3.6.3 answers the question about the geometry of the detection. In other words, once that the Monte Carlo has been validated, it can work as an additional tool for data analysis on ITEP test beam acquisitions, providing extra clues to interpret the results.

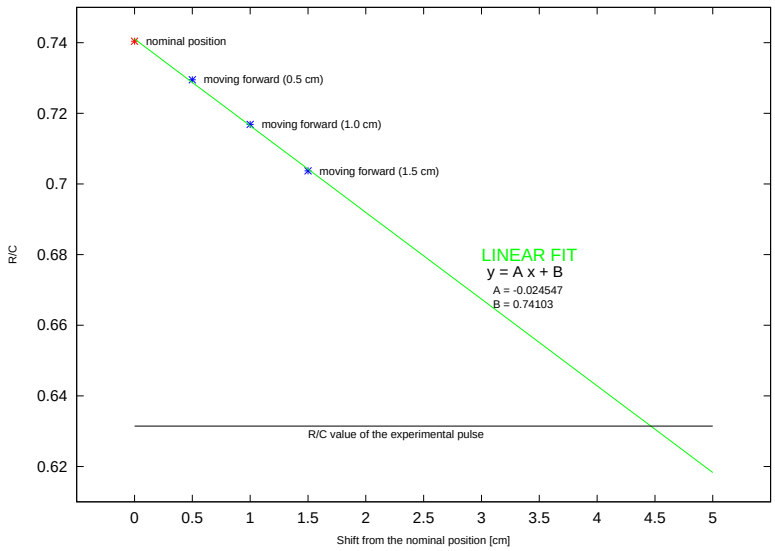

Figure 3.25: Symmetry Factor R/C and the shift in the x coordinate - Linear dependence. The horizontal axis is the shift of the hydrophone x coordinate from the nominal position. Dots in the plot are data (1-4) from Figure 3.24 (nominal position and moving forward results). The green line is the result of a linear fit on data (1-4). The black line gives the level of asymmetry of the experimental pulse. The intersection of the black line with the green line gives the prediction on the shift to apply in xH.

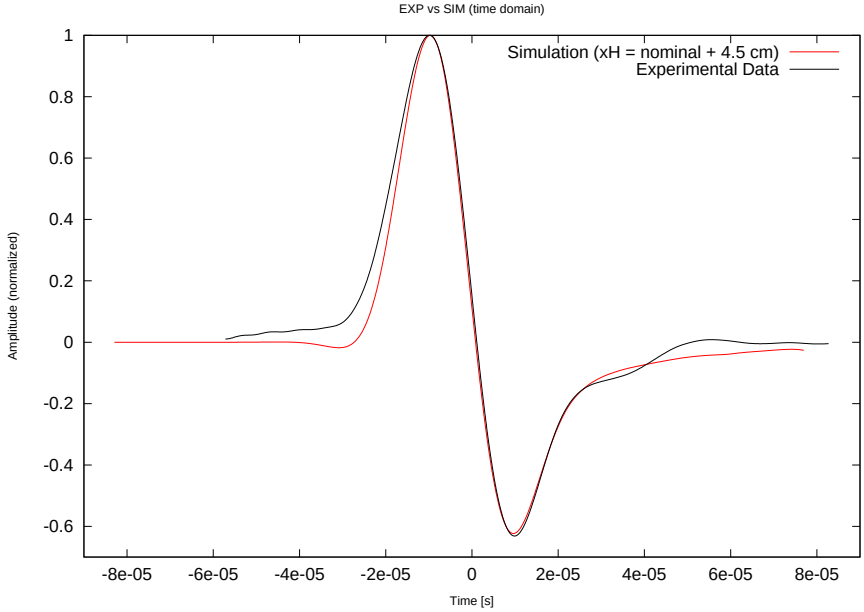

(a) Comparison between experimental data and simulation (time domain)

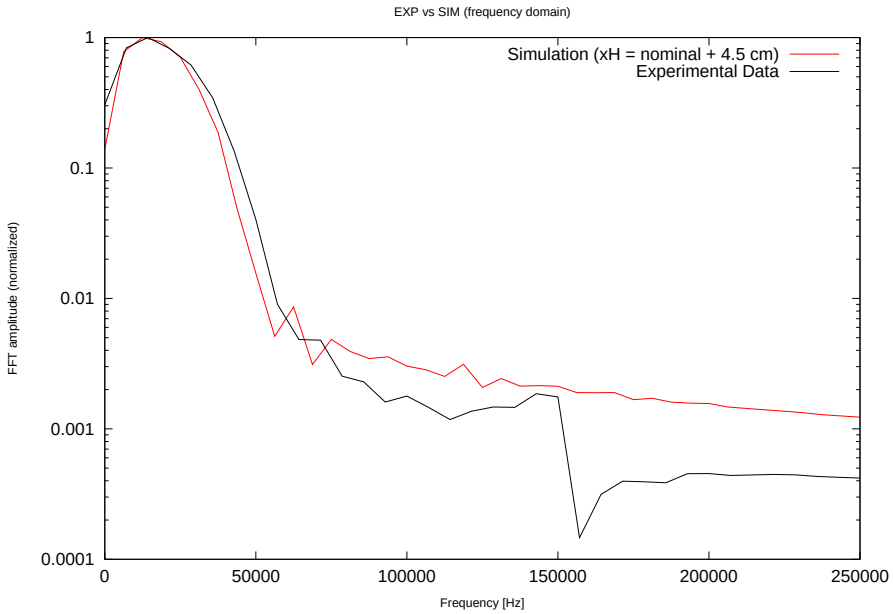

(b) Comparison between experimental data and simulation (frequency domain)

Figure 3.26: Comparison between experimental data and simulation. Hydrophone position in the AcPulse code is set considering the shift resulting from Figure 3.25.

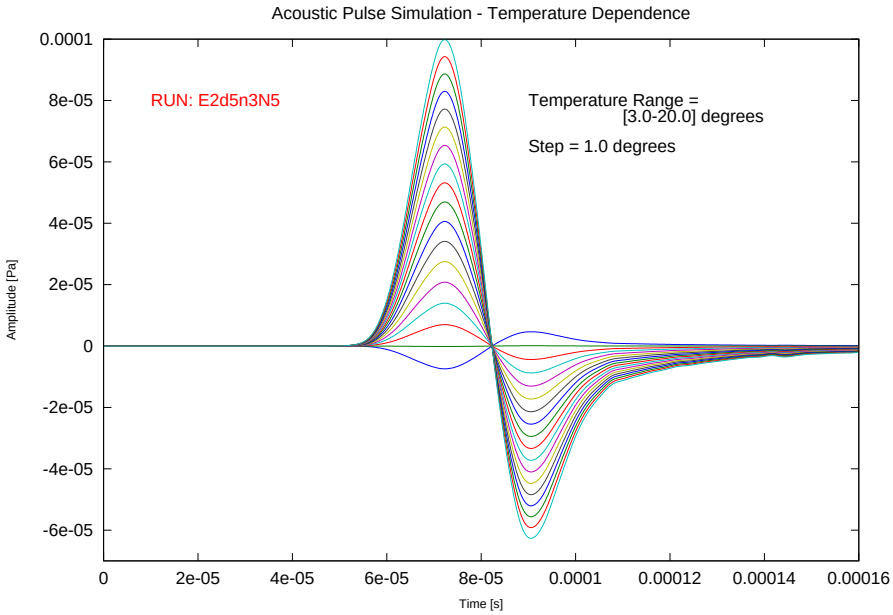

Figure 3.27: Signal Amplitude dependence on Water Temperature. It is in evidence the effect of negative thermal expansion coefficient, occurring if water temperature is below 4 °C. The consequence is that acoustic pulse at low temperature is inverted, that means that first a rarefaction and then a compression occurs.

3.7.1 The Best Data/Simulation Comparison

The first result coming from the joint effort in simulation and data analysis is the "best" comparison between experimental data and Monte Carlo simulation. The comparison carried on up to now (Figure 3.26) is completed including a *scalefactor* depending both on environmental parameters (Gamma.m code) and on the ratio between the number of protons in the experiment (BCT measurement, Section 3.2.3 and in the simulation. The most important outcome from the study on the *scalefactor* is that it closes the set of information one can extract from the simulation, offering a good indication for the temperature value during the data taking. The "best" value appears to be $T = 15.8\,°C$, results shown in Figure 3.28[17].

An additional important point resulting from Figure 3.28 is the order of magnitude of the acoustic pulse. The good agreement between experimental data and Monte Carlo simulation offers a confirmation on the measured value.

The last note is on the time of arrival. The time scale in Figure 3.28 has its origin at the time of proton injection in the water tank. The positive peak appears on the hydrophone after about $7 \cdot 10^{-5}\,s$. Assuming instantaneous energy deposition, that is the spill time is much more shorter than the transit time across the source

[17] For completeness' sake, it must be added that the simulated pulse included in Figure 3.28 is not exactly the same shown in Figure 3.26. The simulation is computed setting $xH = -17.25\,cm$ (the nominal position and a shift of $4.5\,cm$), $yH = 9.5\,cm$ (a correction of $1.0\,cm$ on nominal position), $zH = 0.0\,cm$). The idea is to keep unchanging the distance between the receiver and the core of the energy deposition (the Bragg peak, assumed at $xBP = -21.75\,cm$, $yBP = zBP = 0.0\,cm$ in the water tank frame of reference), in order to get the same time of arrival in acquisition and simulation (time is connected to distance through Equation 3.5).

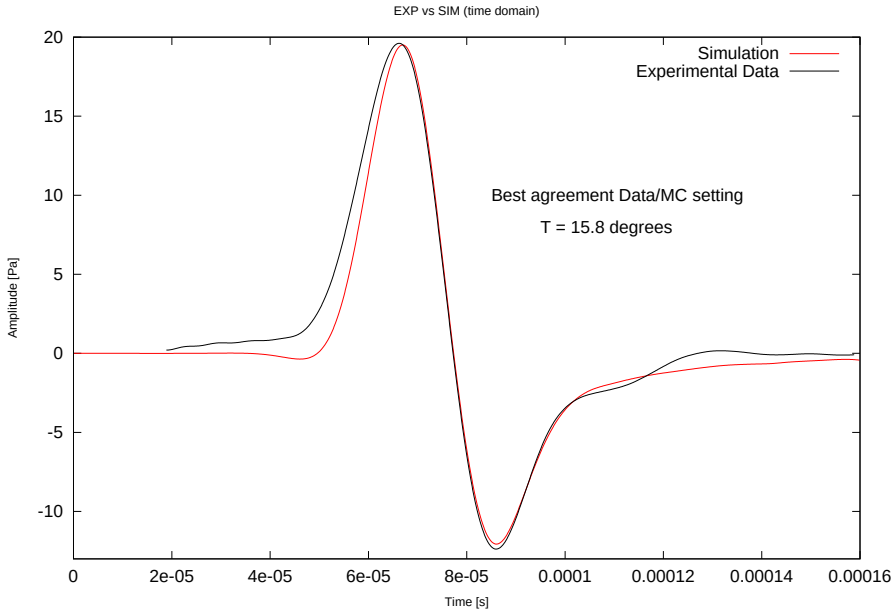

Figure 3.28: Best comparison between experimental data and simulation. Results obtained right now considering the outcomes from investigations on the simulation are integrated including the *scalefactor*, that is temperature dependent. The best agreement is reached selecting $T = 15.8\,°C$. The value is compatible with expectations, according to information available during the data taking. Origin of time is at the proton injection in the water tank.

diameter, the observed time of arrival corresponds to a distance between the source and the receiver of about $R \approx 10.5\,cm$ (Equation 3.5), compatible with the assumed geometry of the detection.

3.7.2 Comparison with Sulak Results

So far so good, results of the ITEP test beam seems to be well consistent with predictions of the simulation, and experimental data can be described and interpreted in the frame of the thermo-acoustic mechanism.

The next step consists in looking for validation somewhere else, moving apart from my ITEP test beam data set. The choice goes on the already mentioned Sulak *et al.* studies in the field of experimental check out of the thermo-acoustic mechanism [152].

The cited paper (in the following, referred to as "Sulak paper") accounts on deep investigations with proton beams. Two independent data set (in the following, referred to as "Sulak data") have been collected, exploiting features of two different accelerator facilities (Brookhaven National Laboratory - BNL and Harward University) and considering two different experimental setup and geometry of acquisition. The first experiment was performed at BNL linear accelerator, with 200 MeV protons interacting in a large water tank. Number of protons in the particle beam is such that the total deposited energy is in the range $10^{19} - 10^{21}$ eV. The distance between the hydrophones and the beam is set at $1\,m$.
A low-energy set (less intense proton beams, for a total deposited energy in the

range $10^{15} - 10^{16}\, eV$) has been collected at the 158 MeV cyclotron at Harward, with hydrophones positioned 8 cm off the beam axis, opposite the Bragg peak.

It is interesting to notice that Sulak data are affected by the same kind of uncertainties that accompany my data set collected at ITEP (Section 3.2). In particular, in [152] they refer to uncertainties in the measurement of the beam intensity and in the calibration of the transducers.

During the data taking, Sulak and his collaborators had control on the spill time, and they could verify that, under the assumption of instantaneous energy deposition (spill time shorter than sound transit time across the source transverse size), the signal amplitude was linearly related to the total energy deposited in the water tank. My intention is thus to check if data collected during the ITEP test beam follow the same tendency of Sulak results.

The procedure to perform the comparison consists in extracting data from figures included in the Sulak paper, both the low-energy and the high-energy set. Sulak data are converted in order to have energy in eV and pressure in Pascal.

Concerning the results from the ITEP test beam, for each run listed in note 4 the total deposited energy is computed from the Monte Carlo. Going into details, the computation consists in considering the output of the Geant4 AcSource code with beam profile settings following the indications in Section 3.6.2, note 16. Total deposited energy is the total amount of energy released in the sensitive volume. The value is scaled taking into account the ratio between number of protons in the experiment (BCT measurement) and number of protons in the simulation ($N = 10^5$). An estimate of the error is computed considering a "lower" ($\sigma = 1.0cm$) and an "upper" ($\sigma = 2.0cm$) beam profile model. The signal amplitude is the A_p parameter computed according to Niess-Bertin definition (Figure 3.23). In this case, an estimate of the uncertainty is evaluated considering the signal processing. The adopted strategy is to apply a second order Butterworth filter with cut-off frequency $f_0 = 100\, kHz$ and consider a "lower" ($f_0 = 50\, kHz$) and an "upper" ($f_0 = 100\, kHz$) case, to set the error bars.

Figure 3.29 displays Sulak linearity results, presenting on the same plot both the low-energy set and the high-energy. Results from the ITEP test beam are added. Since data span over several orders of magnitudes both in energy and in pressure amplitude, they are represented on a logarithmic scale. Details in caption.

Beside the fact that the three data set refer to very different experimental setup, and that data analysis has been carried out independently and according to separate strategies[18], the comparison shown in Figure 3.29 is successful. In fact, not only it verifies what stated in the Sulak paper: the low-energy set is consistent with a linear extrapolation of the high-energy set. In addition, it shows that the ITEP results perfectly follow the same trend and data stay in the "right" place, filling the empty region between the low-energy and the high-energy set.

The detailed study of the linearity of the signal amplitude with total deposited energy is only one of the several aspects that the Sulak paper investigates in depth.

[18] Technical details on Sulak data analysis are not known. Sulak paper refers to some corrections applied, concerning the beam spill time, the beam radius, the deposition length and distance between acoustic source and hydrophone.

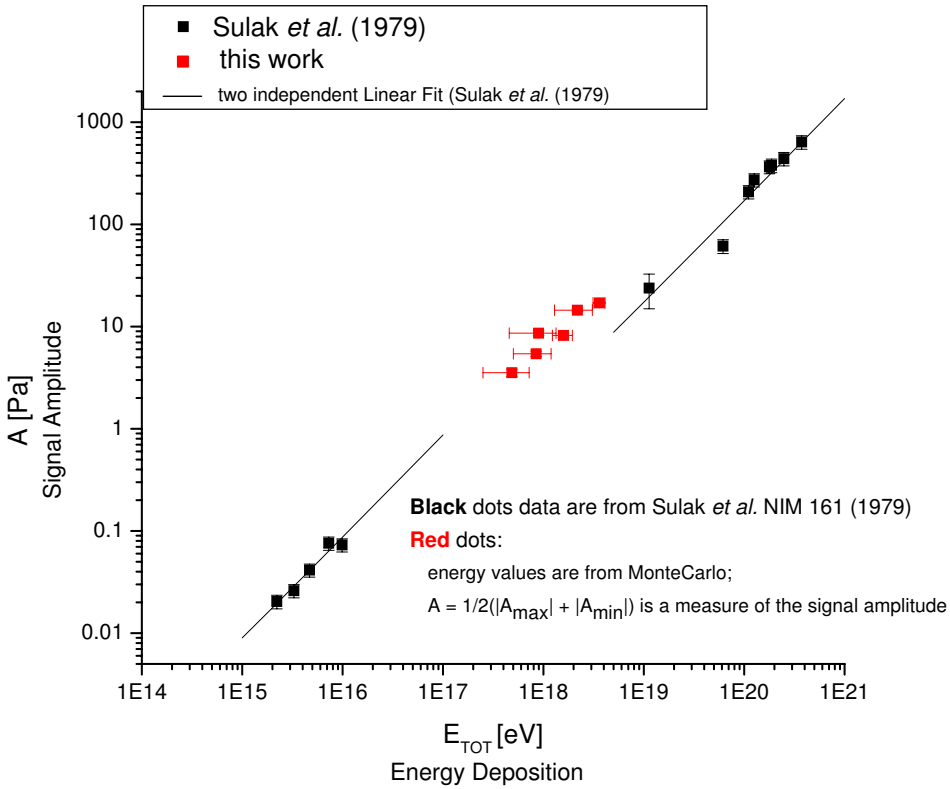

Figure 3.29: Linearity of the signal amplitude with the total deposited energy - ITEP and Sulak data. Sulak data are from two independent experiments performed with proton beams; black lines are the outcome of two independent analysis and linear fit computation. Red dots are ITEP data. The plot is on logarithmic scale. Considering the three data sets, an important difference concerns the hydrophone's position during data acquisition: low-energy data have been collected with hydrophone positioned 8 cm off the beam axis; high-energy data were acquired setting the source-receiver distance at 1 m; the hydrophone position in the ITEP case is at about 10.5 cm from the shower core. The consequence of this difference in the geometry of the detection is in evidence. Since the signal amplitude scales with the distance between the acoustic source and the receiver, this explains why the high-energy data set, collected at larger distance, lies on a lower line.

Among the other topics the paper faces and illustrates, there are: signal period versus beam diameter, signal amplitude versus beam diameter, signal amplitude versus temperature, signal amplitude versus distance between source and receiver. These investigations aim to prove that thermo-acoustic mechanism of sound generation is dominant over alternative mechanisms, such microbubbles and cavitation[19]. Experimental results are well supported by the simulation, computed assuming the thermo-acoustic hypothesis, and offering a validation of the model it self.

Because of the limited amount of experimental data collected at ITEP, and the little control on machine settings, geometry and environmental parameters, comparison between Sulak and ITEP experiment cannot go much further that the check of the linearity trend.

[19] Information on cavitation and bubble dynamics can be looked up in [181].

Nevertheless, Sulak results can still be considered a fruitful source of information, in particular they offer a valid tool of comparison to perform additional test of the simulation chain. Moreover, since the ITEP simulation is based on the thermo-acoustic hypothesis and since it well describes the outcome of the ITEP experiment 3.7.1, if the Monte Carlo shows agreement with Sulak results, this constitutes a further confirmation of the thermo-acoustic model at the ITEP test beam.

A first investigation can be dedicated to explore the relation between the signal period τ (duration of the acoustic pulse in the time domain) and the beam diameter D. The account given in the Sulak paper, based on Equation 3.15, adopts the naive description according to which the half period of the bipolar pulse is connected with the transit time across the beam diameter, through the relation:

$$\tau = \frac{2 \cdot D}{v} \tag{3.16}$$

(the beam diameter is related with the source transverse dimension ℓ). The signal period is independent of the beam energy and intensity.
Controlling the beam diameter, Sulak and his collaborators could plot the signal period versus the beam diameter, and check the validity of the prediction.

To compare with Sulak results, I consider the acoustic pulses investigated in Section 3.6.2 (Figure 3.19). For each event, I take as the beam diameter the weighted mean of the σ parameters listed in Table 3.1, $D = [p \cdot \sigma_1 + (1-p) \cdot \sigma_2]/100$. I assume the signal period as $\tau = 2.25 \cdot \Delta t$, where Δt is the Niess-Bertin parameter (Figure 3.23)[20]. The error bar is the ten percent of the value, considering the uncertainty in the definition of the pulse duration.

Sulak results and the outcome of the ITEP Monte Carlo are plotted in Figure 3.30. The trend is consistent with the prediction, and the agreement with the model is quite good.

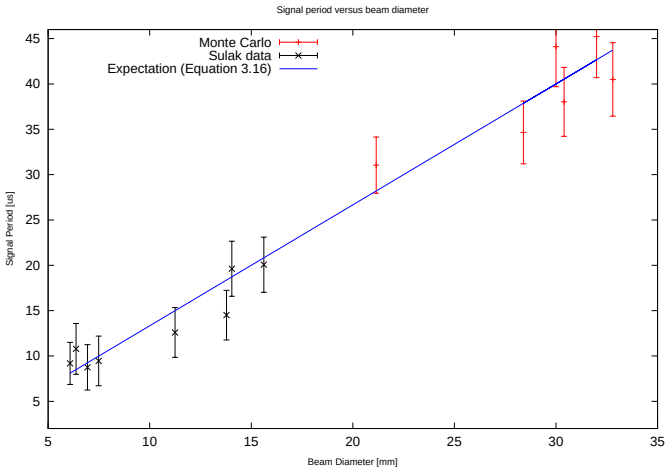

Figure 3.30: Signal Period versus Beam diameter. Sulak data (black dots) are taken from Sulak paper [152]. Red dots are the outcome of the ITEP Monte Carlo. The blue line is the expectation, according to Equation. 3.16.

[20] Δt is approximately the half period. The correction $0.25 \cdot \Delta t$ accounts for the "tails" in the pulse shape.

An additional check can be performed considering signal amplitude. Sulak paper refers to Askaryan computation, assuming signal amplitude proportional to f^2, and therefore the following relation with the beam diameter D:

$$A \propto \frac{1}{D^2} \tag{3.17}$$

Figure 3.31 displays results of the ITEP simulation, obtained choosing for the signal amplitude the value at the positive peak. The error bar is the ten percent of the value, to take into account any uncertainty in the model and fluctuations in the peak amplitude due to the asymmetry of the bipolar pulse. The plot shows that the outcome of the ITEP Monte Carlo follows the prediction.

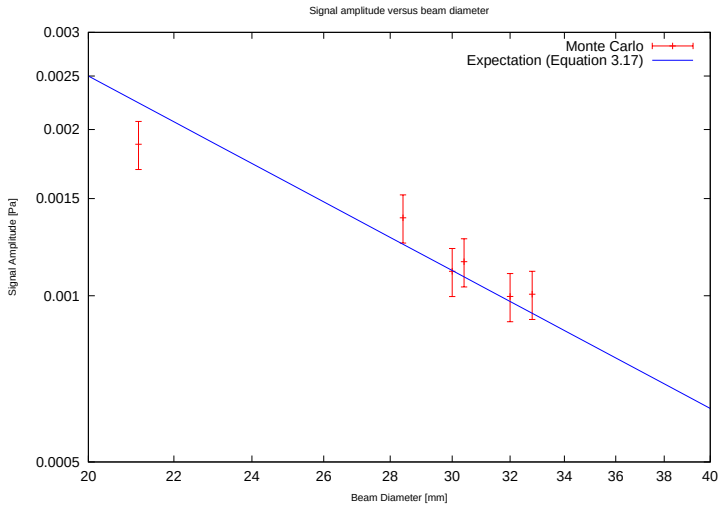

Figure 3.31: Signal Amplitude versus Beam Diameter. Outcome of the ITEP Monte Carlo is compared with expectation, that assumes a $1/D^2$ dependence of the signal amplitude on the beam diameter D. The plot is represented in logarithmic scale. Since Sulak results in [152] are given in arbitrary units, they cannot be compared on the same plot with the ITEP simulation.

3.8 Conclusions

The discussion presented in this Chapter can be considered a conclusive account on the ITEP test beam experiment. A schematic list of the most noticeable results of the study are:

1. The outcome of the Geant4 Monte Carlo well reproduces the expectations concerning the energy deposition profile of protons in water. In particular, the Bragg peak behaviour is simulated according to the model (Section 3.6.1)

2. Combining outcomes from data analysis and Monte Carlo simulation, it is possible to have indications on some acquisition parameters that can confirm and enrich the knowledge of the experimental setup. In particular, the beam profile model is discussed in Section 3.6.2, the geometry of the detection in Section 3.6.3, the Gruneisen coefficient in Section 3.7.1.

3. ITEP experimental data set is in good agreement with Sulak data concerning linearity between the signal amplitude and the total deposited energy (Section 3.7.2). In addition, results shown in Figure 3.29 give the order of magnitude of expected acoustic signals generated from proton induced showers in water.

4. The development of the Monte Carlo has given the opportunity to progress in the understanding of the thermo-acoustic mechanism. Several aspects of the model are well described and their effect on the pressure pulse generation is under control.

5. Additional validation of the simulation chain developed for the ITEP project comes from the agreement with Sulak well established results in the frame of the thermo-acoustic hypothesis (Section 3.7.2).

Item 4 in the above list is important for planning future experiments to perform calibration measurements with test beams. A mandatory recommendation for the future is to include a strict control on environmental parameters and geometry. The successful comparison with Sulak results (item 5 in the list) indicates that the simulation chain, developed for proton induced showers in the frame of the ITEP test beam experiment, is well adequate to describe the thermo-acoustic phenomenon of pressure pulse generation. This conclusion thus assures that the Monte Carlo can be applied as a valid tool to explore the neutrino case, as it will be discussed in the next Chapter.

Chapter 4

Acoustic Signal from Neutrino-induced Hadronic Showers

4.1 From Protons to Neutrinos

Achievements reached with the ITEP proton beam test, diffusely described in Chapter 3, can be taken as a starting point for future developments. In particular, successful comparison with Sulak data represents an additional confirmation of the thermo-acoustic mechanism as the main responsible for the pressure pulse generation. At the same time, since results have been achieved with the support of a dedicated simulation (AcSource and AcPulse), they validate our understanding and our description of the mechanism itself. Work done with protons, both in simulation and in data analysis, has thus provided tools and techniques to extend the study of the acoustic signal to the neutrino-case.

Concerning neutrinos, since experimental data are of course not available, the whole topic has to be faced with simulation.

As already widely discussed in Section 3.4, the simulation chain can be described as made up of two elements, referred to as AcSource and AcPulse, the first one dedicated to the reproduction of the acoustic source, the second one devoted to the computation of the acoustic pulse. It is important to underline once again that they constitute two independents steps in the computation procedure, in a sense that they have been devised and written separately, and they can be tested and used independently. AcSource stays upstream, AcPulse stays downstream, and they are connected since output from the former plays the role of input for the latter (see Figure 3.13).

Keeping concentrated on the AcPulse step of the computation, the noticeable point is that the code can be adapted to accept as input any energy deposition, or, in other words, beside minor changes in the code, any energy deposition "map" can "feed" the AcPulse program. Therefore, moving from protons (test-beam) to neutrinos (the relevant case for underwater neutrino telescopes), the most immediate choice is to try the AcPulse program combined with neutrino-related acoustic sources.

4.2 CORSIKA Showers

Results shown in this chapter are obtained feeding AcPulse with energy deposition patterns coming from the simulation of neutrino-induced hadronic showers propagating in water. The tracking of the particles in the shower and the evaluation of their energy losses is computed with a modified version of the CORSIKA code.

CORSIKA (COsmic Ray SImulations for KAscade) [182] is a program for detailed simulation of extensive air showers. The program was originally written to work as the backbone of the simulation system of the KASCADE surface array experiment. It still constitutes a reference for cosmic air experiments, and has been implemented in Auger, as well.

Taking the CORSIKA package as a starting point, people from the ACoRNe Collaboration (Section 2.4) have adapted it to make it suitable for submarine applications. In particular, T. Sloan has modified the code to simulate high-energy showers propagating in water. His efforts are documented in [183]. The major change consists in considering a medium of constant mass density ($\rho = 1.025\, g/cm^3$) instead of the variable density air atmosphere. The modification of the medium density affects the threshold for the LPM effect[1] In addition, since showers transverse development in water is limited if compared to the air case, a smaller radial binning is required.

Thanks to a personal communication with Sloan, I was provided the results of his work, i.e. a simulation code, that plays the role of AcSource, producing *rhoEmap* files to be used as input for the AcPulse program. In the following, I will refer to the output of the CORSIKA AcSource as "CORSIKA Showers".

The ACoRNe Collaboration results in the field, including both the study of the acoustic source (performances of the CORSIKA Showers simulation) and of the acoustic pulse generation, are extensively described in [140]. The material in the cited paper constitutes a term of comparison for the study discussed in this chapter.

4.2.1 CORSIKA AcSource

Going into details of the Monte Carlo simulation of the acoustic source, for each $n_p = log_{10}E_p[GeV]$ ($n_p = 2, ..., 11$), a collection of 100 individual CORSIKA proton induced showers is produced and stored in files. These data files are in the format of an energy "map" in cylindrical coordinates, assigning a couple of values (longitudinal, transverse) to identify the the annular region along the shower axis where the energy is deposited. Therefore, axial symmetry is assumed, the longitudinal index pointing to the penetration depth along the shower axis, the transverse index following the radial development of the particle shower. Longitudinal slices are equally spaced, volume of deposition changes with the radius. In addition, to better describe the transverse energy profile, the binning is computed so that the inner radii are packed more closely.

An ultra-high-energy neutrino propagating in water can interact with nucleons in the medium and generate a particle cascade (Section 1.3.1). The CORSIKA AcSource Monte Carlo is based on the simplified assumption according to which a CORSIKA proton induced shower is equivalent to a neutrino induced hadron shower

[1] LPM threshold depends on medium density: order of magnitude is $10^2\, TeV$ in water, $10^17\, TeV$ in air at standard temperature and pressure [132].

at the same energy. In other words, the CORSIKA shower collection reproduces the hadronic part of the particle cascade generated at the neutrino interaction point.

Considering the AcSource code as provided by Sloan, the input is $n_\nu = log_{10}E_\nu$ [GeV], defining the primary neutrino energy. The model assumes that the amount of energy transferred to the hadronic channel E_H is a fraction of the primary neutrino energy:

$$E_H = y \cdot E_\nu \tag{4.1}$$

where y is the Bjorken scaling variable representing the collision inelasticity [184]. y variable distributes in the range $(0, 1)$, according to its probability density function $P(y)$ that is depending on neutrino differential cross section, and thus on neutrino energy. Looking at the details of the computation, the normalized $P(y)$ is proportional to the differential cross section:

$$P(y) = \frac{1}{\sigma_{TOT}} \frac{d\sigma}{dy} \tag{4.2}$$

To generate a y value, the standard Monte Carlo trick of the inverse transform sampling method is followed [185] and the cumulative function $F(y)$ is considered:

$$F(y) = \int_0^y P(y')dy' \tag{4.3}$$

The cumulative function goes from 0 to 1. Therefore, once that cumulative function tables are built up for every energy decade[2], a random generation selects $F(\bar{y})$, and the corresponding $\bar{y}$ is computed inverting the relation in Equation 4.3 and assuming linear interpolation. $\bar{y}$ identifies E_H (Equation 4.1); n_p is the integer value closest to $n = log_{10}E_H$ and it selects the shower collection. A scaling factor $C = E_H/10^{n_p}$ is applied to take into account the difference between n_p and n. At last, a random generation picks out one of the 100 CORSIKA proton-induced showers in the collection, defining the *rhoEmap* to be used in AcPulse.

4.2.2 Feeding AcPulse with CORSIKA Showers

Coming to computational details in the AcPulse step of the simulation chain, the backbone of the algorithm (sum over spherical surfaces and difference quotient) stays unchanged, therefore the code in Appendix C and the discussion in Section 3.4.2 still constitute a reference on the topic. Modifications are introduced to take into account changes in the geometry of the acoustic source and of the detection point.

Concerning the source, in the case of CORSIKA showers, the energy deposition map is given in cylindrical coordinates and assuming axial symmetry for particles generation and propagation in the hadronic shower. As anticipated in Note 8, Chapter 3, the AcPulse code is modified to accept CORSIKA shower *rhoEmap* as input file.

Moreover, the time resolution (sampling time of simulated pulses) is connected to the binning through the *rstep* parameter, that is set at 0.005 cm. Assuming a constant sound propagation speed (Equation 3.5), this setting corresponds to a sampling frequency in the simulation $f_{MC} = 300kHz$.

[2]The Monte Carlo code makes use of muon neutrino cross section data.

About the geometry of the detection, an important change is connected to the topic anticipated in Note 7, Chapter 3. Increasing the distance between the source and the receiver, the angular extension of the acoustic source in the hydrophone "field of listening" becomes much more smaller. Therefore, there is no need to consider the whole solid angle in the surface integral[3] and, at the same time, a more accurate angular resolution is needed, to better described the (almost point-like) acoustic source. It is important to underline that settings to apply in the AcPulse code depend on the distance between the hydrophone and the acoustic source. In other words, this means that the angular acceptance and the angular resolution has to be tuned with the receiver position with respect to the shower core.

As discussed in Section 2.3, pressure pulses are attenuated while propagating in sea water and attenuation becomes more important with increasing distance from the acoustic source. Since the study of the acoustic pulse generation in the neutrino case involves large source-receiver distances, sound attenuation should play a role, altering the frequency content of the signal far from the generation point. Nevertheless, in the preliminary study presented in this chapter, the code used for computation is based on the Poisson formula (Equation 2.3), and thus *attenuation is not included* in the simulation.

The last comment concerns the fact that the algorithm used for computation has been developed to study the ITEP test beam case, that is a situation in which the receiver is close-by and the acoustic source dimensions are comparable with the geometry of the detection. Therefore, I expect poorer performances at larger distances, when the acoustic source appears as point-like in the hydrophone "field of listening".

4.3 The neutrino-case results

In the following, the procedure to test the AcPulse code coupled with the CORSIKA AcSource Monte Carlo is described.

The first set of results shown in this section are relative to the case $E_\nu = 10^9\,GeV = 10^{18}\,eV$. The selected energy value is in the expected energy range for GZK cosmic neutrinos, Figure 1.9. To take into account fluctuations in the neutrino interactions with matter, the *rhoEmap* considered as acoustic source is the average of 1000 neutrino events. In other words, once that $n_\nu = log_{10}E_\nu[GeV]$ is set, 1000 generations of the y-Bjorken variable are performed, and 1000 proton showers at the corresponding E_H are picked out. The acoustic source used as input file for the AcPulse computation is the arithmetic mean of the selected showers.

Figure 4.1 reproduces an histogram of the distribution of the **y-Bjorken scaling variable**. The mean value is coherent with the predictions of the parton model, according to which only about 20% of the primary neutrino energy goes into the hadronic channel [82].

[3] A proper normalization factor is required, to take into account that integration is performed over a restricted angular portion: the Jacobian computed in Equation 3.10 assumes that θ and ϕ are defined to cover the whole solid angle.

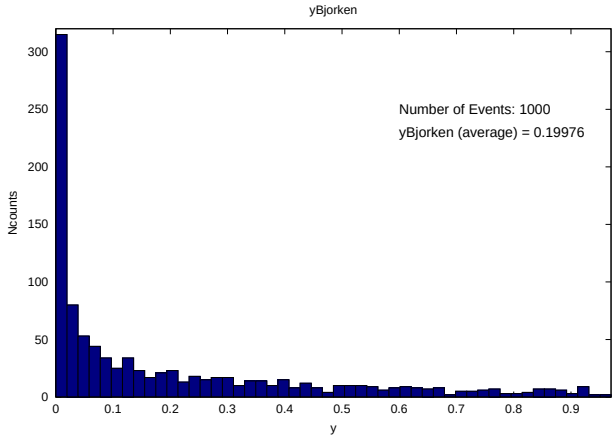

Figure 4.1: y-Bjorken scaling variable distribution. Neutrino initial energy is $E_\nu = 10^{18}\, eV$.

Figure 4.2 is the **longitudinal profile** of the energy deposition, Figure 4.3 is the **radial profile**, at several penetration depth. Results are consistent with expectations; more plots of this kind, at different energies, can be checked in [140].

The longitudinal profile data are used to decide the hydrophone position settings to include in the AcPulse code for computing the acoustic signal at the receiver. According to the model, a coherent signal is expected only over a restricted angular range (the so-called sonic "pancake", Figure 2.1). The maximum acoustic pulse occurs at the maximum of the energy deposition, therefore the most straightforward choice is to select xH coincident with x_{max}, the depth at which the energy deposition profile in Figure 4.2 shows its maximum[4].

Figure 4.4 is a first look at the result of the computation, performed setting $xH = x_{max}$, $yH = 0$, $zH = R$, distance of the hydrophone from the shower axis. More details in caption. The amplitude is given in Pascal, assuming for the Gruneisen coefficient the parametrization discussed in Section 3.4.3. **Environmental parameters** are set as following: temperature T=13.7 °C, salinity S=38.7, depth D=3500 m. These values are assigned considering data collected at the sub-marine sites investigated by the NEMO Collaboration in the Mediterranean Sea [99].

Figure 4.5 enters into details of the acoustic pulse shape in the time domain, considering a larger number of simulated pulses, and examining in particular how the amplitude of the positive peak of the pressure pulse and the symmetry coefficient R/C (Figure 3.23) change with increasing distance from the acoustic source. In this very preliminary study, a constant error is assigned to each value in the plot, to get the relative error larger for values computed at larger distances. This because, as already underlined, the AcPulse algorithm is optimized for close-by receivers and extended sources, and larger uncertainty is expected at large R. No error bars are added to the symmetry factor values.

Concerning the **symmetry factor** R/C, in Figure 4.5 plot [b] we see that the symmetry factor approaches 1 as the distance increases. This makes sense, since

[4]Another possibility is to evaluate the position x_{med}, defined as the depth at which the energy deposition "splits in two" (considering the cumulative of the deposition profile, half the energy is deposited behind x_{med}, the other half beyond) and then take $xH = x_{med}$.

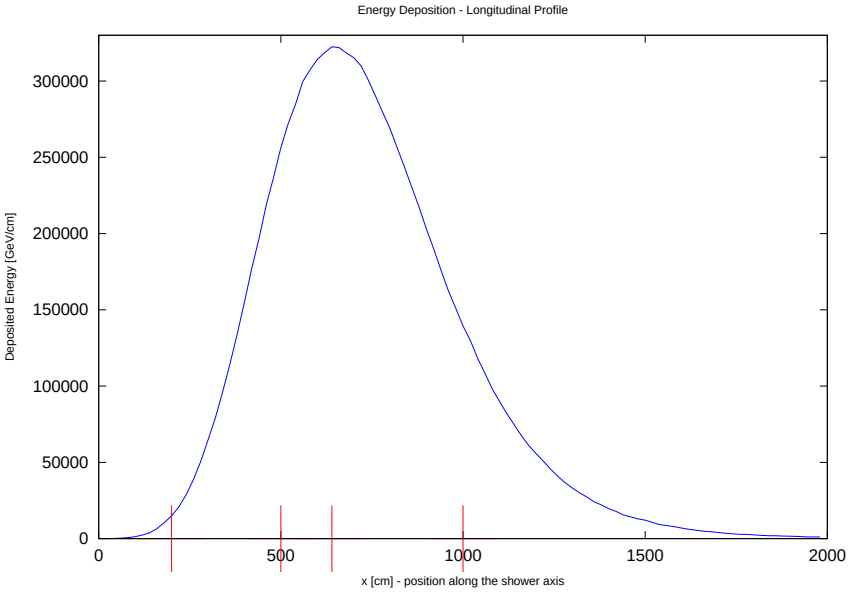

Figure 4.2: Energy Deposition - Longitudinal Profile. The red markers identify the depth at which the radial profile is shown in Figure 4.3. Neutrino initial energy is $E_\nu = 10^{18}\, eV$.

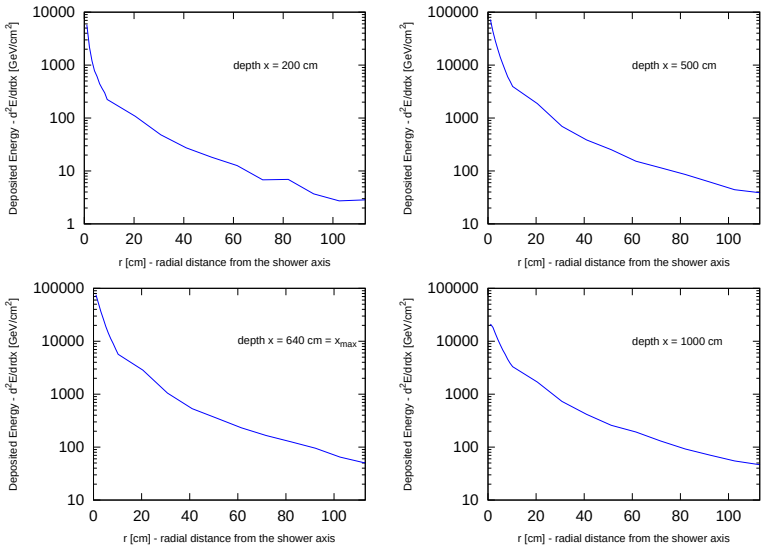

Figure 4.3: Energy Deposition - Radial Profile. x_{max} is the depth at which the longitudinal profile has its maximum (see Figure 4.2). Neutrino initial energy is $E_\nu = 10^{18}\, eV$.

the further the hydrophone is, the more point-like the acoustic source appears, and therefore the more the pressure signal approaches a perfect bipolar pulse. The outcome is consistent with result reported by Askaryan [133], who suggested to use a measurement of the symmetry factor as an indication on the distance between the acoustic source (neutrino interaction point) and the receiver. Figure 4.6 develops more deeply the comparison with Askaryan, evidencing a dependence on the shower development (longitudinal and transverse size), and therefore on the shower energy. Details in caption.

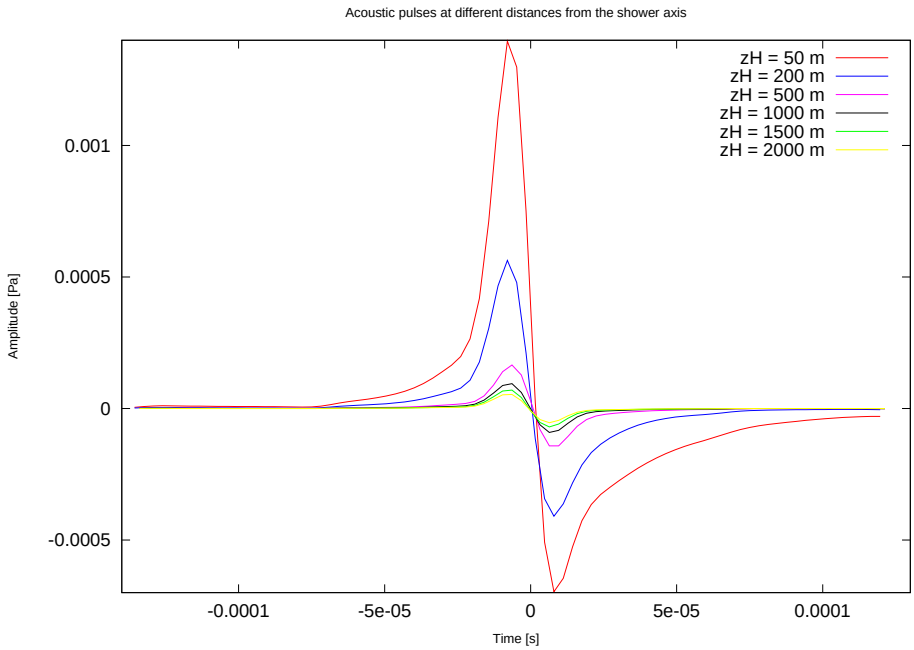

Figure 4.4: Acoustic pulses at different distances from the shower axis. A reduced number of signals is included, to avoid a too crowded plot. The time origin is translated at the pulse center. Assuming $t = 0$ at the neutrino interaction time, and instantaneous energy deposition, the actual time of pulse occurrence at the receiver is a function of the distance from the acoustic source (Equation 3.5). Neutrino initial energy is $E_\nu = 10^{18}\, eV$.

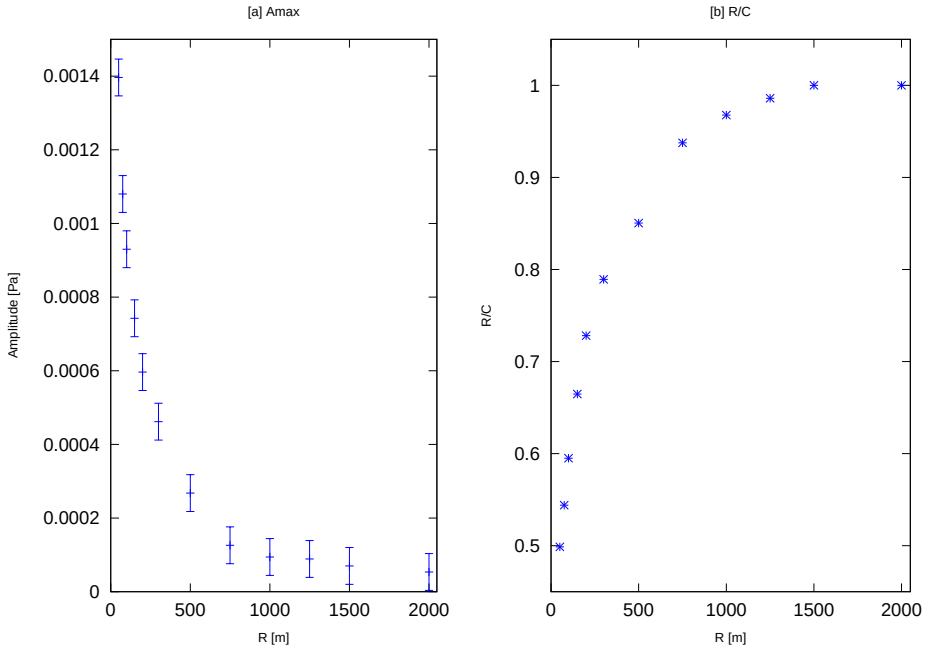

Figure 4.5: Peak amplitude and symmetry factor versus distance. Neutrino initial energy is $E_\nu = 10^{18}\, eV$.

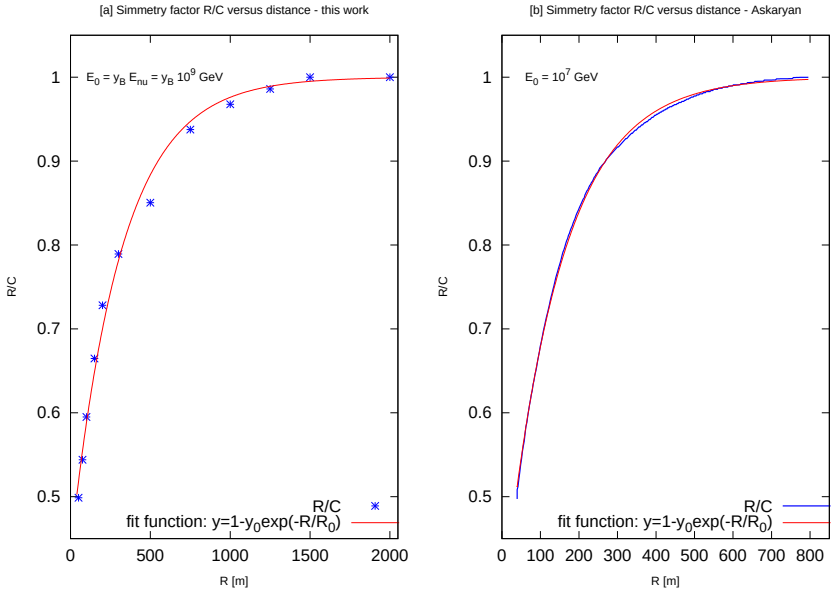

Figure 4.6: Symmetry factor versus distance. Comparison with Askaryan simulation results [133]. It is interesting to notice that the fit function I selected well describes, in both cases, the dependence of the symmetry factor on distance. This very preliminary analysis allows to advance the hypothesis that y_0 fit parameter is related to the value of R/C ratio at small distances and that R_0 parameter seems to be connected with the transition from near to far field conditions (see Equation 4.4). The distance ρ around which the transition occurs is of course depending on the shower energy, since E_0 defines the longitudinal and radial development of the energy deposition. Results of the fit are: plot [a], $y_0 = 0.56$, $R_0 = 316.5m$; plot [b], $y_0 = 0.64$, $R_0 = 144.5m$.

Concerning Figure 4.5 plot [a], a more detailed study of **signal amplitude dependence on distance** can be carried on following the account given in [152]. Considering the case of a cylindrical energy deposition ("hot rod"), the so-called *near field* regime extends up to a distance:

$$\rho = \frac{L^2}{\lambda} \tag{4.4}$$

where L is the length (longitudinal size) of the acoustic source, λ is the wavelength of the acoustic pulse, connected with the source diameter (transverse size) through Equation 3.15, $\lambda = 2 \cdot D$. If distance R between the shower axis and the receiver fulfill the near field regime requirements, that is $R < \rho$, the model predicts the signal amplitude varying as $1/\sqrt{R}$. The case $R \gg \rho$ identifies the *far field* regime, where a $1/R$ amplitude dependence on distance is expected (cylindrical wave) and an almost symmetric bipolar pulse is predicted. We expect a transition from near field to far field conditions in a range around ρ. Introducing in Equation 4.4 the values corresponding to the CORSIKA shower energy deposition, the transition is estimated at a distance around 200-400 meters. Results shown in Figure 4.7 follow the expectations.

An additional check is signal **amplitude versus energy**. Askaryan predicted a linear dependence, and my simulation outcome confirms the result, as shown in Figure 4.8, details in caption.

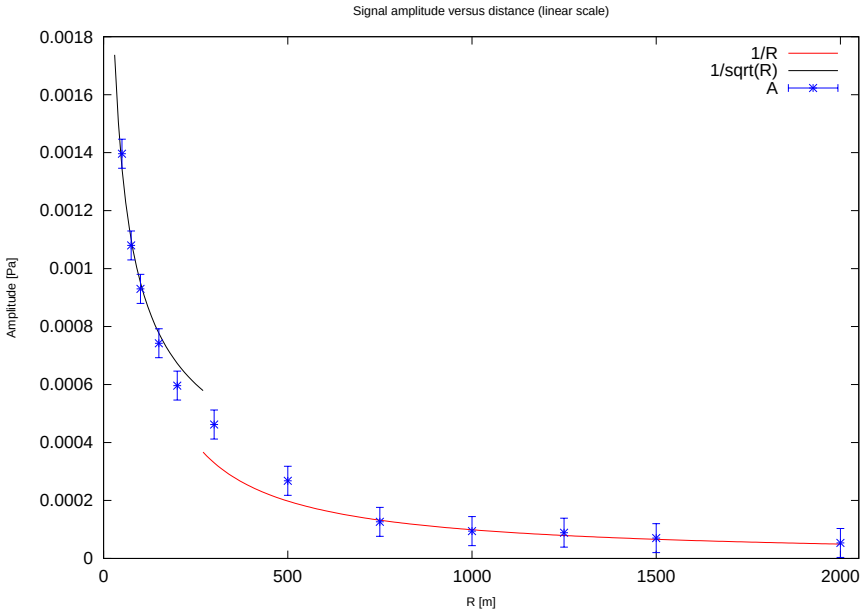

(a) Signal amplitude vs distance - linear scale

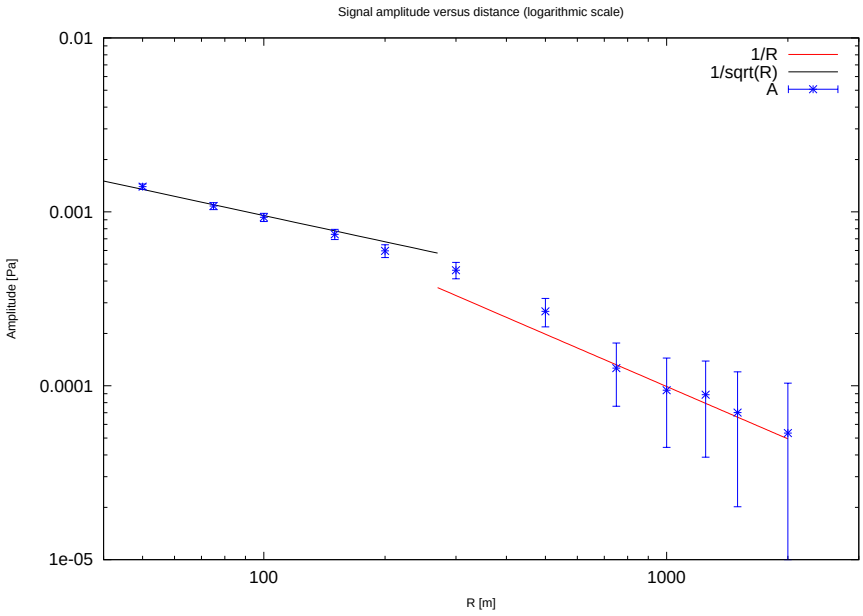

(b) Signal amplitude versus distance - logarithmic scale

Figure 4.7: Signal amplitude versus distance. The results are consistent with the predictions of the model. Near field and far field regime are distinguished, the transition is at the distance scale predicted by Equation 4.4. Plot [a] reproduces results of the computation on linear scale, plot [b] on logarithmic scale, to better evidence the change of slope at the transition.

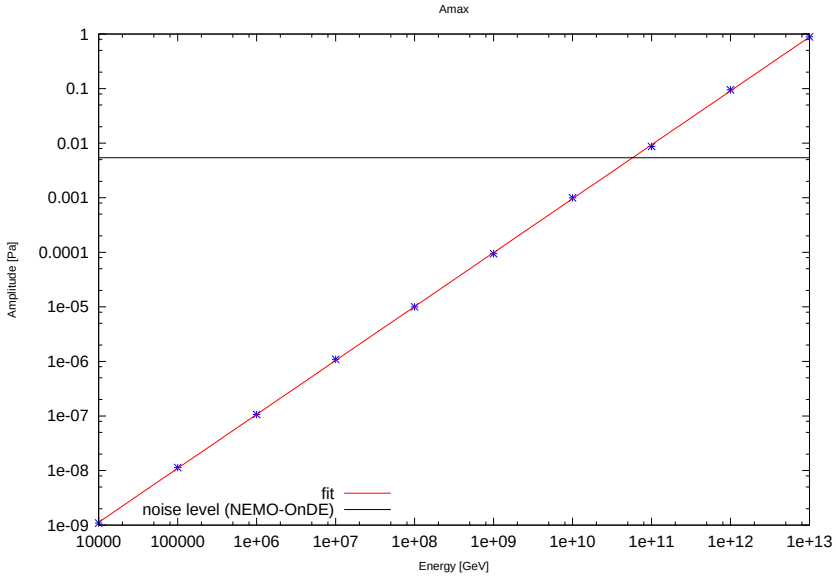

Figure 4.8: Signal amplitude versus initial neutrino energy. A linear dependence comes up, in agreement with predictions. Simulation is carried on assuming $zH = 1km$, $xH = x_{max}$, environmental parameters as discussed in the text. The horizontal axis is neutrino initial energy E_{nu}, that differs from the shower energy E_H because of the y-Bjorken scaling factor (Equation 4.1). Table 4.1 lists the y-Bjorken scaling variable for each energy, computed as the average over 1000 random generations. If amplitude is plotted versus E_H, the result of the fit ($A \propto E^{1.02}$) is in very good agreement with Askaryan, who reported $A \propto E^{1.07}$ [133]. The black line identifies the noise level measured by the NEMO-OνDe submarine station [146]. It provides an indication for a rough estimate of the energy threshold for neutrino acoustic detection. Improvements in the signal to noise rejection are achieved including matched filter and beam forming techniques, see text for details.

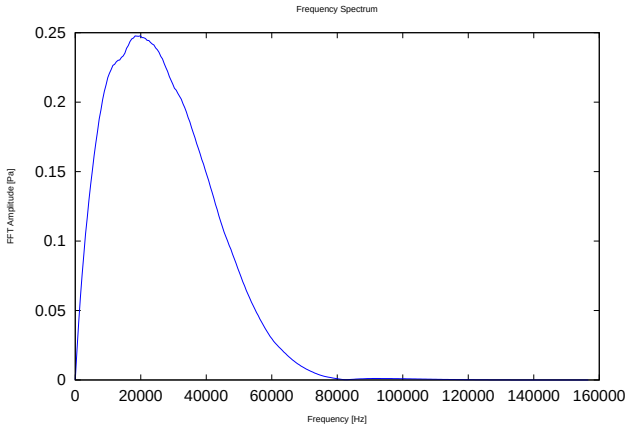

Figure 4.9: Frequency spectrum of the acoustic pulse, computed assuming $zH = 1km$, $xH = x_{max}$ (no attenuation is included in the simulation). The energy of the hadronic shower is $E_H = 10^{11}$. The outcome in the plot is the absolute value of the Fast Fourier Transform (FFT) computed in Octave. The most of the frequency content is in the frequency range [10-50] kHz.

The black line in the plot identifies the noise level reported by the NEMO Collaboration as result of the measurements taken in the Mediterranean Sea by the NEMO-OνDe submarine station (see Section 2.4) [146]. The value accounted for the average acoustic sea noise is 5 mPa RMS, in the band [20-43 kHz], that is where neutrino-induced acoustic signals are expected in the frequency domain (see Figure 4.9). Combining the NEMO-OνDe results and the outcome of the simulation, preliminary information on the signal to noise ratio can be extracted. In particular, the comparison allows to advance a rough estimate of the energy threshold for acoustic neutrino detection. A window of observation is open at about 10^{11} GeV in neutrino energy; GZK expectations and several top-down models (Z-bursts) predict neutrinos in this range (see Section 1.2.1 and Figure 1.9).

In addition, it is important to underline that the approximate indication coming from Figure 4.8 has big room for improvement, since a comparison in amplitude is not the only strategy for signal to noise rejection. Additional techniques, as matched filter [186] and beam forming [187], are available to lower the energy threshold and increase the signal to noise ratio; their application to the neutrino case in underwater environment is under study [145] [144] [188] [150].

$\log(E_\nu[\mathrm{GeV}])$	y-Bjorken
4	0.42079
5	0.33401
6	0.25903
7	0.24137
8	0.21452
9	0.19976
10	0.21297
11	0.18820
12	0.20608
13	0.19285

Table 4.1: y-Bjorken scaling variable. For each neutrino initial energy, the corresponding y-Bjorken is the result of an average over 1000 random generation (Section 4.2.1). Values in the table are used to compute energy of the hadronic shower from initial neutrino energy in Figure 4.8.

The next topic is related to investigations on the **sonic "pancake"**. The matter is connected to the shape of the wave front during the propagation, and the model predicts strong anisotropy (the "pancake"), and a connection between the line of listening and the shower axis. As suggested by Askaryan in [133], the shape of the pancake can provide some hints on the direction of the neutrino propagation.

Simulation is carried on fixing the shower energy ($E_H = 10^{11} GeV$), selecting a distance from the shower axis (zH = 1 km) and moving the hydrophone along the x direction, computing the acoustic pulse at different xH. Results can be plotted as function of bf Θ:

$$\Theta = arctan\left(\frac{xH - x_{max}}{R}\right) \tag{4.5}$$

Θ identifies different "lines of listening": $\Theta = 0$ is when $xH = x_{max}$, with the line of listening perpendicular to the shower axis; this condition defines the *median plane*. $\Theta = 0.035°$ corresponds to x_{med}. The geometry illustrating Θ definition is sketched in Figure 4.10.

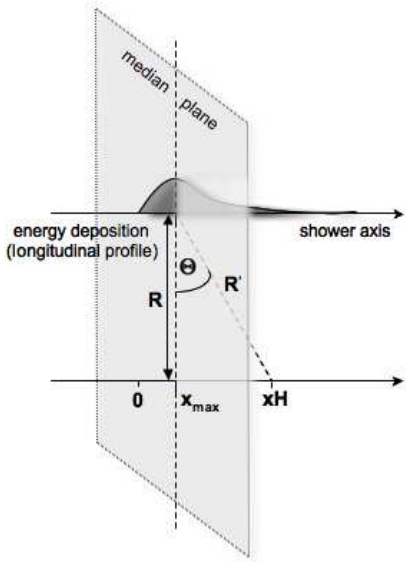

Figure 4.10: Definition of the angle Θ and a sketch of the geometry.

Results are presented in Figure 4.11-4.14. Figure 4.11 displays the value of the **peak pressure** versus Θ and compares the outcome of the simulation work with results of previous studies. The plot can be considered an image of the "pancake". It is important to notice that the peak amplitude of the pressure pulse reduces of about one order of magnitude for an angular shift of about 1.5°, and the reduction is of a factor one hundred if the shift is of about 5°.

The additional horizontal scale in Figure 4.11 represents the position of the hydrophone along the shower axis, with respect to x_{max}. It displays the segment corresponding to the angular window of 6° around the position where the maximum is exhibited, if the distance between the source and the receiver is 1 km. The result can offer some clues when working out the project for an underwater acoustic neutrino telescope, designed as an array of hydrophones. The segment, in fact, provides indications on the relative distances between acoustic sensors in the array and can yield some hints for selection algorithms and signal reconstruction. For instance, assuming the neutrino interaction occurring 1 km away from the hydrophone array, a cluster of hydrophones, in proximity of the median plane and whose spacing is about 50m, can intercept and reconstruct the "pancake"[5]. Alternatively, having a

[5]Nevertheless, the chance to reconstruct the whole "pancake" in underwater environment appears quite remote. A spacing of 50 m between sensors, in fact, limits the main advantage of the acoustic technique in water. As discussed in Section 1.3.3, the possibility to complement and extend the Cherenkov telescope lies on the large value of sound attenuation length, that offers the opportunity of a sparse array of sensors, the only practical solution to go beyond the km^3. However, a compromise solution can be considering a certain number of clusters (randomly?) distributed in the instrumented volume.

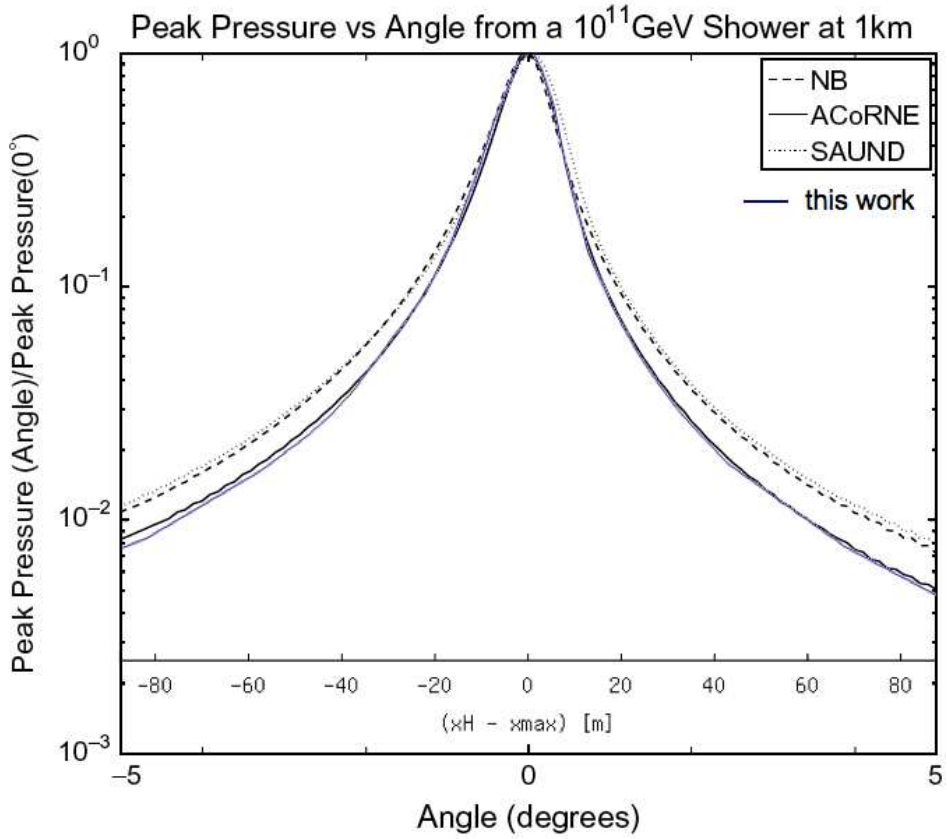

Figure 4.11: Peak pressure versus angle Θ (defined in Equation 4.5). The blue line is the result of the present simulation, carried out as discussed in the text and compared with results of previous works, as they are presented in [140]. Entering the details, the ACoRNe Collaboration carried on the computation of pressure pulses using three different parametrization of the acoustic sources ("NB" is the short for "Niess, Bertin" and refers to the work presented in [131] and [145]; "SAUND" refers to the activity completed by Vandenbroucke, Gratta and Lehtinen in the framework of the SAUND experiment (Section 2.4) and reported in [142]; "ACoRNe" is the outcome of the studies carried out by the ACoRNe Collaboration using CORSIKA, see Section 4.2). The comparison is successful, in particular with "ACoRNe", in agreement with the fact that in both cases, the same CORSIKA showers are used as acoustic source. The additional horizontal scale shows the segment along the shower axis corresponding to the angular window in the plot, for zH=1 km (see the text for details).

single hydrophone rather than a cluster, a displacement of about 50m with respect to the median plane should not rule out the possibility of detecting the acoustic pulse. These preliminary reasoning thus suggests some guidelines for selection algorithms in data analysis.

Additional information for reconstruction comes from considering not only the peak pressure, but taking into account others parameters useful to characterize the bipolar pulse in the time domain, such as pulse asymmetry, pulse duration and pulse centre. Figure 4.12 carries on the comparison with results reported in [189], reproducing the variation of the **pulse asymmetry** with angle. Analogue to the symmetry factor R/C, the asymmetry parameter a is an additional variable to quantify the

difference between the rarefaction (negative) peak and the compression (positive) peak of the acoustic bipolar pulse:

$$a = \frac{|A_{max}| - |A_{min}|}{|A_{max}| + |A_{min}|} \tag{4.6}$$

The asymmetry parameter is positive when the compression peak (A_{max}) is larger that the rarefaction peak (A_{min}), it is negative vice versa, and it is equal to zero if the pressure pulse is perfectly symmetric.

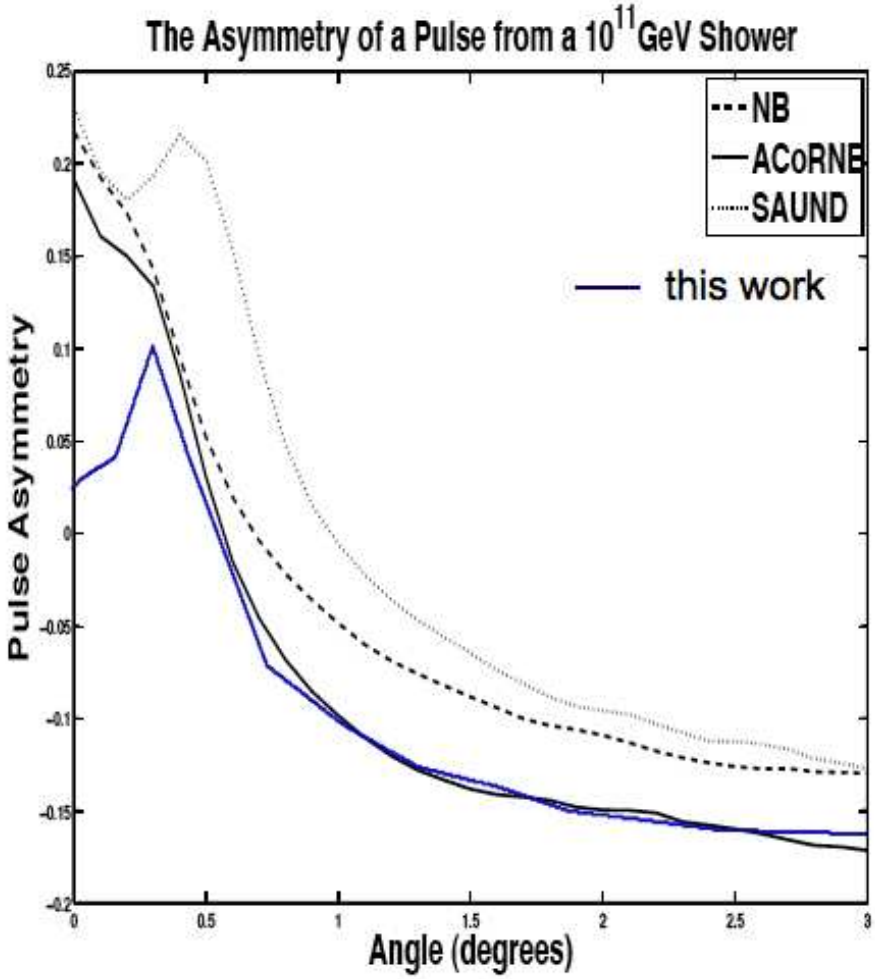

Figure 4.12: Pulse asymmetry versus angle - a comparison with previous studies. The outcome of the simulation (blue line) is compared with results of previous works (for details about the plot legend, see Figure 4.11, caption). The result is consistent with ACoRNe prediction, but there is an important discrepancy at small angles.

Looking at Figure 4.12, the trend of the computation carried out for this work is consistent with previous studies, and in good agreement with ACoRNe results, but there is a significant difference at small angles, since the acoustic pulses following from my simulation look much more symmetric. This result was already in evidence in Figure 4.6, where the agreement with Askaryan's result shows that, moving away

from the source, the acoustic signal in the median plane approaches quite fast a perfectly symmetric bipolar pulse. Moreover, beside the fact that the asymmetry value is different at small angles, the outcome of this work exhibits a "peak" at about 0.3° that resembles the result produced by the SAUND Collaboration. In conclusion, the variation of the asymmetry parameter with angle must be investigated further, with additional statistics of simulation, since it can be a valid tool for signal reconstruction. Figure 4.13 shows the complete set of asymmetry values in the angular window [-6°,6°].

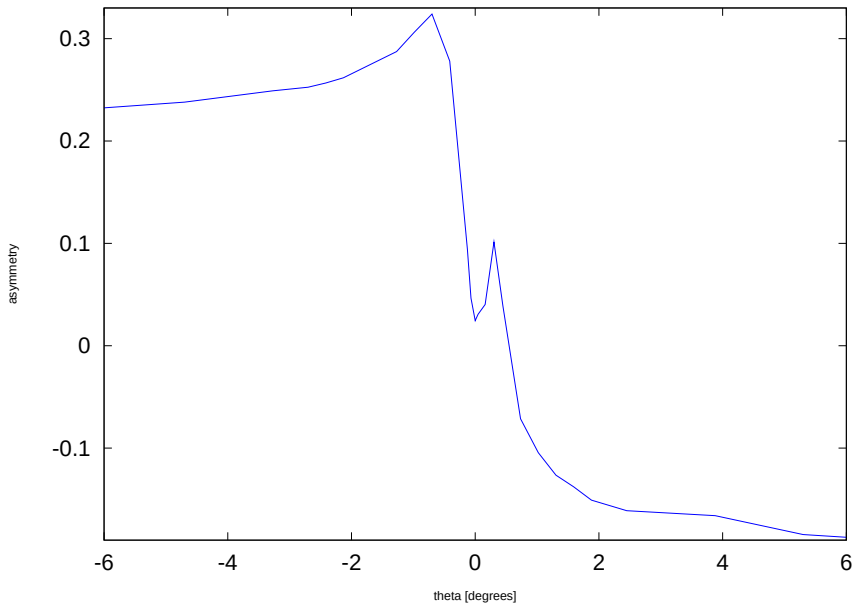

Figure 4.13: Pulse asymmetry versus angle in the angular window (-6°,6°).

Figure 4.14 and 4.15 complete the study, reporting the variation with Θ of the **pulse duration** Δt and the **pulse center** t_0 (both defined according Niess-Bertin parametrization, Figure 3.23). Results are in agreements with expectations.

In particular, for what concerns t_0, an easy check comes from the fact that it represents the time of arrival of the perturbation to the hydrophone, that is the interval required to travel the distance between the hydrophone and the source, at the speed of sound (Equation 3.5). In this case, $v = 1566.5\,m/s$, computed in AcPulse, using parametrization in Equation 3.12 and environmental parameters from results of the NEMO Collaboration measurements. A good estimate of the distance is the value R' reported in Figure 4.10, that is the distance from the hydrophone to the "core" of the energy deposition:

$$R' = \sqrt{R^2 + (x_{max} - xH)^2} \qquad \text{or} \qquad R' = \frac{R}{cos\Theta} \tag{4.7}$$

Combining Equation 3.5 and 4.7, a $\frac{1}{cos\Theta}$ dependence for t_0 is expected, as it is verified in Figure 4.14.

Figure 4.15 shows the result for Δt. The plot confirms the expectations, according to which the pulse duration increases if moving away from the median plane.

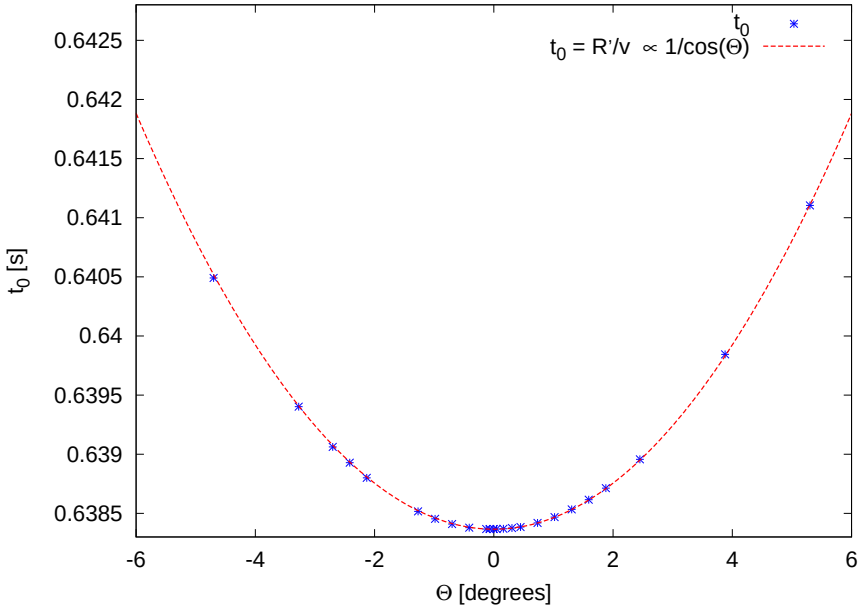

Figure 4.14: t_0 (pulse centre) versus angle. The blue line is the output of the simulation concerning the t_0 parameter, as defined according Niess-Bertin parametrization. The red line is the result of the calculus, taking into account Equation 3.5 and 4.7. The outcome in the plot is valid under the assumption of constant sound speed, and thus ray-tracing computation for sound propagation.

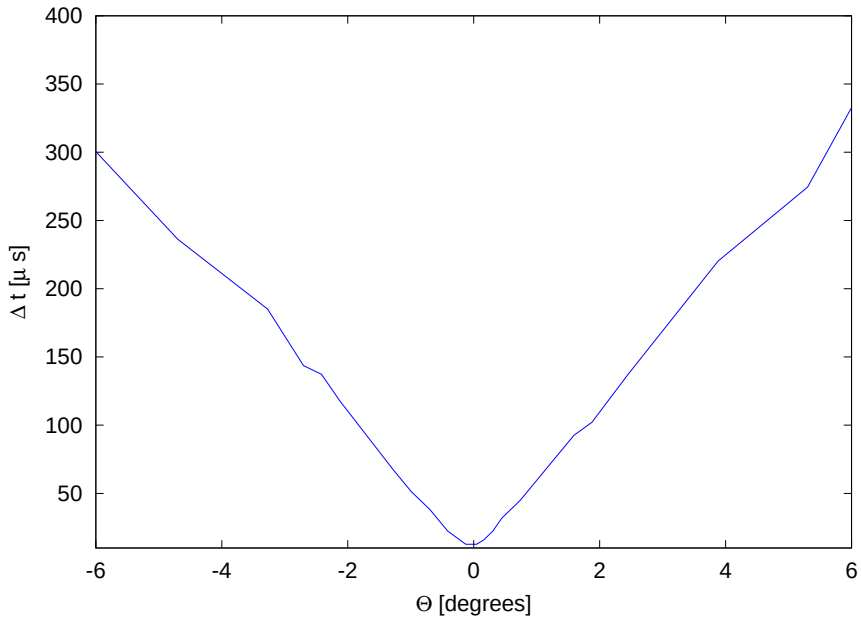

Figure 4.15: Δt (pulse duration) versus angle.

The same conclusion is in evidence in Figure 4.16, that reproduces the outcome of the simulation in the time domain, for several hydrophone positions.

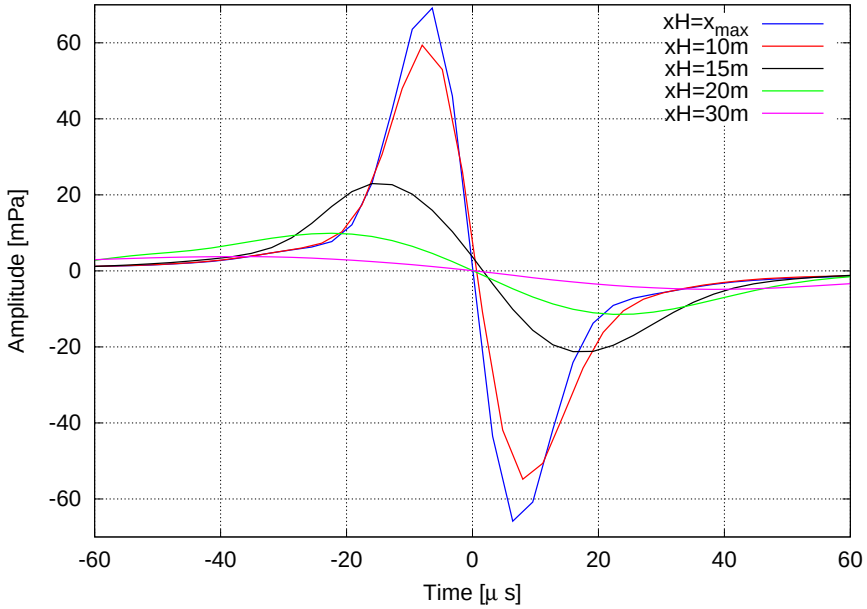

Figure 4.16: Acoustic pulses in the time domain, for several hydrophone positions. Pulse duration has a minimum if the acoustic pulse is computed in the median plane. This plot should be compared with Figure 2 in [142], but the curves are not easily superimposable, because of the difference in the asymmetry parameter at small angles.

The last topic presented in this section is a preliminary **comparison to previous studies** concerning the characteristics of simulated acoustic pulse in the time domain. Two comparisons are carried out, and results are presented in the form of a table, following Niess's report in [131].

The first comparison concerns the case of an hadronic shower with $E_H = 10^7$ GeV, "listened" from a distance $zH = 400m$ and with hydrophone placed at the shower maximum ($xH = x_{max}$). Table 4.2 summarizes the results, listing data reported by Niess in [131] and adding the outcome of this study. My computation assumes that each amplitude has been scaled according to the Gruneisen factor evaluated with environmental parameters given in [131][6].

	$\mathbf{A_p}[\mu\mathbf{Pa}]$	$\mathbf{\Delta t}[\mu\mathbf{s}]$	$\mathbf{R/C}$ [%]
Askaryan [133]	25	17	100
Learned [139]	3	20	50
Dedenko [190]	44	10	75
Niess [131]	47	10	35
this work	26	16	87

Table 4.2: Acoustic pulse characteristics ($E_H = 10^7$ GeV, and $zH = 400\,m$) - Comparison with previous studies. Lines 1-4 are taken from [131]. Parameters listed in the table are defined in 3.23.

[6]In [131], the author claims to use $\beta = 2.1 \cdot 10^{-4} K^{-1}$, $C_p = 3.6 \cdot 10^3 J \cdot kg^{-1} \cdot K^{-1}$. No mention is given concerning the speed of sound used in the computation, therefore the nominal value $v = 1500 m/s$ is assumed.

Looking at the listed results, it is of interest that the signal duration is pretty similar in all cases. Differences in amplitude can be related to different energy deposition distribution, and may be corrected taking into account uncertainties. The most significant discrepancy among the several computation concerns the symmetry factor. This point, as already underlined, should be investigated more deeply. My result is in very good agreement with Askaryan's: this may be connected to the fact that the algorithm of computation in AcPulse comes from the account given in [133].

The second comparison considers results presented in [140] and in [142], corresponding to the acoustic pulse generated from an hadronic cascade with energy $E_H = 10^{11}$ GeV and "listened" at $zH = 1\,km$. Results are listed in Table 4.3. The signals are assumed scaled at the Gruneisen coefficient factor given in [140].

	$\mathbf{A_p}$[mPa]	$\mathbf{\Delta t}[\mu s]$	R/C [%]
SAUND [142]	52	9	73
SAUND [140]	47	19	67
ACoRNe [140]	80	16	64
this work	68	13	95

Table 4.3: Acoustic pulse characteristics ($E_H = 10^{11}$ GeV, and $zH = 1\,km$) - Comparison with previous studies. Two different data set for SAUND are due to the fact that data in line 1 refers to computation carried out by the SAUND Collaboration [142], and line 2 is the outcome produced by the ACoRNe Collaboration, using the SAUND parametrization of the shower profile [140]. Parameters listed in the table are defined in 3.23.

Again, the most significant discrepancy concerns the symmetry factor, as already discussed in Figure 4.12. Taking into account the definition of A_p, differences in the symmetry factor correspond also to differences in the reported amplitude. Variations in the pulse duration look less significant. Moreover, it is interesting to underline that line 1 and line 2 in the table are computed considering the same parametrization of the shower profile ("AcSource" step of the simulation) and an independent computation of the acoustic pulse ("AcPulse" step of the simulation); on the contrary, line 2 and 3 come from different AcSource and the same AcPulse; line 3 and line 4 have, again, the same AcSource, and a different AcPulse. The conclusion is that fluctuations in the results of different studies may be due both to the Monte Carlo of neutrino interaction and both to the algorithm of computation of the acoustic pulse. This short comment provides a confirmation about the need of additional investigations in the field, in order to improve the computation of expected neutrino-induced acoustic signals.

Chapter 5

Summary and Outlook

The review presented in Chapter 1 - 2 attests that **neutrino astronomy is a very lively field of research** and documents developments and achievements in neutrino detection. Cherenkov apparatuses constitute the present generation of neutrino telescopes. Several projects are ongoing, exploiting ice, fresh water and sea water as natural target for neutrino interactions. Existing telescopes have already been able to test technologies and reconstruction strategies to investigate neutrino events. Technical solutions and resources developed for optical detectors enable the deployment of sub-marine (or in-ice) infrastructures with instrumented volume up to about 1 km^3.

Next generation telescopes have to consider the integration of alternative techniques, to complement Cherenkov observations, and to extent the detector sensitive volume beyond the km^3. Radio and acoustic proposals fulfil the requirements, a lot of work is in progress to check the feasibility of the techniques for ultra-high-energy neutrino detection.

Concerning in particular the acoustic technique, the activity concentrates in the development of acoustic modules (hydrophones and glaciophoes), the calibration of sensors, the simulation of expected neutrino-induced acoustic pulses, the investigation of data analysis techniques and reconstruction strategies. Another major topic is the evaluation of the acoustic noise background in selected candidate site. Such measurements are important to estimate the performances of the acoustic technique and provide hints for noise rejection algorithms.

The idea of acoustic detection was advanced by Askaryan in the late '50s. The mechanism that causes the generation of acoustic pulses as a consequence of ultra-high-energy neutrino interactions is the thermo-acoustic model. Energy released in the medium induce a perturbation of the thermal equilibrium that propagates as a pressure wave.

An outline of the main features to be considered when evaluating the feasibility and the performances of the acoustic detection evidences four fundamental steps, interlinked and correlated to each other.

The first step consists in **modeling ultra-high-energy neutrino interactions**, in order to calculate the map of the energy deposition. (the *AcSource* block in the simulation chain described in Chapter 3). The critical point at this level is the fact that neutrino-nucleon cross section is not completely determined, and assump-

tions are based on extrapolations from lower energy experimental data. In addition, the occurrence of the LPM effect alters the development of electro-magnetic showers, introducing fluctuations in the energy deposition longitudinal profile.

The second step is the **definition of the acoustic signature** expected from neutrino interactions (the *AcPulse* block in the simulation chain). Assuming a model for neutrino interaction, that is a known energy deposition profile, the goal of these studies is to compute expected neutrino-induces acoustic pulse. This stage of the calculus should include a model of sound propagation, to get a more accurate description of the generate acoustic pulse in the frequency domain The environmental property should also be taken into account, since they affect the signal amplitude.

The outcome of this second step of investigation is crucial, since it provides hints for the next feature, that is the **design of reconstruction strategies** for acoustic neutrino detection and background noise rejection. The most promising strategies in this field are matched filters and beam forming techniques.

Reconstruction algorithms are connected with the last topic in the list, that is the **definition of the optimized geometry** of an hydrophone array to be implemented in an underwater (or in-ice) neutrino telescope. An important outcome of this step is the opportunity to set detector sensitivity to neutrino events.

The present work concentrates on the first two topics of the above list (energy deposition profiles and acoustic pulse computation); it considers the case of acoustic detection in water. The goal of this thesis consists in using protons (the simulation code implemented to study the proton test beam) to better understand the neutrino case. Protons are the appetizer and neutrinos the main course, nevertheless protons constitute a rich premise, since a lot of work has been carried out in the framework of the ITEP test beam, an experiment we did to test the acoustic technique, employing the ITEP protosynchrotron accelerator facilities.

The **ITEP test beam experiment**, described in Chapter 3, has validated the possibility of a thermo-acoustic detection of particles, since acoustic signals resulting from proton beam interactions in water have been registered with hydrophones. In addition, it has been a fruitful test-bench to get familiar with techniques and devices for acoustic detection in underwater environment. Preliminary results on proton beams have been completed and complemented with the important contribution of a dedicated Monte Carlo simulation. The Monte Carlo allowed a control on the model parameters, gaining a deeper understanding of the thermo-acoustic mechanism and setting the conditions for future test beam experiments.

The successful comparison between acquired data and simulated pulse, and the agreement with with predictions of the thermo-acoustic model and with results produced by Sulak *et al* (in particular for what concerns hydrophone energy calibration and linearity of the pulse amplitude with the total deposited energy, Figure 3.29) has given support to the simulation algorithm, enabling to move to the neutrino case, transferring the achievements acquired with protons.

The study of **the neutrino case**, discussed in Chapter 4, considers neutrino-induced hadronic showers as acoustic source. The outcome of the computation produces results in agreement with the model for what concerns the signal amplitude dependence on the distance between the acoustic source and the receiver (Figure 4.7). The symmetry factor is a parameter evaluating the ratio between the rarefac-

tion peak and the compression peak of the pressure pulse. Concerning the symmetry factor, results from the simulation are in agreement with Askaryan results, allowing to advance an hypothesis on a correlation between the symmetry factor (i.e. the shape of the acoustic pulse) and the distance from the source (Figure 4.6).

Signal amplitude shows a linear variation with primary neutrino energy, in very good agreement with Askaryan results. In addition, combining the outcome of the simulation with measurements performed with the NEMO - OνDE station on sea noise level in Catania test site, a preliminary indication on neutrino energy threshold accessible to acoustic detection can be achieved (Figure 4.8). The resulting value ($E_\nu \sim 10^{11}$ GeV) is compatible with GZK events, and with several top-down models. Nevertheless, it must be underlined that the selected threshold can be lowered and signal-to-noise ratio can be increased if matched filters and beam forming techniques are taken into account.

Investigations on the "acoustic pancake" consists in exploring the shape of the pressure pulse if the hydrophone is moved away from the median plane, that is the position, orthogonal to the particle shower axis, at which the signal exhibits the maximum value. Results concerning the peak pressure variation in the pancake are in good agreement with previous studies (Figure 4.11). Information available from the plot can provide hints for the design of the array geometry. Some discrepancies are observable in the pulse asymmetry, the simulation presented in this work producing a much more symmetric pulses than results from previous computation. The pulse duration is also reported, the pulse duration increases for pulses registered off the median plane.

The last topic presented in the analysis is the comparison with previous studies, reported in Table 4.2 and 4.3. Results show a very good agreement with the computation of Askaryan, relative to pressure pulses from hadronic cascades with energy $E_H = 10^7$ GeV. Considering the case of hadronic cascades with energy $E_H = 10^{11}$, some discrepancies are accounted, mostly for what concerns the pulse asymmetry. This deviation evidences the presence of some uncertainties are in the model, and may be due to differences both in the simulation of ultra-high-energy neutrino interactions and in the acoustic pulse computation algorithm.

Concerning the neutrino case, results presented in this thesis have to be considered preliminary. In the top list of future developments there is the introduction of sound attenuation in the computation, and more careful investigations in the frequency domain. In addition, some optimizations of the simulation chain may be included, to get a more efficient computation.

A conclusive remarks underlines the fact that stronger cooperation between people working in the field should be encouraged, to better cross-checks methods and results, and to faster progress in the definition of expected neutrino signatures. The ARENA Workshops contribute, in this sense, to create a community in which achievements and results can be shared, carrying on, at the same time, a close relationship between alternative techniques and "traditional" Cherenkov detection. As widely underlined in Chapter 1, efforts of people involved in the field of neutrino telescopes should stay focused on **hybrid detection**, and on the opportunity of cross-calibration and coincidences with different experiments. The challenge of cosmic neutrino detection is a very hard task to manage, and we cannot afford to waste any sign of these elusive particles.

Appendices

Appendix A

Geant4 Simulation of the ITEP Test Beam

In the following, I will give a description of the Geant4 Monte Carlo code I used as AcSource code for the ITEP test beam simulation[1]. I will pay attention in particular to the implementation, for the ITEP application, of the so-called **Mandatory User Classes**: *DetectorConstruction* and *PrimaryGeneratorAction*, since they play a crucial role in reproducing the experimental setup and defining the acoustic source shape.

A.1 The *main* method

To build a Geant4 application, the first condition is the *main* method, that must be included by the user and it is required to complete the simulation program.

The first operation to perform inside the *main* method is to create an instance of the toolkit class *G4RunManager*:

```
G4RunManager* runManager = new G4RunManager;
```

The *RunManager* assumes a leading role in controlling the two main phases in the flow of the program: initialization (build the simulation) and action (run the simulation).

Initialization procedures include description of the geometry and definition of the physics processes taken into account:

```
runManager->SetUserInitialization(new ItepDetectorConstruction);
runManager->SetUserInitialization(new ItepPhysicsList);
```

ItepDetectorConstruction is an example of a user initialization class derived from the toolkit class *G4VUserDetectorConstruction*. It implements the detector geometry and the materials used in detector construction, and it defines the detector sensitive regions. A detailed description will be discussed in Section A.2.
ItepPhysicsList is derived from *G4VUserPhysicsList* and allows to define the catalog

[1] The main reference I follow in this account is "Geant4 User's Guide for Application Developers",
`http://geant4.web.cern.ch/geant4/UserDocumentation/UsersGuides/ForApplicationDeveloper/html/`

of available particles and the list of activated physics processes.
Both *DetectorConstruction* and *PhysicsList* are Mandatory User Classes, since no simulation can work if they are not defined.

For what concerns **action** managing, the most important instruction is

```
runManager->SetUserAction(new ItepPrimaryGeneratorAction);
```

that makes the particles generator, creating an instance of the toolkit class *G4VUser PrimaryGeneratorAction*. This is where the proton beam injection mechanism is specified, including the beam profile design. Details will be presented in Section A.4. *PrimaryGeneratorAction* is a Mandatory User Class as well: simulation requires the definition of primaries.

Other action procedures involve the setting of objects that specify any additional operations one can request during the run (the execution of the program), during the event (each run can consist of several events), and during the step-by-step simulation (each elementary slice of action that constitutes the event itself - such as any occurrence of interaction or detection process). Examples of these **Optional User Action Classes** are in the following lines:

```
runManager->SetUserAction(new ItepRunAction);
runManager->SetUserAction(new ItepEventAction);
runManager->SetUserAction(new ItepSteppingAction);
```

Typical tasks requested at different stages of the program can be the information collection, or the computation of physical quantities, or the enabling of output files.

Initialization takes place with the instruction:

```
runManager->Initialize();
```

that is responsible to arrange the simulation according to what previously selected with initialization methods.

At last, we have got the method:

```
G4int numberOfEvent = 1;
runManager->BeamOn(numberOfEvent);
```

that activates the simulation itself.

RunManager methods *Initialize* and *BeamOn* check the existence of the Mandatory User Classes.

In addition, the *main* method is where **Visualization** and **User Interface** procedure are included and initialized.

The following lines create the User Interface session for interactive mode and gets the pointer to the User Interface manager:

```
G4UIsession* session = new G4UIterminal();
G4UImanager* UI = G4UImanager::GetUIpointer();
```

The User Interface manager controls the execution of commands. A common usage consists in defining a macro in which a list of commands is included, both Geant4 built-in commands - such as the setting of verbosity and of visualization attributes[2] -

[2] See "List of built-in commands", Section 7.1 of "Geant4 User's Guide for Application Developers", reference in Note 1.

and user-defined commands - such as detector and generator configuration parameters (see Note 4 and Note 7, and examples at page 115). The macro file is then passed as argument at the program execution.

```
  if(argc!=1) // Batch mode
    {
     G4String command = "/control/execute ";
     G4String fileName = argv[1];
     UI->ApplyCommand(command+fileName);
    }
```

This solution has been adopted when executing the ITEP application. The advantage is that parameters can be changed at execution time, with no need of re-compiling the source code.

Visualization is managed and initialized via the *VisManager*:

```
G4VisManager* visManager = new G4VisExecutive;
visManager->Initialize();
```

If any visualization interface has been defined, the *VisManager* has to be deleted at the end of the program:

```
delete visManager;
```

The procedure of deleting the *RunManager*

```
delete runManager;
```

terminates the simulation.

A.2 Geometry: *ItepDetectorConstruction*

This section goes into details of the Mandatory User Class *ItepDetector Construction* defined for the ITEP application.

The basic idea when building the geometry in Geant4 can be depicted with the concept of "Chinese box": volume elements are a series of **nested boxes**, responding to a fixed hierarchy that calls "mother volume" the outer one, the container, representing the Universe, that is the experimental hall, and "daughter volumes" the inner ones. This technique of nested volumes allows to easy specify the coordinate system for the simulation. The origin of the frame of reference is placed at the very centre of the mother volume, and for each daughter volume the position relative to the mother has to be defined.

The other important point to underline is that *DetectorConstruction* comes in two phases: logical volumes and physical volumes.

The first step is the building of **logical volumes**, that means pure geometry, with some physical properties, but without a concrete placement in the experimental hall. To select the shape, one can choose from a detailed catalog, that includes fundamental elements, as parallelepipeds, instances of the toolkit class *G4Box*, or cylinders, instances of the toolkit class *G4Tubs*. More complex elements can be designed, covering the possibility of reproducing every precise detail in a particle detector.

Once that the shape is build, the logical volumes are completed with constructive

details (materials) and the definition of sensitive regions in the detector, that are elements able to register the passage of particles and to collect data.

Physical volumes are evolution of logical volumes when physical information on position (placement and rotation) is added. This allows to move from a generic description to the concrete punctual geometry of the particular application one wants to implement.

The case of the the ITEP test beam geometry is rather simple, since elements to be reproduced consist only on a water tank and a collimator, realized as a lead screen with a circular hole, the screen thick enough to stop particles that pass outside the hole. Everything has to be placed inside the mother volume that represents the Experimental Hall.

Materials - Since Geant4 is suitable for very advanced detector simulations, it admits the possibility to select a very large number of materials, including both elements and compounds. In our case, the point is easy, because we are considering a schematic simulation in which we have vacuum in the Experimental Hall (the mother volume), simply water in the tank (no details on water salinity are included) and a lead screen with a vacuum hole to collimate the proton beam.
Going into details of the *ItepDetectorConstruction* source file, let's check how different materials are implemented in the code.

Elements → elements definition is required to build up materials:

```
  G4Element* H = new G4Element("Hydrogen","H",z=1.,a=1.01*g/mole);
  G4Element* O = new G4Element("Oxygen","O",z=8,a=16.00*g/mole);
  G4Element* N = new G4Element("Nitrogen","N", z=7.,a=14.01*g/mole);
```

Water → material "Water" is a mixture of 2 components, Element "Hydrogen" and Element "Oxygen", added in the standard proportion. The material density is fixed at the ideal value of 1 g/cm^3.

```
  density = 1.000*g/cm3;
  G4Material* H2O = new G4Material("Water", density, ncomponents=2);
  H2O -> AddElement(elH, natoms=2);
  H2O -> AddElement(elO, natoms=1);
```

Alternatively, NIST[3] data are available in Geant4 and materials can be uploaded from the database. For instance:

```
#include "G4NistManager.hh"
  G4Material* H2O = G4NistManager::Instance()->FindOrBuildMaterial("G4_WATER");
```

Vacuum → material "Vacuum" is material "Air" at very low density. "Air" is defined as a mixture of Element "Nitrogen" and Element "Oxygen" in standard proportion, defined through the fraction-mass parameter.

[3]NIST, National Institute of Standards and Technology, `http://www.nist.gov/`

```
G4Material* air = new G4Material("Air", density= 1.290*mg/cm3, ncomponents=2);
air->AddElement(N, fractionmass=0.7);
air->AddElement(O, fractionmass=0.3);

G4Material* vacuum = new G4Material("Vacuum", density= 1.e-5*g/cm3,
    ncomponents=1, kStateGas, STP_Temperature, 2.e-2*bar);
vacuum->AddMaterial(air, fractionmass=1.);
```

Lead → material "Lead" is made up with standard atomic lead.

```
G4Material* Pb = new G4Material("Lead", z= 82., a= 207.2*g/mole,
    density= 11340*kg/m3);
```

Volumes - This paragraph shows in details the constructing of volumes for the ITEP application. As already underlined, the geometry is kept simple and schematic.

Mother Volume → The following lines construct the mother volume:

```
G4double mother_x = 0.6*m;
G4double mother_y = 0.3*m;
G4double mother_z = 0.3*m;
// -- shape: BOX
G4Box* mother_box = new G4Box("mother_box",mother_x,mother_y,mother_z);
// -- logical volume: materials added
mother_log = new G4LogicalVolume(mother_box,Vacuum,"mother_log",0,0,0);
// -- physical volume: placement
mother_phys = new G4PVPlacement(0,G4ThreeVector(),mother_log,"mother",0,
    false,0);
```

In creating the box shape, the toolkit class *G4Box* asks for half size, and therefore the mother box is constructed with dimensions $Lx = 120\,cm$, $Ly = 60\,cm$, $Lz = 60\,cm$ (the x-axis is coincident with the beam axis). In this way, the ITEP tank can easily fit inside.
The box becomes a logical volume specifying the material ("Vacuum", in this case). No other physical properties are added, since the mother volume is a non-sensitive volume, and no magnetic field is turned on (the corresponding *G4LogicalVolume* arguments are set to 0).
Concerning the placement, the most important point to notice is that the fifth argument, that is where the containing volume has to be specified, is set to 0, and therefore it identifies the mother volume as the outermost volume. The mother volume is placed with no rotation (the first argument in *G4VPlacement* is set to 0). An empty G4ThreeVector means that it is placed with no translation: as already explained, the mother volume itself defines the frame of reference.

Water Tank → To build the water tank, the same sequence described for the mother volume is followed, that is passing through the logical volume and the physical volume.
Here notice once again that geometry is kept simple and approximated: the basin plastic walls are not considered and the simulation simply takes into account the - not realistic - case of a parallelepiped made of water, placed with no physical support inside the experimental hall and centered at the mother volume.

```
G4double basin_x = 0.4725*m;
G4double basin_y = 0.251*m;
G4double basin_z = 0.23535*m;
G4Box* basin_box = new G4Box("basin_box",basin_x,basin_y,basin_z);
basin_log = new G4LogicalVolume(basin_box,H2O,"basin_log",0,0,0);
basin_phys = new G4PVPlacement(0,G4ThreeVector(),basin_log,"basin",mother_log,
    false,0);
```

The basin dimensions are as listed in 3.2.1, with a small correction in the z extension, to take into account the fact that the tank is only 90% filled.
Is it clear from specification given to create *basin_log* that the basin volume is not made sensitive. As it will discussed below, only a restricted portion of the water tank (the *Grid*) constitutes the sensitive region.

Lead Screen and Collimators → To simulate the effect of the collimators, an easy and schematic solution is to place a lead screen just outside the water tank, right before the beam injection point. A "hole" is produced in the screen, centered at the beam axis. According to Geant volume creation criteria, this is obtained placing a cylinder made of vacuum in the lead screen, at the position where the collimator window is expected. The radius of the cylinder (*diaphragmRadius*) can be set to any values or controlled through a user-defined command in terminal[4].

```
G4double screen_x = 5.*cm;
G4double screen_y = 25.1*cm;
G4double screen_z = 23.535*cm;
G4double innerRadiusOfTheHole = 0.*cm;
G4double outerRadiusOfTheHole = diaphragmRadius;
// Screen
G4double screenCenter = -basin_x-screen_x; // screen thickness: 10 cm
G4Box* screen_box = new G4Box("screen_box",screen_x,screen_y,screen_z);
screen_log = new G4LogicalVolume(screen_box,Pb,"screen_log", 0,0,0);
screen_phys = new G4PVPlacement(0,G4ThreeVector(screenCenter,0,0),
    screen_log,"screen",mother_log,false,0);
// Hole
G4double halfhightOfTheHole = screen_x;
G4double startAngleOfTheHole = 0.*deg;
G4double spanningAngleOfTheHole = 360.*deg;
G4Tubs* hole_tube = new G4Tubs("hole_tube",innerRadiusOfTheHole,
    outerRadiusOfTheHole, halfhightOfTheHole,startAngleOfTheHole,
    spanningAngleOfTheHole);
hole_log = new G4LogicalVolume(hole_tube,Vacuum,"hole_log",0,0,0);
G4RotationMatrix* fieldRot = new G4RotationMatrix();
fieldRot->rotateY(90.*deg);
// Rotation is required to place the hole into the screen
hole_phys = new G4PVPlacement(fieldRot,G4ThreeVector(0,0,0),hole_log,"hole",
    screen_log,false,0);
```

Looking at the above lines, we can notice that the screen is placed inside the mother volume, translated in order to put it at the beam output, and centered with the beam axis. The hole is centered with the screen, thus the collimator is assumed as centered with the beam axis. The screen is thick enough to stop protons passing through it.

[4] The toolkit class *G4UIMessanger* allows to define new commands to apply in the terminal, in order to have more flexibility in modifying the detector. An instance *ItepDetectorMessenger* has been created, and the command */Itep/detector/setCollRad* has been implemented.

Sensitive Detector: Grid and Cells - So far so good, even if with some schematic descriptions, the ITEP test beam experimental setup has been reproduced. The next step is to make it a *detector*, that means a region in space able to register the passage of protons. Remembering the goal of the AcSource code, that is the computation of a map of deposited energy, water has to be made sensitive.

Ideally, what one wants is to know the energy density in each position $P \equiv (x, y, z)$ of the water tank, but this possibility is impracticable in a discrete computation. The concrete solution is to produce a sensitive grid, composed of small cubic cells, and collect the information of the amount of energy deposited inside each cell. The energy density at the position identified with the cell centre is computed dividing the total amount of energy in the cell for the cell volume. The smaller is the cell volume, the more accurate is the approximation.

Of course, the larger is the sensitive region, and the smaller are the sensitive cells, the larger is the amount of information collected and stored, and the longer is the computation time requested to complete the simulation. Since reducing the computation time is important, the first recommendation is thus avoiding to waste resources. For instance, it is no use to keep track of what happening in regions where nothing is actually happening, that is widely outside the expected range of protons in water. In other words, there is no need to make the whole water tank a sensitive detector.

The solution adopted is a cubic *Grid*, with a side of $30\,cm$, thus smaller that the whole basin, placed inside the basin, centered at the position where most of the energy is deposited. The *Grid* is then chopped in cells, and each cell is made sensitive.

Concerning the cell size, a good compromise is achieved setting the cube side at the value $0.2\,cm$. As it is explained in Section 3.4.2, this value constraints the sampling time of the simulated acoustic pulse.

Grid and cell size are specified with the user-defined commands */Itep/detector/setGridDim* and */Itep/detector/setGridNCells*, as explained in Note 4.

Going into details:

```
// GRID
G4double xGridHalfLength=15.*cm,yGridHalfLength=15.*cm,zGridHalfLength=15.cm;
G4double gridPos_x =-(basin_x-xGridHalfLength),gridPos_y = 0.*cm,
    gridPos_z = 0.*cm;
G4Box* grid_box = new G4Box("grid_box",xGridHalfLength,yGridHalfLength,
    zGridHalfLength);
grid_log = new G4LogicalVolume(grid_box,H2O,"grid_log",0,0,0);
grid_phys = new G4PVPlacement(0,G4ThreeVector(gridPos_x,gridPos_y,gridPos_z),
    grid_log,"grid",basin_log,false,0);
```

As shown in Figure 3.12, the selected grid dimensions are enough to contain most of the particles generated in the simulation.

To chop the grid in cells, the idea is to execute in sequence $N = 150$ cuts along the x, the y and the z direction. The toolkit class *G4PVReplica* is used to uniformly divide the grid.

Since the grid side is $30\,cm$, with the selected N the above cited value of $0.2\,cm$ is obtained for the cell side.

The following lines implement the division in cells.

```
// -- along x
G4double halfchop = xGrigliaHalfLength/N, chop=2*halfchop;
G4Box* slice_box = new G4Box("slice_box",halfhchop,yGrigliaHalfLength,
```

```
    zGrigliaHalfLength);
slice_log = new G4LogicalVolume(slice_box,H2O,"slice_log",0,0,0);
slice_rep = new G4PVReplica("slice_rep",slice_log,grid_log,kXAxis,N,chop,0);
// -- along z
G4Box* layer_box = new G4Box("layer_box",halfchop,yGrigliaHalfLength,halfchop);
layer_log = new G4LogicalVolume(layer_box,H2O,"layer_log",0,0,0);
layer_rep = new G4PVReplica("layer_rep",layer_log,slice_log,kZAxis,N,chop,0);
// -- along y
G4Box* chamber_box = new G4Box("chamber_box",halfchop,halfchop,halfchop);
chamber_log = new G4LogicalVolume(chamber_box,H2O,"chamber_log",0,0,0);
chamber_rep = new G4PVReplica("chamber_rep",chamber_log,layer_log,kYAxis,
    N,chop,0);
```

The last step creates the sensitive detector *aGridSD*. The procedure consists in activating as sensitive the *chamber_log* element, that is the inner portion in the volume hierarchy, as clear from the above lines.

```
chamber_log->SetSensitiveDetector( aGridSD );
```

An additional comment has to be done concerning **visualization attributes**. *SetVisAttributes* method is applied to set colors and visualization options. In particular, volumes visibility can be selected. It is important to notice that if visualization is activated, the computation time increases with the number of elements set as visible. This is why I decided to make the cells invisible, keeping the grid contour only, as implemented in the following lines:

```
slice_log->SetVisAttributes(G4VisAttributes::Invisible);
layer_log->SetVisAttributes(G4VisAttributes::Invisible);
chamber_log->SetVisAttributes(G4VisAttributes::Invisible);
```

Visualization properties can be set at the User Interface Terminal level, also.

A.3 Particles and Physics Processes in the Simulation: *ItepPhysicsList*

As already pointed out in A.1, *ItepPhysicsList* is an instance of the toolkit mandatory user class *G4VuserPhysicsList*.
Physics List is where particles and physics process to be used in the simulation must be defined, and range cut-off for all particles must be set. Different application require different Physics List, that is different physics model and different levels of approximation.
The source code used for the ITEP application is modelled on the *ExN03PhysicsList*, written for ExampleN03 and distributed with the Geant4 toolkit.

The three fundamental methods to be implemented are:

```
ConstructParticle();      // construct particles
ConstructProcess();       // construct processes and register them to particles
SetCuts();                // set a range cut value for particles
```

The *ConstructParticle()* method evokes methods for bosons, leptons, mesons and baryons construction[5].

[5]The complete list of particles included in the simulation is: Gamma, Electron, Positron,

For each particle, a list of processes has to be specified with the *ConstructProcess* method[6].
AddTransportation method is evoked to assign transportation process to each particle defined in *ConstructParticle*.

Setting cuts means fixing the low energy limit on secondary production. In Geant4 jargon, the "cut" is secondary production threshold distance. The use of the term "cut" is somehow improper, since particles are not cut out of the simulation when the lower limit in energy is reached, but they stop to produce secondaries. Geant4 asks for a threshold given as a distance. The default value, adopted in the simulation, is 1.0 mm, compatible with the size of sensitive elements in the ITEP application, that is 2.0 mm. This value is elaborated for each particle and it corresponds to different energies depending on material. If requested, the output of the simulation lists the so-called Material-Cuts Couples, as recorded in the following lines.

```
 Materials : Vacuum Lead Water
 Production cuts :  gamma 1 mm     e- 1 mm     e+ 1 mm
========= Table of registered couples ==============================
Index : 0     used in the geometry : Yes
 Material : Vacuum
 Range cuts        :  gamma 1 mm     e- 1 mm     e+ 1 mm
 Energy thresholds :  gamma 990 eV     e- 990 eV     e+ 990 eV
Index : 1     used in the geometry : Yes
 Material : Lead
 Range cuts        :  gamma 1 mm     e- 1 mm     e+ 1 mm
 Energy thresholds :  gamma 100.511 keV    e- 1.36128 MeV    e+ 1.28002 MeV
Index : 2     used in the geometry : Yes
 Material : Water
 Range cuts        :  gamma 1 mm     e- 1 mm     e+ 1 mm
 Energy thresholds :  gamma 2.90186 keV    e- 347.138 keV    e+ 338.695 keV
============================================================================
```

A.4 Beam Profile and Injection: *ItepPrimaryGeneratorAction*

The third mandatory user class is derived from the toolkit class *G4VUserPrimaryGeneratorAction*. This is the most important step in the simulation: the reproduction of the beam profile is, in fact, crucial, since it strongly determines the shape of the energy deposition, that is the acoustic source, and thus the acoustic pulse.

Going into details of the source code, the *GeneratePrimaries* method defines the properties of primaries and sets the values for each event: what particles are employed as primaries, the momentum direction, the injection energy of primaries, the injection vertex position. Almost each parameter of the primary generator can

MuonPlus, MuonMinus, NeutrinoE, AntiNeutrinoE, NeutrinoMu, AntiNeutrinoMu, PionPlus, PionMenus, PionZero, Eta, EtaPrime, KaonPlus, KaonMinus, KaonZero, AntiKaonZero, KaonZeroLong, KaonZeroShort, Proton, Antiproton, Neutron, AntiNeutron

[6] In the following, the complete list of processes for each particle. Gamma: GammaConversion (e^+e^- pair production), ComptonScattering, PhotoElectricEffect. Electron and Positron: MultipleScattering, eIonisation, eBremsstrahlung. Positron only: G4eplusAnnihilation. MuonPlus and MuonMinus: MultipleScattering, MuBremsstrahlung, MuPairProduction (e^+e^- pair production), MuIonisation. Charged Hadrons: MultipleScattering and hIonisation. Where applicable: Decay.

be controlled through user-defined commands, specified in the execution macro[7].

```
void ItepPrimaryGeneratorAction::GeneratePrimaries(G4Event* anEvent)
{ // Momentum Direction (Unit Vector)
  G4ThreeVector v(1.0,0.0,0.0); // (v_x,v_y,v_z)
  // Selecting protons as primaries and extracting particle properties
  G4ParticleTable* particleTable = G4ParticleTable::GetParticleTable();
  G4String particleName;
  G4ParticleDefinition* pcledef = particleTable->FindParticle(particleName =
      "proton");
  G4double charge = pcledef->GetPDGCharge();
  G4double mass   = pcledef->GetPDGMass();
  // Kinematics
  G4double Kinergy = inj_energy; // inj_energy can be set at 100 MeV or 200 MeV
  G4double Energy = Kinergy + mass;
  G4double Momentum = sqrt(Energy*Energy-mass*mass);
  G4ThreeVector P = v*Momentum;
  // * BEAM PROFILE *
  // Extracting the injection vertex for each proton in the beam
  double Xfix = -60.*cm; // (at the edge of the mother volume)
  for(int i =0; i<NofVertex;i++) // NofVertex=10^5
    { G4double percent = G4UniformRand();
      G4double rndY =0;
      G4double rndZ =0;
      if(percent<= |fraction|) // Gaussian1
        { rndY = G4RandGauss::shoot(0,sigma_y1);
          rndZ = G4RandGauss::shoot(0,sigma_z1);
        }
      else                     // Gaussian2
        { rndY = G4RandGauss::shoot(0,sigma_y2);
          rndZ = G4RandGauss::shoot(0,sigma_z2);
        }
      G4ThreeVector vertex_pos(Xfix,rndY,rndZ);
      G4PrimaryVertex* vertex = new G4PrimaryVertex(vertex_pos,0.);
          // (vertex pos., time)
      G4PrimaryParticle* particle = new G4PrimaryParticle(pcledef,P[0],P[1],P[2]);
      particle->SetMass(mass);
      particle->SetCharge(charge);
      vertex->SetPrimary(particle);
  // generated vertexes add up to constitute the Event
      anEvent->AddPrimaryVertex(vertex);
    }
}
```

Protons are selected as primary particles. The momentum is calculated from kinematics, direction is specified by the unit vector v, that is constant for each proton and along the x axis.
The beam profile simulation consists in the extraction of the injection vertex for each primary proton in the beam, that is the position from which the proton starts its track, entering the water tank with the momentum specified above, moving along the x axis.
The x coordinate of the vertex is fixed at the mother volume edge, behind the lead screen. The y and z coordinates are extracted according to the model, that is assumed, both in y and in z, as a convolution of two Gaussian distributions. The Gaussian distributions are centered in 0, at the beam axis, and the σ parameters (σ_{y1}, σ_{y2}, σ_{z1}, σ_{z2}) have to be specified. In addition the model requires the setting of a "fraction", that is a number between 0 and 1 expressing the percentage of

[7] Analogous to the case described in Note 4, the instance *ItepPrimaryGeneratorMessaenger* has been implemented, with a list of setting commands, as */Itep/generator/setSigma*, */Itep/generator/setKinergy*, */Itep/generator/setNofVertex*, */Itep/generator/setFraction*.

occurrence of Gaussian1 over Gaussian2. As shown in the lines above, a uniform random extraction (*percent*) decides which of the two Gaussian has to be selected for the vertex position extraction. If Gaussian1 is selected, y coordinate is extracted according to a Gaussian with $\sigma = \sigma_{y1}$ and z coordinate is extracted following a Gaussian distribution with $\sigma = \sigma_{z1}$. σ_{y2} and σ_{z2} come into play when the extracted *percent* value corresponds to Gaussian2. Of course, the model can be reduced to a simple Gaussian distribution setting $fraction = 1$.
In my investigations, sigma values are set assuming symmetry in y and z, but the code is implemented to accept also a beam profile with $\sigma_y \neq \sigma_z$.
In the following, I will define an index n to indicate different beam profiles. Each n corresponds to a set of three numbers (σ_1, σ_2, p, where p is the selected fraction value). Detailed investigations on how different selections in the beam profile set of parameters affect the pulse shape in the simulation is examined in Section 3.6.2.

Simulation is in three dimensions (space-simulation). Time dimension is excluded, since instantaneous energy deposition hypothesis is assumed, as specified in the line that defines the *G4PrimaryVertex*.

A.5 Optional User Classes: *ItepEventAction*, *ItepGridSD*, *ItepGridHit*

Mandatory User Classes are what needed to build an application and to make the simulation work. But simulation results cannot be used further[8] if information on particle tracking is not opportunely collected and stored. Optional User Classes thus come to help.

Analogous to the definition given when describing the ITEP test beam data (see Section 3.2.3, page 51), an **event** in the simulation is a single occurrence of the phenomenon of the proton beam injection into the water tank. Since the structure of the simulation is rather simple, each **run** consists of one event only, and therefore no particular operation is requested at the *RunAction* level.

The *G4UserEventAction* level, on the contrary, is implemented with the ITEP application instance *ItepEventAction*. It is where the managing of the output file is performed.
The class has two main methods, *beginOfEventAction()* and *endOfEventAction()*. This last method, in particular, has been exploited to set options for the creation of the output file, as the output file name and the list of quantities to include in the output file.

Information recorded in the output file at the *EventAction* level comes from the HitCollection, that is where details on the step-by-step simulation are stored. This object is evoked via *ItepGridSD*, that is an instance from the abstract base class *G4VSensitiveDetector* defining the proprieties of the Sensitive Detector. The three main methods are *Initialize*, *ProcessHits* and *EndofEvent*.

The *Initialiaze* method creates a **HitCollection** associated with the Sensitive Detector "Grid".

[8] A note to remember that the purpose of this first AcSource stage in the simulation chain is to produce an energy deposition map to be used as acoustic source, in order to get an input for the next step in the simulation chain, AcPulse.

```
gridCollection = new ItepGridHitsCollection(SensitiveDetectorName,
    collectionName[0]);
```

ProcessHits is responsible for extracting and storing **physics** and **geometry** information into Hits.

A G4Step in Geant4 is a physics process occurring in the Sensitive Detector. For each G4Step in the simulation, G4Track identifies the particle involved in the process. Every particle generated or created in the full simulation has its own track identification number. Physic information is transferred to each newHit through set methods:

```
ItepGridHit* newHit = new ItepGridHit();
newHit->SetTrackID  (aStep->GetTrack()->GetTrackID());
newHit->SetEdep     (aStep->GetTotalEnergyDeposit());
```

"newHit" is an object of type *ItepGridHit*, derived from the abstract base class *G4VHit*. The point is that the user can build her/his own hit type for each sensitive region in the detector. The advantage is that the list of information recorded and stored in the simulation is a user-defined property, suitable for the specific application one wants to implement.
In my case, I defined the following list: track identification number (track ID), chamber identification number (chamberNb), layer identification number (layerNb), slice identification number (sliceNb), cell volume (cellVol), cell position (cellPos), energy deposited into the cell (Edep).

Information on geometry are collected through G4Touchable. A G4Touchable is a geometrical entity with a unique placement in the detector. It allows to identify each sensitive cell and to distinguish each replica in the grid. Set methods transfer information from G4Touchable to G4Hit.

```
const G4VTouchable *touchable = aStep->GetPreStepPoint()->GetTouchable();
newHit->SetChamberNb(touchable->GetReplicaNumber(0));
newHit->SetLayerNb(touchable->GetReplicaNumber(1));
newHit->SetSliceNb(touchable->GetReplicaNumber(2));
```

Numeric argument in *GetReplicaNumber* identifies the hierarchic level in the grid construction.

Information given as cell identification number has to be changed into cell coordinates in order to get the cell position geometry. This operation is essential in order to build the energy map.

```
G4double XCell = touchable->GetTranslation().x()/cm;
G4double YCell = touchable->GetTranslation().y()/cm;
G4double ZCell = touchable->GetTranslation().z()/cm;
G4ThreeVector position(XCell,YCell,ZCell);
newHit->SetCellPos(position);
```

To get physical properties of the cell, such as the cell volume, the touchable has to be made "solid":

```
G4Box *touchable_solid = (G4Box*)touchable->GetSolid();
G4double vol = touchable_solid->GetCubicVolume()/cm3;
newHit->SetCellVol(vol);
```

Since both physical and geometrical information have been stored into the hit, the last action in the *ProcessHit* method is to insert the newHit into the HitCollection:

```
gridCollection->insert(newHit);
return true;
```

EndofEvent method is evoked at the end of the event. The only operation asked at this stage is to compute the statistics of hits recorded in the HitCollection:

```
G4int NbHits = gridCollection->entries();
```

A.6 G4Simulation Output: the Energy Deposition Map file *rhoEmap*

The simulation run is guided through a macro file (see page 111) where built-in and user-defined commands are specified, as pointed out in Note 2, 4 and 7.

Concerning user-defined commands, they allow to set detector and generator parameters. Lines below are extracted from ITEP.mac macro file.

```
# -- ITEP detector commands
/Itep/detector/setGridDims 15 15 15
/Itep/detector/setGridCells 150 150 150
/Itep/detector/setCollRad 2.5 cm
/Itep/detector/update
# -- ITEP generator commands:
/Itep/generator/setNofVertex 10000
/Itep/generator/setKinergy 200 MeV
/Itep/generator/setSigmaY1 1.00 cm
/Itep/generator/setSigmaZ1 1.00 cm
/Itep/generator/setSigmaY2 2. cm
/Itep/generator/setSigmaZ2 2. cm
/Itep/generator/setFraction 50
/Itep/generator/update
```

From the above settings, the Grid is a cube with a 30 cm side. 150 cuts are operated along x, y and z, obtaining thus a cell side of 0.2 cm. Collimator diameter is set at 5 cm. For what concerns the primary generator, selected values for sigma parameters and fraction correspond to the beam profile identified with $n = 3$ (see Table 3.1).

Setting tracking verbosity level "/tracking/verbose 1", the output of the simulation prints out a detailed report on each G4Track generated during the run. In Appendix B, I report some extracts from the output, pointing out significant parts and evidencing the connections with elements accounted in this Chapter.

A sample of the G4OutputFile of the AcSource code, written as defined in *ItepEventAction*, is in the following lines:

```
trackID cellID   zID yID xID Edep      x     y    z   V
...
99988   215598   78  74  2   1.01324  -46.75 0.7 -0.1 0.008
99988   305598   78  74  3   1.1626   -46.55 0.7 -0.1 0.008
...
99988   11465595 75  74  127 12.8442  -21.75 0.1 -0.1 0.008
99987   35119    79  73  0   0.883224 -47.15 0.9 -0.3 0.008
99987   125119   79  73  1   0.95753  -46.95 0.9 -0.3 0.008
...
```

Concerning the file format: *trackID* is track identification number; *cellID* is cell identification number; *zID* is layer identification number; *yID* is chamber identification number; *xID* is slice identification number; *Edep* is the amount of energy, in MeV, that particle identified by trackID releases into the cell; x is the x-coordinate of the cell centre (in cm); y is the y-coordinate of the cell centre (in cm); z is the z-coordinate of the cell centre (in cm); V is the cell volume, in cm^3.
Comments: *cellID* is obtained combining *xID*, *zID*, *yID* in order to get a unique identification number, different for each of the $Ncell = 150^3$ cells that constitute the grid; cells are all the same in size, therefore V is always the same.

It is clear from the lines reported above (and from extracts of G4Track Information in Appendix B) that the Geant4 Simulation follows each particle track in its propagation through the sensitive detector, registering if something (an interaction) is occurring, causing an energy loss.

The G4OutputFile is not an energy deposition map, yet, therefore further processing is needed. In particular, we are not interested in which particle (trackID) is releasing energy in the sensitive detector, but in *where* (cellID) the energy deposition is occurring and in *how much* is the total amount of energy released in each cell. In other words, in order to build the Energy Deposition Map, we have to add up energy deposition occurrences happening in the same sensitive element (cell) of the sensitive detector (grid), forgetting information about tracks.

The OutputMaker.cc code has been written to elaborate the G4OutputFile and to produce the Energy Deposition Map requested as input for the AcPulse stage. Information is encoded according to the format showed below, where *rhoE* is computed, for each cell, as a fraction of *Edep* over V.

```
cellID rhoE    x      y    z
...
33672  4978.61 -47.15 -0.5 -0.9
33673  12644.6 -47.15 -0.3 -0.9
33674  15433.9 -47.15 -0.1 -0.9
33675  13453.2 -47.15  0.1 -0.9
...
```

This file format points out the importance given to the grid, rather than to particles. It is much more easy to manipulate and it is the way information is passed as a *rhoEmap* at the next stage of computation, AcPulse.

Appendix B

Investigating the ITEP Monte Carlo

Output of the Geant4 Simulation

The output here discussed has been produced running the ITEP application with detector and generator settings specified in Section A.6. The only difference is in the NofVertex parameter, that here is put at the value 10, in order to speed up the computation.

The first information is a list of generated primary particles. For each primary proton, the PrimaryVertex (X, Y, Z, time) is given, computed according prescriptions described in Section A.4. The X coordinate is fixed and the time coordinate is always zero, because beam profile in time is assumed instantaneous. Y and Z values are extracted according to the beam profile model specified in the generator settings. Concerning the momentum, it is always along the x axis.

```
10 vertices passed from G4Event.
[...]
G4PrimaryTransformer::PrimaryVertex (-600(mm),-2.8958(mm),39.7114(mm),0(nsec))
Primary particle (proton) --- Transfered with momentum (644.445,0,0)
G4PrimaryTransformer::PrimaryVertex (-600(mm),12.7595(mm),-12.371(mm),0(nsec))
Primary particle (proton) --- Transfered with momentum (644.445,0,0)
[...]
```

Since the diaphragm radium is set at 2.5 cm, if Y or Z are extracted greater that this value, the generated proton is outside the collimator windows and is stopped in the lead screen without reaching the water tank. This is the case of the first particle in the list above. From G4Track Information, we see it is identified with TrackID=4. Its ParentID is 0 since it is a primary particle. Following in details its destiny through the volume defined in the ITEP application, we see that its path is composed of 11 steps. Transportation process is responsible of leading it from the the vacuum mother volume to the screen boundary. This first step length is 2.75 cm, that, Remembering the ITEP geometry details (Section A.2), corresponds to the vacuum space between the mother edge and the screen edge. Once that the proton enters the lead screen, it keeps moving inside the screen, and it does not reach the water tank, loosing all its energy because of hadronic ionization processes.

```
*****************************************************************************
* G4Track Information:   Particle = proton,   Track ID = 4,   Parent ID = 0
*****************************************************************************
Step#  X(mm) Y(mm) Z(mm) KinE(MeV)  dE(MeV) StepLeng TrackLeng NextVolume ProcName
    0  -600  -2.9   39.7    200        0        0         0   mother initStep
    1  -572  -2.9   39.7    200 0.000162     27.5      27.5   screen Transport
    2  -562  -2.5   40      171       29     10.9      38.4   screen hIoni
    3  -553  -2.59  40.6    146     24.7     8.83      47.3   screen hIoni
    4  -546  -3.07  42      122     24.1     7.15      54.4   screen hIoni
    5  -540  -3.9   42.9    102     20.5     5.67      60.1   screen hIoni
    6  -536  -4.81  43.8    81.5    20.2     4.56      64.6   screen hIoni
    7  -532  -5.33  44.3    63.5    18.1     3.59      68.2   screen hIoni
    8  -530  -5.55  44.6    46.7    16.7     2.83      71.1   screen hIoni
    9  -527  -5.46  44.8    29.2    17.5     2.21      73.3   screen hIoni
   10  -526  -5.53  45.3    9.96    19.3     1.52      74.8   screen hIoni
   11  -526  -5.56  45.3    0       9.96    0.306      75.1   screen hIoni
```

The next case is TrackID=5, that is still a primary proton. In this case, extracted injection vertex is so that the particle passes through the hole in the lead screen and enters the water tank. From this step on, it keeps moving through the sensitive cells of the grid, because of transportation processes. In most of the cases, the step length is 2 mm, that corresponds to the geomtric boundary of the cell[1].

For what concern energy loss (dE), the case is coherent with the expected Bragg peak behaviour, as described in Section 3.1.1: a small amount of energy is lost along the proton path, the energy loss increase as instantanoeus kinetic energy decreases (Equation 3.1). Most of the energy deposition occurs at the end of the path, at the Bragg peak. The position where the proton stops is at X=-22.0 cm. This value corresponds to a distance from the water tank edge of 25.25 cm, compatible with the range value calculated from the Simplified Physical Model illustrated in Section 3.1.1.

```
*****************************************************************************
* G4Track Information:   Particle = proton,   Track ID = 5,   Parent ID = 0
*****************************************************************************
Step#  X(mm) Y(mm) Z(mm) KinE(MeV)  dE(MeV) StepLeng TrackLeng NextVolume ProcName
    0  -600  12.8 -12.4     200        0        0         0      mother initStep
    1  -572  12.8 -12.4     200        0     27.5      27.5        hole Transport
    2  -472  12.8 -12.4     200 0.000202      100       128 chamber_rep Transport
    3  -470  12.8 -12.4     199    0.897        2       130 chamber_rep Transport
    4  -468  12.8 -12.4     198    0.827        2       132 chamber_rep Transport
    5  -466  12.8 -12.4     197    0.881        2       134 chamber_rep Transport
    6  -466  12.8 -12.4     197    0.324    0.809       134 chamber_rep hIoni
:--- List of 2ndaries - #SpawnInStep=1(Rest=0,Along=0,Post=1), #SpawnTotal=  1 ---
    :  -466  12.8  -12.4   0.412                e-
    :-------------------------- EndOf2ndaries Info ---------------------------
    7  -464  12.8  -12.4    196     0.69     1.19       136 chamber_rep Transport
    8  -462  12.8  -12.4    195    0.864        2       138 chamber_rep Transport
    9  -460  12.7  -12.4    194      0.9        2       140 chamber_rep Transport
[...]
  129  -228  16.1  -13.6    30.3     3.55        2       372 chamber_rep Transport
  130  -226  16    -13.6    26.4     3.97        2       374 chamber_rep Transport
  131  -226  16    -13.6    25.5    0.845    0.365       374 chamber_rep Transport
  132  -224  15.9  -13.7    21.6     3.91     1.64       376 chamber_rep Transport
  133  -222  15.8  -13.7    16.2      5.4        2       378 chamber_rep Transport
  134  -221  15.8  -13.7    8.83     7.39      1.9       379 chamber_rep hIoni
  135  -220  15.8  -13.7    8.36    0.468   0.0989       380 chamber_rep Transport
  136  -220  15.8  -13.7       0     8.36    0.886       380 chamber_rep hIoni
```

[1]The StepLength is limited by a physics process occurrance or if a geometric boundary is reached.

In addition, we see that TrackID=4 produces a secondary electron, identified with TrackID=11. ParentID points at the proton track we have described already. Details on the secondary electron path are listed in the following.

```
*********************************************************************************
* G4Track Information:   Particle = e-,   Track ID = 11,   Parent ID = 5
*********************************************************************************
Step#  X(mm) Y(mm) Z(mm) KinE(MeV) dE(MeV) StepLeng TrackLeng NextVolume ProcName
    0  -466  12.8   -12.4    0.412        0        0         0 chamber_rep initStep
    1  -466  12.8   -12.4    0.39    0.0224   0.0948   0.0948 chamber_rep msc
    2  -466  12.8   -12.4    0.361   0.0292   0.0948     0.19 chamber_rep msc
    3  -465  12.9   -12.3    0.342   0.019    0.0948    0.284 chamber_rep msc
    4  -465  13     -12.3    0.318   0.0234   0.0948    0.379 chamber_rep msc
    5  -465  13.1   -12.3    0.298   0.0203   0.0948    0.474 chamber_rep msc
    6  -465  13.1   -12.2    0.273   0.0253   0.0948    0.569 chamber_rep msc
    7  -465  13.2   -12.2    0.242   0.0304   0.0948    0.664 chamber_rep msc
    8  -465  13.3   -12.2    0.22    0.0219   0.0948    0.759 chamber_rep msc
    9  -465  13.4   -12.2    0.202   0.0186   0.0948    0.853 chamber_rep msc
   10  -465  13.5   -12.2    0.182   0.0202   0.0948    0.948 chamber_rep msc
   11  -465  13.5   -12.2    0.153   0.0282   0.0948     1.04 chamber_rep msc
   12  -465  13.6   -12.1    0.125   0.0288   0.0948     1.14 chamber_rep msc
   13  -465  13.6   -12.1    0.0727  0.0519   0.0948     1.23 chamber_rep msc
   14  -465  13.6   -12.1         0  0.0727   0.0829     1.32 chamber_rep eIoni
```

Appendix C

AcPulse code

The code included is the full AcPulse.c source code, as it has been used in the simulation chain for the Itep Test Beam Application.

Detailed comments can be found in Chapter 3, Section 3.4.2.

```
// ------------------------------------------------------------------------
// Giulia De Bonis
// 20/03/2008
// (rev1.0 25/08/08)
//
// AcPulse code computes the Acoustic Pulse from an input rhoEmap.
//
// rhoEmap comes from AcSource.
// AcSource is Geant4 Monte Carlo Simulation of the ITEP Test Beam.
// ------------------------------------------------------------------------
#include <stdio.h>
#include <stdlib.h>
#include <math.h>

#define PI          3.1415926536

double RoundDouble (const double theNumber)
{
  return floor (theNumber + 0.5);
}
// This function allows an univocal managing of rounding operation.

// *************************** Declarations ******************************//
int    ii,jj,kk; // loop indexes

double xH,yH,zH; // Hydrophone Position

double Dcm2m,EMJ,DIMfact; // unit conversion factors

double v; // sound speed

double grid;

// Integration Parameters
double Rmin,Rmax,rstep,Tmin,Tmax,tstep;
int    nbinR,nbinT,N,M;

// rhoEmap
double Xmin,Xmax,Ymin,Ymax,Zmin,Zmax; // rhoEmap size
int    nX,nY,nZ;
int    nline;
```

```
double ***rhoE; // energy density

double E,V,x,y,z;
int    dum1,dum2,dum3;
int    i,j,k;

int    iR,itheta,iphi,iZ,iX,iY;
double R=0.,T=0.,theta=0.,phi=0.;
double thetamax=-1.0e10,thetamin=1.0e10,phimax=-1.0e10,phimin=1.0e10;

double F=0.,Fprev=0.,pulse=0.;
double pmax=-1.0e10,pmin=1.0e10;
double t1=0.,t2=0.;

char   InputFile[150],OutputFile[150];
FILE   *input,*output;
// ***************************** MAIN PROGRAMM ***************************//
int main(int argc,char **argv)
{
// ************************** Input Selection **************************//
  if (argc==1)
     {
       printf(" Specify the input file (including the complete path)\n");
       printf(" USAGE - type: ./AcPulse InputFileName\n");
       return 0;
     }

   if(argc!=1)
    {
      sprintf(InputFile,argv[1]);
      //* InputFile *//
      printf("\nInputFile: %s\n",InputFile);
    }
// ************************* Hydrophone Selection ************************//
  // Hydrophone Position [cm]
  xH = -21.75;
  yH =10.5;
  zH = 0.;
  printf ("Selected Hydrophone:\n");
  printf ("    xH = %lf\n",xH);
  printf ("    yH = %lf\n",yH);
  printf ("    zH = %lf\n\n",zH);
//****************************** Parameters *******************************//
  // Unit Conversion Factors
  // -----------------------
  Dcm2m   = 0.01;                       // LENGHT
  EMJ     = 1.6e-13;                    // ENERGY
  DIMfact = (EMJ)/(Dcm2m*Dcm2m*Dcm2m);  // DimFact to get Pressure in PASCAL

  // Simulation Parameters (from AcSource Monte Carlo)
  // -------------------------------------------------
  grid = 0.2; // [cm]
// rhoEmap is given over a grid divided in cubic cell.
// The cell side is the "grid" value here declared -
// it defines the spatial resolution of the simulation and
// it provides a lower constraint on the sampling time of the sim. pulse.

  // Integration Parameters
  // ----------------------
  // --> angular variables: theta, phi
  N = 1000;              // dtheta = PI/N
  M = 2000;              // dphi   = 2*PI/M

  // --> radius: R
  Rmin=0;
  nbinR=100;
  rstep=0.3; // [cm] - It cannot be lower than grid
```

```
  Rmax=Rmin+(nbinR-1)*rstep;

  printf("Integration Parameters:");
  printf("\n    Rmin  = %lf cm",Rmin);
  printf("\n    Rmax  = %lf cm",Rmax);
  printf("\n    rstep = %lf cm",rstep);
  printf("\n    nbinR = %d",nbinR);

  // --> time t connected to distance R through propagation velocity: T=R/v
  v=1500.; // [m/s]
// To compute the sampling time, v is fixed at the nominal value, and
// assumed constant (homogeneous medium).

  tstep=rstep*Dcm2m/v; //[s] - sampling time ts.
// Using the nominal value for v, ts=2.0 microseconds

  Tmin=Rmin*Dcm2m/v;
  nbinT=nbinR;
  Tmax=Tmin+tstep*nbinT;
  printf("\n    Tmin  = %.8lf s",Tmin);
  printf("\n    Tmax  = %.8lf s",Tmax);
  printf("\n    tstep = %.8lf s",tstep);
  printf("\n    nbinT = %d\n",nbinT);

  //* OutputFile *//
  sprintf(OutputFile,"AcPulses/acsig.dat");
//***************************** Initialization *****************************//
  Xmin = 1.0e10;
  Xmax = -1.0e10;
  Ymin = 1.0e10;
  Ymax = -1.0e10;
  Zmin = 1.0e10;
  Zmax = -1.0e10;
//************ Open InputFileSIM - Xmax,Xmin,Ymax,Ymin,Zmax,Zmin ************//

  if ((input = fopen(InputFile, "r")) == NULL)
    {
      printf("\nCannot open file %s\n\n",InputFile);
      printf ("\nPress ENTER to continue.\n\n");
      getchar (); // wait for input
      return(1);
    }

  printf("\n*** InputFile OPEN ****\n\n");

  nline = 0;

  while (!feof(input))
    {
    fscanf(input,"%i%lf%lf%lf%lf",&dum1,&E,&x,&y,&z);
// ! ! ! Input File format ! ! !
// Change here if rhoEmap comes from different AcSource code.
      if(x>=Xmax)Xmax=x;
      if(y>=Ymax)Ymax=y;
      if(z>=Zmax)Zmax=z;

      if(x<=Xmin)Xmin=x;
      if(y<=Ymin)Ymin=y;
      if(z<=Zmin)Zmin=z;

      nline=nline+1;
    }

  fclose(input);
// The input file is scanned to determine the acoustic source size

  printf("%i lines READ\n\n",nline);
```

```
  printf("    Xmax = %lf   Xmin = %lf\n",Xmax,Xmin);
  printf("    Ymax =  %lf   Ymin = %lf\n",Ymax,Ymin);
  printf("    Zmax =  %lf   Zmin = %lf\n\n",Zmax,Zmin);

  nX=RoundDouble((Xmax-Xmin)/grid);
  nY=RoundDouble((Ymax-Ymin)/grid);
  nZ=RoundDouble((Zmax-Zmin)/grid);

  printf("    nX = %d\n",nX);
  printf("    nY = %d\n",nY);
  printf("    nZ = %d\n",nZ);
//******************** Dynamical allocation of a 3D array *******************//
  rhoE = (double***) malloc((nX+1) * sizeof(double**));
  for(ii=0; ii<=nX; ii++)
    {
      rhoE[ii] = (double**) malloc((nY+1) * sizeof(double*));
      for(jj=0;jj<=nY;jj++)
        rhoE[ii][jj] = (double*) malloc((nZ+1) * sizeof(double));
    }
// rhoE[nX+1][nY+1][nZ+1]=[0...nX][0...nY][0...nZ]
//*************************** rhoE Initialization ***************************//
  if(rhoE!=NULL)
    {
      for(ii=0;ii<=nX;ii++)
        {
          for(jj=0;jj<=nY;jj++)
            {
              for(kk=0;kk<=nZ;kk++) rhoE[ii][jj][kk]=0; // INITIALIZATION
            }
        }
    }
  else
    {
      printf("rhoE not allocated\n");
      printf ("\nPress ENTER to continue.\n\n");
      getchar (); // wait for input
      return(1);
    }
//***************** Open InputFileSIM - Filling the rhoE array **************//
  if ((input = fopen(InputFile, "r")) == NULL)
    {
      printf("\nCannot open file %s\n\n",InputFile);
      printf ("\nPress ENTER to continue.\n\n");
      getchar (); // wait for input
      return(1);
    }

  while (!feof(input))
    {
      fscanf(input,"%i%lf%lf%lf%lf",&dum1,&E,&x,&y,&z);
      i=RoundDouble((x-Xmin)/grid);
      j=RoundDouble((y-Ymin)/grid);
      k=RoundDouble((z-Zmin)/grid);
      rhoE[i][j][k]=E;
    }
  fclose(input);
  printf("\n*** InputFile CLOSED ****\n");
//***************************** Open OutputFile *****************************//
//******* Sum over spherical surface, difference quotient, --> ACPULSE ******//
  if ((output = fopen(OutputFile, "w")) == NULL)
    {
      printf("\nCannot open file %s\n\n",OutputFile);
      printf ("\nPress ENTER to continue.\n\n");
      getchar (); // wait for input
      return(1);
    }
```

```
  printf("\n*** OutputFile: %s ****\n",OutputFile);
  printf("\n*** OutputFile OPEN ****\n");

// Sum over spherical surfaces, radius R, centered at the hydrophone position
  for (iR=0;iR<nbinR;iR++)
    {
      R=Rmin+rstep*iR; //
      T=Tmin+tstep*iR; // T=R/v
      F=0.; // initialization of the sum value
      printf("\n R=%lf\tT=%.8lf",R,T);
      for (itheta=0;itheta<=N;itheta++)
        {
          theta = PI*itheta/N; // theta assumes (N+1) values from 0 to PI
          iZ = 1+RoundDouble((zH + R*cos(theta)-Zmin)/grid);
          if ((iZ>nZ)||(iZ<=0)) continue;
          for (iphi=0;iphi<=M;iphi++)
            {
              phi = 2*PI*iphi/M;  // phi assumes (N+1) values from 0 to 2*PI
              iX = 1+RoundDouble((xH + R*sin(theta)*cos(phi)-Xmin)/grid);
              if ((iX>nX)||(iX<=0)) continue;
              iY = 1+RoundDouble((yH + R*sin(theta)*sin(phi)-Ymin)/grid);
              if ((iY>nY)||(iY<=0)) continue;
              // rhoE[iX][iY][iZ]=q(R,itheta,iphi) is energy density
              F = F + (rhoE[iX][iY][iZ])*sin(theta);

              // thetamax/min e phimax/min
              // source size - angular extension (hydrophone point of view)
              if(rhoE[iX][iY][iZ]!=0.)
                {
                  if(phi>=phimax)phimax=phi;
                  if(phi<=phimin)phimin=phi;
                  if(theta>=thetamax)thetamax=theta;
                  if(theta<=thetamin)thetamin=theta;
                }
            }
        }
      // F*(PI/N)*((2.*PI)/M) = F*dtheta*dphi
      // --> JACOBIAN of the coord. transformation: (theta,phi)-->(itheta,iphi)

// DIFFERENCE QUOTIENT
      pulse = DIMfact*PI/(2.0*N*M)*(F+R*(F-Fprev)/rstep); // [Pa]
      // (from the Poisson formula)
// NOTE: The Gruneisen Coefficient GAMMA(Temperature, Salinity, Depth)
//       has to be taken into account to compute the signal amplitude
//       as a function of environmental parameters: pulse=GAMMA*pulse;

      printf("\tp=%lf\n",pulse);
      fprintf(output,"%.8lf %lf\n",T,pulse);
      Fprev=F;

    // Search for pmax/pmin
      if(pulse>=pmax)
        {
          pmax=pulse;
          t1=T;
        }
      if(pulse<=pmin)
        {
          pmin=pulse;
          t2=T;
        }
    }

  fclose(output);
  printf("\n*** OutputFile CLOSED ****\n\n");
  free(rhoE);
```

```
//************************* END of MAIN PROGRAM ************************//

   printf("----------------------\n");
   printf("|*** END OF PROGRAM ***|\n ----------------------\n");
   printf("\nPress ENTER to continue\n\n");
   getchar (); // wait for input


   return 0;
}

// **** END of MAIN PROGRAMM ****
```

Bibliography

[1] F. Halzen. Multi-messenger astronomy: Cosmic rays, gamma-rays, and neutrinos. e-Print: arXiv astro-ph/0302489, 2003. Presented at 21st Texas Symposium on Relativistic Astrophysics (Texas in Tuscany), Florence, Italy, 9-13 Dec 2002.

[2] M. Davier. Multi-Messenger Astronomy. In J. Dumarchez, Th. Patzak, and F. Vannucci, editors, *NEUTRINO 2004. Proceedings of the XXIst International Conference on Neutrino Physics and Astrophysics*, volume 143 of *Nuclear Physics B - Proceedings Supplements*, pages 395–406, June 2005.

[3] M. Longair. *High Energy Astrophysics.* Cambridge University Press, 1992.

[4] V.S. Berezinskii, B.S. Bulanov, V.A. Dogiel, and V.S. Ptuskin. *Astrophysic of Cosmic Rays.* Edited by V.L. Ginzburg, Amsterdam: North-Holland, 1990.

[5] J. Cronin, T.K. Gaisser, and S. Swordy. Cosmic rays at the energy frontier. *Scientific American*, 276:44, 1997. Additional information about Figure 1.1 available at `http://astroparticle.uchicago.edu/archives.htm`.

[6] R. Battiston. Astro Particle Physics from Space. In P.A Shaver, L. DiLella, and A. Gimenez, editors, *Astronomy, Cosmology, and Fundamental Physics: Proceedings of the ESO/CERN/ESA Symposium Held in Garching, Germany, 4-7 March 2002*, pages 316–333, 2002. e-Print: arXiv astro-ph/0208108.

[7] A.M. Hillas. *Cosmic Rays.* Pergamon Press, Oxford, 1972.

[8] J.N. Bahcall. *Neutrino Astrophysics.* Cambridge University Press, 1989.

[9] M Fukugita and T. Yanagida. *Physics of Neutrinos - and Applications to Astrophysics.* Springer, 2003.

[10] K. Zuber. *Neutrino Physics.* CRC Press, 2004.

[11] G.G. Raffelt. Astrophysics probes of particle physics. *Physics Reports*, 333-334:593–618, 2000.

[12] S. Sarkar. New physics from ultrahigh energy cosmic rays. In *33rd International Symposium on Multiparticle Dynamics (ISMD 2003), Cracow, Poland, 5-11 Sep 2003.*, volume B35, pages 351–364. Acta Phys. Polon., 2004. e-Print: arXiv hep-ph/0312223.

[13] F.W. Stecker. Ultrahigh Energy Cosmic Rays: Old Physics or New Physics? In C. Aramo and A. Insolia, editors, *CRIS 2004 Proceedings of the Cosmic Ray International Seminars: GZK and Surroundings. Catania, Italy, May 31-June 4, 2004*, volume 136 of *Nuclear Physics B - Proceedings Supplements*, pages 309–318, 2004.

[14] T. Craig, A. Olinto, and G. Sigl. Cosmic neutrinos and new physics beyond the electroweak scale. *Phys. Rev.*, D63:055001, 2001. e-Print: arXiv hep-ph/0002257.

[15] V.A. Kuzmin and I.I. Tkachev. Ultra-high-energy cosmic rays and inflation relics. *Physics Reports*, 320:199–221, 1999.

[16] S. Sarkar and R. Toldra. The high energy cosmic ray spectrum from massive particle decay. *Nucl. Phys.*, B621:495–520, 2002. e-Print: arXiv hep-ph/0108098.

[17] A.D. Dolgov. Neutrinos in Cosmology. *Physics Reports*, 370:333–535, 2002.

[18] A.W. Strong, I.V. Moskalenko, and V.S. Ptuskin. Cosmic-Ray Propagation and Interactions in the Galaxy. *Annual Rewiew of Nuclear and Particle Science*, 57(1):285–327, 2007.

[19] M. Prouza and R. Smida. The Galactic magnetic field and propagation of ultra-high energy cosmic rays. *Astron. Astrophys.*, 410:1–10, 2003. e-Print: arXiv astro-ph/0307165.

[20] H Takami, H. Yoshiguchi, and K. Sato. Propagation of ultra-high energy cosmic rays above 10^{19} eV in a structured extragalactic magnetic field and galactic magnetic field. *Astrophys. J.*, 639:803–815, 2006. e-Print: arXiv astro-ph/0506203.

[21] X. Chi and A.W. Wolfendale. Features of the Local Galactic Magnetic Field. *J. Phys. G: Nucl. Part. Phys.*, 16:1409–1421, 1990.

[22] P. Biermann and G. Sigl. Introduction to Cosmic Rays. *Lect. Notes Phys.*, 576:1–26, 2001. e-Print: arXiv astro-ph/0202425.

[23] D. Allard, E. Parizot, A.V. Olinto, E. Khan, and S. Goriely. UHE nuclei propagation and the interpretation of the ankle in the cosmic-ray spectrum. *Astronomy & Astrophysics*, 443(3):L29–L32, 2005.

[24] K.H Kampert. Cosmic Rays from the Knee to the Ankle - Status and Prospects. In R. Caruso, R. Fonte, A. Insolia, and V. Pirronello, editors, *Proceedings of the Cosmic Ray International Seminars, Catania, Italy, May 29 - June 02, 2006*, volume 165 of *Nuclear Physics B - Proceedings Supplements*, pages 294–306, 2007. e-Print: arXiv astro-ph/0611884v1.

[25] E. Roulet, D. Harari, and S. Mollerach. The most energetic particles in the Universe. e-Print: arXiv hep-ph/0001328, 1999. Plenary talk presented by E. Roulet at COSMO99, Trieste, Oct. 1999.

[26] The Pierre Auger Cosmic Ray Observatory - Home Page. http://www.auger.org/.

[27] The Pierre Auger Collaboration (J. Abraham et al.). Correlation of the highest-energy cosmic rays with the positions of nearby active galactic nuclei,. *Astropart. Phys.*, 29:188–204, 2008. e-Print: arXiv astro-ph/0712.2843.

[28] M. Catanese et al. Multiwavelength observations of a flare from Markarian 501. *Astrophys. J.*, 487:L143–L146, 1997. e-Print: arXiv astro-ph/9707179.

[29] A.J. Castro-Tirado. Multiwavelength Observations of Gamma-Ray Bursts: towards the Understanding of the Mystery. In W. Wamsteker, R. Gonzalez Riestra, and R. Harris, editors, *Ultraviolet Astrophysics Beyond the IUE Final Archive: Proceedings of the Conference, Sevilla, Spain, 11th-14th November 1997*, volume SP-413 of *ESA Conference Proceedings*, page 659. European Space Agency, European Astronomical Society, ESA Publications Division, 1998. e-Print: arXiv astro-ph/9803007.

[30] Th.J.R. Courvoisier. What May We Learn from Multi-wavelength Observations of Active Galactic Nuclei. e-Print: arXiv astro-ph/0011090, 2000.

[31] D.J. Thompson. The Multiwavelength Approach to Unidentified Gamma-Ray Sources. *Astrophys. Space Sci.*, 297:1–7, 2005. e-Print: arXiv astro-ph/0407423.

[32] Y. Suzuki. Solar neutrinos. In C. Frohlich, M.C.E. Huber, S.K. Solanki, and R. Von Steiger, editors, *Solar Composition and Its Evolution– from Core to Corona: Proceedings of an ISSI Workshop 26-30 January 1998, Bern, Switzerland*, volume 85 of *Space Science Reviews*, pages 91–104. Springer, 1998.

[33] T.K. Gaisser. *Cosmic Rays and Particle Physics*. Cambridge University Press, 1990. (Chapter 13).

[34] The H.E.S.S. Experiment - Home Page. http://www.mpi-hd.mpg.de/hfm/HESS/.

[35] The MAGIC Experiment - Home Page. http://magic.fisica.uniud.it/, 30 November 2008.

[36] E.G. Berezhko and H.G. Volk. Hadronic versus leptonic origin of the gamma-ray emission from Supernova Remnant RX J1713.6-3946. e-Print: arXiv astro-ph/0810.0988, 2008.

[37] The MAGIC Collaboration (J. Albert et al.). Observation of gamma rays from the Galactic Center with the MAGIC telescope. *Astrophys. J.*, 638:L101–L104, 2006. e-Print: arXiv astro-ph/0512469.

[38] The MAGIC Collaboration (J. Albert et al.). MAGIC observations of the unidentified TeV gamma-ray source TeV J2032+4130. *Astrophys. J.*, 675:L25–L28, 2008. e-Print: arXiv astro-ph/0801.2391.

[39] The H.E.S.S. Collaboration (F. Aharonian et al.). HESS VHE Gamma-Ray Sources Without Identified Counterparts. e-Print: arXiv astro-ph/0712.1173, 2007.

[40] The H.E.S.S Collaboration. H.E.S.S. ICRC 2007 Contributions. 2007. To appear in the proceedings of 30th International Cosmic Ray Conference (ICRC 2007), Merida, Yucatan, Mexico, 3-11 Jul 2007. e-Print: arXiv astro-ph/0710.4057.

[41] C. Cutler and K.S. Thorne. An overview of gravitational-wave sources. In N. Bishop and S.D. Maharaj, editors, *Proceedings of the 16th International Conference on General Relativity & Gravitation: Durban, South Africa, 15-21 July 2001*, pages 72–111. World Scientific, 2001. e-Print: arXiv gr-qc/0204090.

[42] Y. Aso et al. Search method for coincident events from LIGO and IceCube detectors. *Class. Quant. Grav.*, 25:114039, 2008. e-Print: arXiv astro-ph/0711.0107.

[43] T. Pradier. Antares/Virgo Coincidences : a feasibility study. In *Proceedings of the "XXth RENCONTRES DE BLOIS - Challenges in Particle Astrophysics", 18th - 23rd May 2008, Blois (France)*, 2008. e-Print: arXiv astro-ph/0807.2567.

[44] T.K. Gaisser, F. Halzen, and T. Stanev. Particle Astrophysics with High Energy Neutrinos. *Phys. Rept.*, 258:173–236, 1995. Erratum-ibid.271:355-356, 1996. e-Print: arXiv hep-ph/9410384.

[45] F. Halzen. High Energy Neutrino Astronomy. *Physics Reports*, 333-334:349–364, 2000.

[46] J.G. Learned and K. Mannheim. High-Energy Neutrino Astrophysics. *Annu. Rev. Nucl. Part. Sci.*, 50:679–749, 2000.

[47] E. Fermi. On the origin of cosmic radiation. *Phys.Rev.*, 75:1169–1174, 1949.

[48] E. Fermi. An hypothesis on the origin of the cosmic radiation. *Nuovo Cimento*, 6(Suppl.):317–323, 1949.

[49] A.R. Bell. The Acceleration of Cosmic Rays in Shock Fronts (I and II). *Mon.Not.R.astr.Soc.*, 182:147 and 443, 1978.

[50] R.D. Blandford and J.P. Ostriker. Particle Acceleration by Astrophysical Shocks. *The Astrophysical Journal*, 221:L29–L32, 1978.

[51] F. Aharonian. Galactic sources of high energy neutrinos. e-Print: arXiv astro-ph/0702680, 2007. Invited talk at 22nd International Conference on Neutrino Physics and Astrophysics (Neutrino 2006), Santa Fe, New Mexico, 13-19 Jun 2006.

[52] E. Waxman. Extra galactic sources of high energy neutrinos. *Phys. Scripta*, T121:147–152, 2005. Presented at Nobel Symposium 2004: Neutrino Physics, Haga Slott, Enkoping, Sweden, 19-24 Aug 2004. e-Print: arXiv astro-ph/0502159.

[53] Y. Uchiyama, F.A. Aharonian, T. Tanaka, T. Takahashi, and Y. Maeda. Extremely fast acceleration of cosmic rays in a supernova remnant. *Nature*, 449:576–578, 2007.

[54] A.R. Bell. Cosmic ray acceleration in pulsar-driven supernova renmants. *Mon.Not.R.astr.Soc.*, 257:493–500, 1992.

[55] P. Slane. Particle Acceleration in Supernova Remnants and Pulsar Wind Nebulae. e-Print: arXiv astro-ph/0205481, 2002.

[56] W. Bednarek. Neutrinos from the pulsar wind nebulae. *Astron. Astrophys.*, 407:1–6, 2003. e-Print: arXiv astro-ph/0305430.

[57] The NEMO Collaboration (S. Aiello et al.). Sensitivity of an underwater Cerenkov km^3 telescope to TeV neutrinos from galactic microquasars. *Astropart. Phys.*, 28:1–9, 2007. e-Print: arXiv astro-ph/0608053.

[58] F.W. Stecker, C Done, H. Salamon, and P. Sommers. High-Energy Neutrinos from Active Galactic Nulcei. *Phys. Rev. Lett.*, 66:2697–2700, 1991.

[59] A Atoyan and C.D. Dermer. Neutrinos and gamma-rays of hadronic origin from AGN jets. *New Astron.Rev.*, 48:381–386, 2004. e-Print: arXiv astro-ph/0402646v1.

[60] F. Halzen. High energy neutrinos from the TeV Blazar 1ES 1959 + 650. *Astroparticle Physics*, 23(6):537–542, 2005.

[61] T. Piran. Gamma-Ray Bursts and the Fireball Model. *Physics Reports*, 314:575–667, 1999.

[62] E. Waxman and J. Bahcall. High Energy Neutrinos from Cosmological Gamma-Ray Bursts. *Phys. Rev. Lett.*, 78:2292–2295, 1997. e-Print: arXiv astro-ph/9701231.

[63] M. Bouwhuis. GRB satellite triggers for neutrino telescopes. *Astronomische Nachrichten*, 329(3):334–336, 2008.

[64] C. Barbot, M. Drees, Halzen F., and D. Hooper. Neutrinos Associated With Cosmic Rays of Top-Down Origin. *Phys. Lett.*, B555:22–32, 2003. e-Print: arXiv hep-ph/0205230.

[65] Z. Myers and A. Nusser. Searching for Neutrinos from WIMP Annihilations in the Galactic Stellar Disk. *Mon.Not.R.astr.Soc*, 387(4):1712–1718, 2008. e-Print: arXiv astro-ph/0804.0554.

[66] The AMANDA Collaboration (J. Ahrens et al.). Limits to the muon flux from WIMP annihilation in the center of the earth with the AMANDA detector. *Phys. Rev.*, D66:032006, 2002. e-Print: arXiv astro-ph/0202370.

[67] G. Lim (for the ANTARES Collaboration). Indirect search for Dark Matter with the ANTARES neutrino telescope. In W. de Boer and I. Gebauer, editors, *SUSY 2007 proceedings, 15th International Conference on Supersymmetry and*

Unification of Fundamental Interactions, July 26 - August 1, 2007, Karlsruhe, Germany, pages 842–845, 2007. e-Print: arXiv astro-ph/0710.3685.

[68] P. Gondolo, G. Gelmini, and S. Sarkar. Cosmic neutrinos from unstable relic particles. *Nucl. Phys.*, B392:111–136, 1993. e-Print: arXiv hep-ph/9209236.

[69] V. S. Berezinsky and A. Vilenkin. Ultra high energy neutrinos from hidden-sector topological defects. *Phys. Rev.*, D62:83512, 2000. e-Print: arXiv hep-ph/9908257.

[70] E.R. Harrison. *The Science of the Universe.* Cambridge University Press, 2000. (Chapter 20).

[71] Ryden. B. *Introduction to Cosmology.* Addison-Wesley, 2003.

[72] D. Fargion, B. Mele, and A. Salis. Ultrahigh energy neutrino scattering onto relic light neutrinos in galactic halo as a possible source of highest energy extragalactic cosmic rays. *Astrophys. J.*, 517:725–733, 1999. e-Print: arXiv astro-ph/9710029.

[73] T.J. Weiler. Cosmic ray neutrino annihilation on relic neutrinos revisited: a mechanism for generating air showers above the Greisen-Zatsepin-Kuzmin cut-off. *Astropart. Phys.*, 11:303–316, 1999. e-Print: arXiv hep-ph/9710431.

[74] E. Waxman. Can high energy neutrino annihilation on relic neutrinos generate the observed highest energy cosmic-rays? *Submitted to Astropart.Phys. in 2008*, 1998. e-Print: arXiv astro-ph/9804023.

[75] K. Greisen. End to the cosmic ray spectrum? *Phys. Rev. Lett.*, 16:748–750, 1966.

[76] G.T. Zatsepin and V.A. Kuzmin. Upper limit of the spectrum of cosmic rays. *JETP Lett.*, 4:78–80, 1966.

[77] M. Takeda et al. Extension of the cosmic-ray energy spectrum beyond the predicted Greisen-Zatsepin-Kuzmin cutoff. *Phys. Rev. Lett.*, 81:1163–1166, 1998. e-Print: arXiv astro-ph/9807193.

[78] C. Aramo and A. Insolia, editors. *CRIS 2004 Proceedings of the Cosmic Ray International Seminars: GZK and Surroundings. Catania, Italy, May 31-June 4, 2004*, volume 136 of *Nuclear Physics B - Proceedings Supplements*, 2004.

[79] The Pierre Auger Collaboration (J. Abraham et al.). Observation of the suppression of the flux of cosmic rays above $4 \cdot 10^{19}\, eV$. *Phys. Rev. Lett.*, 101:061101, 2008. e-Print: arXiv astro-ph/0806.4302.

[80] The HiRes Collaboration. Observation of the GZK cutoff by the HiRes experiment. *Phys. Rev. Lett.*, 100:101101, 2008. e-Print: arXiv astro-ph/0703099.

[81] D.B. Cline and F.W. Stecker. Exploring the Ultra High Energy Neutrino Universe. *e-Print: arXiv astro-ph/0003459*, 2000.

[82] R Gandhi et al. Ultrahigh-Energy Neutrino Interactions. *Astroparticle Physics*, 5:81–110, 1996.

[83] J.G. Learned and S. Pakvasa. Detecting tau-neutrino oscillations at PeV energies. *Astropart. Phys.*, 3:267–274, 1995. e-Print: arXiv hep-ph/9405296.

[84] The IceCube Collaboration. Preliminary design document. Available on line at: `http://www.icecube.wisc.edu/science/publications/pdd/index.php`, 2001. (Section 5 - Expected IceCube Performance). Last modified: July 13, 2007.

[85] E. Andres et al. Observation of high-energy neutrinos using Cherenkov detectors embedded deep in Antarctic ice. *Nature*, 410:441–443, 2001.

[86] M.A. Markov and I.M. Zheleznykh. On high energy neutrino physics in cosmic rays. *Nuclear Physics*, 27(3):385–394, 1961.

[87] ANTARES - Astronomy with a Neutrino Telescope and Abyss environmental RESearch - Home Page. `http://antares.in2p3.fr/`, 8 September 2008.

[88] The DUMAND Project (Deep Underwater Muon and Neutrino Detector) at University of Hawaii - Home Page. `http://www.phys.hawaii.edu/~dumand/`, 2 June 2003.

[89] Lake BAIKAL Neutrino Telescope - Home Page. `http://baikalweb.jinr.ru/`.

[90] V. The Baikal Collaboration (Aynutdinov and others). The Baikal Neutrino Experiment: status, selected physics results, and perspectives. In A. Capone, F. Lucarelli, M. De Vincenzi, and A. Morselli, editors, *RICAP07: Proceedings of the First Roma International Conference on Astroparticle Physics Roma, Italy, June 20-22, 2007.*, volume A588 of *Nucl. Instrum. Meth.*, pages 99–106, 2008.

[91] AMANDA - Antarctic Muon And Neutrino Detector Array - Home Page. `http://amanda.uci.edu/`, 9 September 2005.

[92] The IceCube Collaboration (X.W. Xu for the collaboration). Results achieved with AMANDA. In K.S. Cheng, R. Engel, Y. Ma, B. Pattison, Z. Yao, and Q. Zhu, editors, *14th International Symposium On Very High Energy Cosmic Ray Interactions (ISVHECRI 2006), 15-22 Aug 2006, Weihai, China*, volume 175-176 of *Nucl. Phys. Proc. Suppl.*, pages 401–406, 2008.

[93] IceCube Neutrino Iservatory - Home Page. `http://icecube.wisc.edu/index.php`.

[94] S.R. Klein (for the IceCube Collaboration). IceCube: A Cubic Kilometer Radiation Detector. e-Print: arXiv physics.ins-det/0807.0034, 2008. Presented at SORMA West 2008: 1th Symposium on Radiation Measurements and Applications, Berkeley, California, 2-5 Jun 2008.

[95] T. Waldenmaier (for the IceCube Collaboration). Icetop - Cosmic Ray Physics with IceCube. In A. Capone, F. Lucarelli, M. De Vincenzi, and A. Morselli, editors, *RICAP07: Proceedings of the First Roma International Conference on Astroparticle Physics Roma, Italy, June 20-22, 2007.*, volume A588 of *Nucl.Instrum.Meth.*, pages 130–134, 2008.

[96] The NESTOR Experiment - Home Page. `http://www.nestor.noa.gr/`, July, 15 2008.

[97] L.K. Resvanis (for the NESTOR Collaboration). Recent results from NESTOR. In A. Bottino, E. Coccia, J. Morales, and J. Puimedon, editors, *TAUP 2005: Proceedings of the ninth Interantion Conference on Topics in Astroparticle and Underground Physics. 10-14 September 2005, Zaragoza, Spain*, volume 39 of *J. Phys. Conf. Ser.*, pages 447–450, 2006. Also in *3rd International Workshop On NO-VE: Neutrino Oscillations In Venice: 50 Years After The Neutrino Experimental Discovery* 7-10 Feb 2006, Venice. Proceedings edited by M. Baldo Ceolin (pp. 461-474).

[98] NEMO - NEutrino Mediterranean Observatory - Home Page. `http://nemoweb.lns.infn.it/`.

[99] G. Riccobene, A. Capone, and the NEMO Collaboration. Deep seawater inherent optical properties in the Southern Ionian Sea. *Astropart. Phys.*, 27:1–9, 2007. e-Print: arXiv astro-ph/0603701.

[100] km3Net - Home Page. `http://www.km3net.org/`, 15 August 2008.

[101] U. Katz. KM3NeT: Towards a km^3 Mediterranean Neutrino Telescope. In E. Migneco, A. Capone, R. Coniglione, P. Piattelli, and P. Sapienza, editors, *Proceedings of the 2nd International Workshop on Very Large Volume: Neutrino Telescopes*, volume 567:2 of *Nucl. Instrum. Meth. A*, pages 457–461, 2006.

[102] E. de Wolf, editor. *VLVnT Workshop On Technical Aspects Of A Very Large Volume Neutrino Telescope In The Mediterrenean Sea. 5-8 Oct 2003, Amsterdam, The Netherlands.* Available on-line at `http://www.vlvnt.nl/proceedings/`, 2003.

[103] E. Migneco, A. Capone, R. Coniglione, P. Piattelli, and P. Sapienza, editors. *KM3NeT: Towards a km^3 Mediterranean Neutrino Telescope*, volume 567:2 of *Nucl. Instrum. Meth. A*, 2006.

[104] *International Workshop On Very Large Volume Neutrino Telescope For The Mediterranean Sea (VLVnT08) 22-24 Apr 2008, Toulon, France.* To be published in Nucl. Instrum. Meth. A, 2008.

[105] J.G. Learned. Alternative Techniques for High Energy Neutrino Astronomy. In *Proceedings of the XXth International Conference on Neutrino Physics and Astrophysics (Neutrino 2002), Munich, Germany, 25-30 May 2002*, volume 118 of *Nuclear Physics B - Proceedings Supplements*, pages 405–410, 2003.

[106] R. Nahnhauer. Alternative Detection Methods for Highest Energy Neutrinos. In J. Dumarchez, Th. Patzak, and F. Vannucci, editors, *Proceedings of 21st International Conference on Neutrino Physics and Astrophysics (Neutrino 2004), Paris, France, 14-19 Jun 2004*, volume 143 of *Nuclear Physics B - Proceedings Supplements*, pages 387–394, 2005.

[107] R. Nahanhauer and S. Boser, editors. *Proceedings of the International Workshop ARENA 2005, May 17-19, 2005. DESY-Zeuthen, Germany.* World Scientific, 2006.

[108] L. Thompson and S. Danaher, editors. *Proceedings of the International Workshop ARENA 2006, June 28-30, 2006, University of Northumbria, Newcastle, UK*, number 81 in Journal of Physics: Conference Series, 2007.

[109] *Proceedings of the International Workshop ARENA 2008, June 25-27, 2008, Roma University "Sapienza", Italy*, To be published in Nucl. Instrum. Meth. A, 2008.

[110] P. Privitera (for the Pierre Auger Collaboration). The fluorescence detector of the Pierre Auger Observatory and hybrid performances. In C. Aramo and A. Insolia, editors, *CRIS 2004 Proceedings of the Cosmic Ray International Seminars: GZK and Surroundings. Catania, Italy, May 31-June 4, 2004*, volume 136 of *Nuclear Physics B - Proceedings Supplements*, pages 399–406, 2004.

[111] D. Tosi et al. Simulation of a hybrid optical-radio-acoustic neutrino detector at the South Pole. e-Print: arXiv astro-ph/0811.2100, 2008. (Presented at the ARENA 2008 Workshop).

[112] J. Vandenbroucke et al. Simulation of a Hybrid Optical/Radio/Acoustic Extension to IceCube for the EHE Neutrino Detection. In R. Nahanhauer and S. Boser, editors, *Acoustic and radio EeV Neutrino detection Activities*, pages 259–264. World Scientific, 2006. Proceedings of the International Workshop ARENA 2005, DESY-Zeuthen, Germany.

[113] C. Spiering. Future high-energy neutrino telescopes. In J. Law, R.W. Ollerhead, and J.J. Simpson, editors, *Sudbury 2000, Neutrino physics and astrophysics. Proceedings of the 19th International Conference on Neutrino Physics and Astrophysics - Neutrino 2000, Sudbury, Ontario, Canada, 16-21 Jun 2000*, volume 91 of *Nucl. Phys. B Proc. Suppl.*, pages 445–452, 2001. e-Print: arXiv astro-ph/0012532.

[114] G. A. Askaryan. Excess negative charge of an electron-photon shower and its coherent radio emission. *Sov. Phys. JETP*, 14:441–443, 1962.

[115] G. A. Askaryan. Coherent Radio Emission from Cosmic Showers in Air and in Dense Media. *Sov. Phys. JETP*, 21:658, 1965.

[116] E. Zas, Halzen F., and T. Stanev. Electromagnetic pulses from high-energy showers: implications for neutrino detection. *Physical Review D*, 45(1):362–376, 1992.

[117] KASCADE Home Page. http://www-ik.fzk.de/KASCADE_home.html.

[118] D. Saltzberg et al. Observation of the Askaryan effect: coherent microwave Cherenkov emission from charge asymmetry in high energy particle cascades. *Phys. Rev. Lett.*, 86:2802–2805, 2001. e-Print: arXiv hep-ex/0011001.

[119] D. Saltzberg et al. Accelerator measurements of the Askaryan effect in rock salt: a roadmap toward Teraton underground neutrino detectors. *Phys. Rev.*, D72:023002, 2005. e-Print: arXiv astro-ph/0412128.

[120] I. Kravchenko et al. RICE limits on the diffuse ultra-high energy neutrino flux. *Phys. Rev.*, D73:082002, 2006. e-Print: arXiv astro-ph/0601148.

[121] H. Landsman and others (for the IceCube Collaboration). AURA - a radio frequency extension to IceCube. e-Print: arXiv astro-ph/0811.2520, 2008. (Presented at the ARENA 2008 Workshop).

[122] The ANITA Collaboration (S.W. Barwick et al.). Constraints on Cosmic Neutrino Fluxes from the ANITA Experiment. *Phys.Rev.Lett.*, 96:171101, 2006. e-Print: arXiv astro-ph/0512265.

[123] N.G. Lehtinen et al. FORTE satellite constraints on ultra-high energy cosmic particle fluxes. *Phys. Rev.*, D69:013008, 2004. e-Print: arXiv astro-ph/0309656.

[124] P.W. Gorham et al. Experimental limit on the cosmic diffuse ultrahigh-energy neutrino flux. *Phys. Rev. Lett.*, 93:041101, 2004. e-Print: arXiv astro-ph/0310232.

[125] C.W. James and R.J. Protheroe. The sensitivity of the next generation of lunar Cherenkov observations to UHE neutrinos and cosmic rays. e-Print: arXiv astro-ph/0802.3562, 2008.

[126] G. A. Askaryan. (title not available). *Atomic Energy*, 3, 1957.

[127] G. A. Askaryan and B. A. Dolgoshein. (title not available). In A. Roberts and R. Donaldson, editors, *Proceedings of the 1976 DUMAND Summer Workshop, Honolulu, Hawaii*, volume 160, September 1976. Preprint Fiz. Inst. Akad. Nauk.

[128] L.D Landau and I.J. Pomeranchuk. Limits of applicability of the theory of bremsstrahlung electrons and pair production at high-energies. *Original in Russian, published in Dokl. Akad. Nauk. SSSR*, 92:535–536, 1953. English translation in "The Collected Papers of L.D. Landau", Pergamon Press, New York (1965).

[129] L.D Landau and I.J. Pomeranchuk. Electron Cascade Process at Very High-Energies. *Original in Russian, published in Dokl. Akad. Nauk. SSSR*, 92:735–738, 1953. English translation in "The Collected Papers of L.D. Landau", Pergamon Press, New York (1965).

[130] A.B. Migdal. Bremsstrahlung and Pair Production in Condensed Media at High-Energies. *Phys. Review*, 103:1811–1820, 1956.

[131] V. Niess and V. Bertin. Underwater Acoustic Detection of Ultra High Energy Neutrinos. *Astropart. Phys.*, 26:243–256, 2006. e-Print: arXiv astro-ph/0511617.

[132] S.R. Klein. Bremsstrahlung and Pair Creation: Suppression Mechanisms and How They Affect EHE Air Showers. In J.F. Krizmanic, J.F. Ormes, and R.E. Streitmatter, editors, *Workshop on Observing Giant Cosmic Ray Air Showers from $> 10^{20}$ eV Particles from Space. College Park, Maryland, 13-15 November 1997*, volume 433 of *AIP Conference Proceedings*, pages 132–147, 1998. e-Print: arXiv astro-ph/9712198.

[133] G. A. Askaryan, B. A. Dolgoshein, et al. Acoustic Detection of High Energy Particle Showers in Water. *Nuclear Instruments and Methods*, 164:267–278, 1979.

[134] N.G. Lehtinen et al. Sensitivity of an underwater acoustic array to ultra-high energy neutrinos. *Astroparticle Physics*, 17:279–292, 2002.

[135] ACoRNe - Acoustic COsmic Ray Neutrino Experiment - Home Page. `http://pppa.group.shef.ac.uk/acorne.php`.

[136] F.H. Fisher and V.P. Simmons. Sound absorption in sea water. *J. Acoust. Soc. Am.*, 62:558–564, 1977.

[137] M.A. Ainslie and J.G. McColm. A simplified formula for viscous and chemical absorption in sea water. *J. Acoust. Soc. Am.*, 103:1671–1672, 1998.

[138] Malcolm J. Crocker, editor. *Encyclopedia of Acoustics*, volume Volume 1, Part IV - Underwater Sound. John Wiley & Sons, Inc., 1997. (Chapter 34 - "Introduction", by I. Dyer; Chapter 35 - "Essential Oceanography", by F.H. Fisher and P.F. Worcester; Chapter 36 - "Propagation of Sound in the Ocean", by W.A. Kuperman.).

[139] J.G. Learned. Acoustic Radiation by Charged Atomic Particles in Liquids: an Analysis. *Physical Review D*, 19(11):3293–3307, 1979.

[140] S. Bevan, S. Danaher, J. Perkin, S. Ralph, C. Rhodes, Thompson L., T. Sloan, and D. Waters. Simulation of ultra high energy neutrino induced showers in ice and water. *Astroparticle Physics*, 28:366–379, 2007.

[141] S. Boser et al. Feasibility of acoustic neutrino detection in ice: Design and performance of the South Pole Acoustic Test Setup (SPATS). e-Print: arXiv astro-ph/0807.4676, 2008.

[142] J. Vandenbroucke, G. Gratta, and N. Lehtinen. Experimental study of acoustic ultra-high-energy neutrino detection. *Astrophys. J.*, 621:301–312, 2005. e-Print: arXiv astro-ph/0406105.

[143] N. Kurahashi and G. Gratta. Oceanic ambient noise as a background to acoustic neutrino detection. *Phys. Rev.*, D78:092001, 2008.

[144] J.D. Perkin. *The Acoustic Detection of Ultra High Energy Neutrinos.* PhD thesis, Department of Physics and Astronomy, University of Sheffield, April 2007. e-Print: arXix astro-ph/0801.0991v1.

[145] V. Niess. *Detection acoustique sous-marine de neutrinos de ultra haute energie dans le cadre de l'experience ANTARES.* PhD thesis, Universite de la Mediterranee, Marseille, France, September 2005. (in French).

[146] The NEMO Collaboration. NEMO-*Ονde*: a submarine station for real-time monitoring of acoustic background installed at 2000 m depth in the Mediterranean Sea. *e-Print: arXiv*, 2008. astro-ph/0804.2913.

[147] R.J. Urick. *Sound Propagation in the Sea.* Peninsula Publishing, 1982.

[148] G. Pavan et al. A long term acoistic moitoring of sperm whales off Catania (east coast of Sicily, Italy). INFN LNS Activity Report 2006 (Astroparticle Physics) `http://www.lns.infn.it/report06/`, 2006.

[149] Random Samples. *Science*, 315(5816):1199, 2007.

[150] F. Simeone. *Detection of Underwater Acoustic Signals induced by Ultra-High Energy Neutrinos Interactions.* PhD thesis, "Sapienza" Universitá di Roma, Italy, 2008. In preparation.

[151] G.A. Askaryan and B.A. Dolgoshein. Acoustic Registration of High-Energy Neutrinos. *JETP Lett. (Pis'ma Zh. Eksp. Teor. Fiz.)*, 25(5):232–233, 1977.

[152] L. Sulak, T. Bowen, J.G. Learned, et al. Experimental Studies of the Acoustic Signature of Proton Beams in Fluid Media. *Nuclear Instruments and Methods*, 161:203–217, 1979.

[153] V. I. Albul et al. Measurements of the Parameters of the Acoustic Radiation Accompanying the Moderation of an Intense Proton Beam in Water. *Instruments and Experimental Techniques*, 44(3):327–334, 2001. Original in Russian, translated from "Pribory i Tekhnika Eksperimenta", 3:50-57, 2001.

[154] V. I. Albul et al. Acoustic Field Generated by a Beam of Protons Stopping in a Water Medium. *Acoustical Physics*, 51(1):33–37, 2005. Original in Russian, translated from "Akusticheskii Zhurnal", 51(1):47-51, 2005.

[155] K. Graf. Testing Thermo-Acoustic Sound Generation in Water with Proton and Laser Beams. In R. Nahanhauer and S. Boser, editors, *Acoustic and radio EeV Neutrino detection Activities*, pages 127–131. World Scientific, 2006. Proceedings of the International Workshop ARENA 2005, DESY-Zeuthen, Germany.

[156] IDAC Institute of Acoustics "O. M. Corbino" - Home Page. `http://www.idac.rm.cnr.it/`, 20 May 2008.

[157] G. De Bonis. Studio delle Tecniche di Rivelazione Acustica di Neutrini Astrofisici di Alta Energia. Master's thesis, "Sapienza" Universitá di Roma, Italy, January 2005. Available on line at: http://www.roma1.infn.it/people/debonis (in Italian).

[158] G. De Bonis. Preliminary Results on Hydrophones Calibration with Proton Beam. In R. Nahanhauer and S. Boser, editors, *Acoustic and radio EeV Neutrino detection Activities*, pages 112–116. World Scientific, 2006. Proceedings of the International Workshop ARENA 2005, DESY-Zeuthen, Germany.

[159] ITEP Institute of Theoretical and Experimental Physics - Home Page. http://www.itep.ru/eng/in_eng.shtml.

[160] ARENA 2008 Workshop - Acoustic and Radio EeV Neutrino Actvities - Home Page. http://www.roma1.infn.it/arena2008/, 8 September 2008.

[161] K. Prelec. Ions and Ion Accelerators for Cancer Treatment. *FIZIKA B*, 6(4):177–206, 1997.

[162] C. Grupen. Tumour Therapy with Particle Beams. *e-Print: arXiv physics/0004015*, 2000.

[163] T Satogata et al. Dose/Sensitivity in Proton Computed Tomography. *C-A/AP/#120*, 2003.

[164] *RESON Hydrophone TC4042 Specification Sheet*. Available from the RESON Web Page http://www.reson.com/.

[165] J.W. Eaton. *GNU Octave Manual*. Network Theory Limited, 2002. Web-page: http://www.octave.org/.

[166] S Agostinelli et al. Geant4 - A Simulation Toolkit. *Nuclear Instruments and Methods A*, 506:250–303, 2003.

[167] J Allison et al. Geant4 Developments and Applications. *IEEE Transactions on Nuclear Science*, 53(1):270–278, 2006.

[168] GEANT4 Home Page. http://geant4.web.cern.ch/geant4/, 02 December 2008.

[169] N. Piskunov. *Differential and Integral Calculus*. (Italian Edition: *Calcolo Differenziale e Integrale*, Editori Riuniti, Roma, 3^{rd} ed. edition, 1995. Original Russian Edition: *Differentsialnoe i integralnoe isĉilenja*, published by MIR, Moscow).

[170] D. Eisenberg and W. Kauzmann. *The Structure and Properties of Water*. Oxford at the Clarendon Press, 1969. (Chapter 4).

[171] R.A. Horne. *Water and Aqueous Solutions - Structure, Thermodynamics and Transport Processes*. Wiley-Interscience, 1972. (Chapter 6).

[172] UNESCO. The International System of Units (SI) in Oceanography. *UNESCO Technical Papers in Marine Science*, 45(IASPO Publication Scientifique No. 32), 1985.

[173] UNESCO. International Oceanographic Tables, Vol. 4. *UNESCO Technical Papers in Marine Science*, 40, 1982 (received in 1987).

[174] W.D. Wilson. Equation for the Speed of Sound in Sea Water. *The Journal of the Acoustical Society of America - JAS*, 32(10):1357, 1960.

[175] J.A. Knauss. *Introduction to Physical Oceanography.* Prentice-Hall, 2^{nd} ed. edition, 1997. (Chapter 12 - "Sound and Optics").

[176] E. Lewis. The Practical Salinity Scale 1978 and its Antecedents. *IEEE Journal of Oceanic Engineering*, OE-5(1):3–8, 1980.

[177] UNESCO. The Practical Salinity Scale 1978 and the International Equation of State of Seawater 1980. *UNESCO Technical Papers in Marine Science*, 36, 1981.

[178] G.S. Kell. Precise Representation of Volume Properties of Water at One Atmosphere. *J. Chem. Eng. Data*, 12(1):66–69, 1967.

[179] H.F. Stimson. Heat units and temperature scales for calorimetry. *Am. J. Phys.*, 23:614–622, 1955.

[180] J.O. Smith. Digital Audio Resampling Home Page. `http://www-ccrma.stanford.edu/~jos/resample/`, February 5, 2008.

[181] C. E. Brennen. *Cavitation and Bubble Dynamics.* Oxford University Press, New York, 1995. Availble at persistent URL `http://resolver.caltech.edu/CaltechBOOK:1995.001`.

[182] D. Heck, G. Schatz, T. Thouw, J. Knapp, and J. N. Capdevielle. CORSIKA: a Monte Carlo code to simulate extensive air showers. FZKA-6019, 1998. CORSIKA Home Page `http://www-ik.fzk.de/corsika/`. Last update: August 11, 2008.

[183] T. Sloan. Simulation of Cosmic Ray ν Interactions in Water. In L. Thompson and S. Danaher, editors, *ARENA 2006 - Acoustic and Radio EeV Neutrino detection Activities*, number 81 in Journal of Physics: Conference Series, page 012001, 2007. Proceedings of the International Workshop ARENA 2006, University of Northumbria, Newcastle, UK.

[184] J.D. Bjorken. Asymptotic Sum Rules at Infinite Momentum. *Physical Review*, 179(5):1547–1553, 1969.

[185] L. Devroye. *Non-Uniform Random Variate Generation.* Springer-Verlag, New York, 1986. (Chapter 2). Available on line at `http://cg.scs.carleton.ca/~luc/rnbookindex.html`.

[186] C.W. Helstrom. The Resolution of Signals in White, Gaussian Noise. In *Proceedings of the IRE - Institute of Radio Engineers*, volume 43:9, pages 1111–1118, September 1955.

[187] B.D Van Veen and K. M. Buckley. Beamforming: a Versatile Approach to Spatial Filtering. *IEEE ASSP MAGAZINE*, April 1988.

[188] B. Bachir. *UHE Neutrino Acoustic Detection.* PhD thesis, Universitá degli Studi di Pisa, Italy, June 2008.

[189] S. Bevan, S. Danaher, J. Perkin, S. Ralph, C. Rhodes, Thompson L., T. Sloan, and D. Waters. Simulation of Ultra High Energy Neutrino Interactions in Ice and Water. e-Print: arXiv astro-ph/0704.1025v1, 2007.

[190] L.G. Dedenko et al. Prospect for radio-wave and acoustic detection of ultra- and superhigh-energy cosmic neutrinos (cross sections, signals, thresholds. *Physics of Particles and Nuclei*, 28(3), May-June 1998.

NOTE

Links at web resources have been checked and verified as existing at the time of the preparation of this thesis. In case of web-references, the date, if specified, refer to the last update or the last modification, as indicated in the page.

List of Figures

List of Tables

Acknowledgments

I thank Prof. Antonio Capone and the NEMO team in Roma, for discussions and advices, and for the opportunity and the support with this work; Dr. Tommaso Chiarusi, for his guidance with the simulations, and Dr. Terry Sloan for his kind help. A special thanks to Dr. Manuela Vecchi, for her profitable discussions and her friendly encouragements.

Since this work is not only made of physics, but also of time, and passion, and patience, I would like to thank my family, my closest friends and all those people who have been around me in these years, and helped me with encouragements, advices, suggestions, phrasal verbs (!), quick answers to technical questions and, moreover, pleasant digressions on non-technical ones. A complete list of names should be too long, and a short list would be unfair. Therefore, no names will be included, but people in this ghost-list perfectly know they are always involved. The only name is at the end, the sweet course, Andrea, who succeeds in the most difficult task, knowing my light and loving my dark.